

博士論文

**Crystal structure of asHPAL as a useful aldolase for
the two-step stereoselective synthesis of
4-hydroxyisoleucine: understanding the reaction
mechanism and expanding the substrate specificity**

(4-Hydroxyisoleucine合成に関わる酵素asHPALのX線結晶構造
解析と基質選択性の拡大)

GUO LINJUN

郭琳珺

Contents

Abbreviations	1
Chapter 1 Introduction.....	3
1.1 Chirality and chiral synthesis	4
1.2 Aldol reaction.....	5
1.3 Aldolases	6
1.4 asHPAL, a member of the HpaI/HpcH aldolase subfamily	7
1.5 X-ray crystallography.....	9
1.6 Purpose of the study	10
Tables and figures	11
Chapter 2 Crystal structure of asHPAL	19
2.1 Exordium	20
2.2 Materials and methods	21
2.2.1 Materials.....	21
2.2.2 Protein expression	21
2.2.3 Purification of recombinant asHPAL.....	21
2.2.4 Size-exclusion chromatography	22
2.2.5 Assay for the stereoselectivity of asHPAL	23
2.2.6 Crystallization of asHPAL	24
2.2.7 Data collection and processing.....	25
2.2.8 Structure determination and model refinement	25

2.3	Results and discussion.....	26
2.3.1	Expression and purification of asHPAL.....	26
2.3.2	Oligomeric state of asHPAL	26
2.3.3	Stereoselective activity of purified asHPAL.....	27
2.3.4	Crystallization of asHPAL	28
2.3.5	Data collection and structure determination.....	28
2.3.6	Overall structure of asHPAL.....	29
2.3.7	Structural comparison of asHPAL with the other enzymes of the HpaI/HpcH-aldolase subfamily	30
2.4	Conclusion.....	32
	Tables and figures	33
Chapter 3	Structural basis for the stereoselective aldol reaction of asHPAL	56
3.1	Exordium.....	57
3.2	Materials and methods	59
3.2.1	Crystallization of the asHPAL-2-ketobutyrate complex	59
3.2.2	Crystallization of the asHPAL-2-ketobutyrate-acetaldehyde complex.....	59
3.2.3	Crystallization of asHPAL at pH 6.0	59
3.2.4	Data collection and processing.....	60
3.2.5	Structure determination and refinement.....	61
3.2.6	Docking simulation of acetaldehyde.....	61
3.2.7	Site-directed mutagenesis	62
3.2.8	Kinetics studies of asHPAL and its mutants.....	63
3.2.9	Assays for the stereoselectivity of asHPAL mutants	64

3.3	Results and discussion.....	66
3.3.1	Crystallographic analyses of asHPAL and its complex with 2-ketobutyrate	66
3.3.2	Crystal structure of asHPAL-2-ketobutyrate complex.....	66
3.3.4	Docking simulation of acetaldehyde	67
3.3.5	Kinetics studies of asHPAL	68
3.3.6	Improved catalytic mechanism of the HpaI/HpcH-aldolase subfamily.....	69
3.3.7	Structural basis for stereoselectivity	71
3.3.8	Improving the stereoselectivity of asHPAL	72
3.4	Conclusion.....	74
	Tables and figures	75
Chapter 4	Mechanism of substrate specificity of asHPAL	109
4.1	Exordium.....	110
4.2	Materials and methods	111
4.2.1	Crystallization of asHPAL complexed with pyruvate, oxamate, and 4-methyl-2-oxovalerate	111
4.2.2	Data collection and processing.....	111
4.2.3	Structure determination and refinement.....	112
4.2.4	Docking simulation of 4-methyl-2-oxovalerate.....	112
4.2.5	Site-directed mutagenesis	113
4.2.6	Assay for aldolase activity toward 4-methyl-2-oxovalerate.....	114
4.2.7	Assay for the inhibitory activity of oxamate	115

4.3	Results and discussion.....	116
4.3.1	Structure determination of asHPAL complexed with pyruvate, oxamate, and 4-methyl-2-oxovalerate	116
4.3.2	Binding mode of pyruvate and oxamate at the active site of asHPAL.....	117
4.3.3	Binding mode of 4-methyl-2-oxovalerate at the active site of asHPAL.....	118
4.3.4	Mutations for expanding the substrate specificity of asHPAL toward 4-methyl- 2-oxovalerate.....	119
4.4	Conclusion.....	122
	Tables and figures	123
	Chapter 5 General discussion.....	143
	Tables and figures	148
	References	151
	Acknowledgments.....	161

Abbreviations

4-HIL	4-hydroxyisoleucine
asHPAL	4-hydroxy-3-methyl-2-keto-pentanoate aldolase from <i>Arthrobacter simplex</i> strain AKU 626
BCAT	branched-chain aminotransferase
Bis-tris	bis(2-hydroxyethyl)-iminotris(hydroxymethyl)methane
BLAST	Basic Local Alignment Search Tool
CBB R-250	Coomassie Brilliant Blue R-250
DDS- <i>d</i> ₆	3-(trimethylsilyl)-1-propane-1,1,2,2,3,3- <i>d</i> ₆ -sulfonate
DNA	deoxyribonucleic acid
DTT	dithiothreitol
ESI-TOF-MS	electrospray ionization time-of-flight mass spectrometry
GITC	2,3,4,6-tetra- <i>O</i> -acetyl- β -D-glucopyranosyl isothiocyanate
HEPES	4-(2-hydroxyethyl)-1-piperazineethanesulfonic acid
HMKP	4-hydroxy-3-methyl-2-keto-pentanoate
HPLC	high performance liquid chromatography
IPTG	isopropyl β -D-1-thiogalactopyranoside
LB	Luria-Bertani
PCR	polymerase chain reaction
PDB	protein data bank
PEG	polyethylene glycol
PF	Photon Factory
PLP	pyridoxal phosphate
RMSD	root-mean-square deviation

SDS-PAGE sodium dodecyl sulfate-polyacrylamide gel electrophoresis
TIM triosephosphate isomerase
Tris *tris*(hydroxymethyl)aminomethane

Chapter 1

Introduction

1.1 Chirality and chiral synthesis

Chirality is the configuration, or handedness (left or right), of a molecule that cannot be completely overlapped by its enantiomer (mirror image of the molecule). Chirality is common in organic molecules due to the presence of asymmetric carbon atoms [1]. At present, more than 60% of commercially available drugs are sold as single enantiomers [2, 3].

It is generally understood that different configurations of a given molecule often possess different properties. The enantiomer of vitamin C, which shows no pharmacological activity, cannot be absorbed by humans when ingested [4]. Quinidine and its stereoisomer quinine possess both anti-malarial and myocardial depressive properties. Quinidine is also used as an anti-arrhythmic drug [5]. Thalidomide is an immunomodulatory drug that is used for nausea and for alleviating morning sickness in pregnant women. This drug is functional only in *R*-form, whereas its *S*-form has been reported to be strongly teratogenic and is estimated to have caused phocomelia in ten thousand infants [6]. The ability to obtain a single enantiomer therefore significantly impacts not only drug efficacy but also drug safety.

There are three well-known approaches used to produce a single enantiomer of interest: chiral resolution to separate a desired single enantiomer from a racemic mixture (a mixture with equal parts left- and right-handed enantiomers of a chiral molecule) [7]; the chiral switch method to transform the racemic mixture into a single enantiomer [7]; and the chiral synthesis method, which involves either a single reaction or a chain of reactions, to generate one or more new elements of chirality and obtain the target enantiomer directly [8]. With chiral resolution, only 50% of the target enantiomer is obtained. The chiral switch is required for an additional transformation reaction after synthesis. Compared with these methods, the chiral synthesis method is more economical in terms of material and energy due to a lower workload. These two advantages make the method more valued, and thus, this method is widely applied in

chemical industries [1].

The chiral synthesis methods proposed thus far are divided into chemical synthesis methods and biocatalysis methods. Chemical synthesis methods include the following: enantioselective catalysis using chiral coordination complexes [9, 10]; stereoselective catalysis using chiral auxiliaries, which are combined with a prochiral substrate to form an intermediate that controls the stereoselectivity of a subsequent reaction to generate a chiral product [11]; and chiral pool synthesis, which directly connects an available chiral starting compound with another compound to generate a new chiral compound. The biocatalysis method uses enzymes to synthesize the target enantiomer preferentially [8]. Organic solvent and heavy metals are widely used in the chemical synthesis methods. In contrast, the biocatalysis method is more commonly used in industry when it demonstrates the advantages of considerably high stereoselectivity, relatively mild reaction conditions, and a less harmful impact on human environment [12].

1.2 Aldol reaction

An aldol is a compound with β -hydroxyl and carbonyl groups and is a common structural unit that can be found in many important compounds [13], such as the cholesterol-lowering drug atorvastatin and the immunosuppressive drug tacrolimus. Aldols can be generated by the aldol reaction of two reacting carbonyl compounds [1, 14-17]. This reaction is particularly useful because it can generate new chiral centers (one or more) and form a new carbon-carbon bond in a single reaction [18, 19]. The reaction mechanism and stereoselectivity have been improved through extensive studies [20-24]. There are many methodologies that promote aldol reactions in high yield and control the relative and absolute stereochemical configurations at

chiral centers simultaneously. The enantioselective regulation can be achieved by the use of metal ions [25], specific electrophiles [26], enzymes as biocatalysts [15, 16], etc.

The aldol reaction proceeds by two fundamentally different mechanisms (Fig 1-1) [15, 16]. One of the reaction mechanisms includes an enol formation step (Fig. 1-1A). Carbonyl compounds with one or two α -carbons (aldehyde and ketone) are generally nucleophilic at the α -carbon and thus can be converted to enol intermediates in acidic conditions. The intermediate attacks the protonated carbonyl carbon of aldehyde to generate an aldol. The other reaction mechanism is via an enolate intermediate, which is formed by deprotonation at the α -carbon of the carbonyl compound and then attacks the electrophile of aldehyde to generate aldol (Fig. 1-1B).

1.3 Aldolases

Aldolases are a type of enzyme that can catalyze the aldol reaction for specific substrates. The reaction catalyzed by aldolases can proceed under mild conditions and thus has the advantage of low environmental impact. In addition, some aldolases have the potential to be used as biocatalysts for stereoselective aldol reactions. Aldolases are divided into two classes (I and II) according to activation states of their reaction processes [27]. The reaction mechanism of aldolases has been reported and thoroughly discussed [28-30]. Class I aldolases form a ketimine Schiff base intermediate with the substrate using a lysine residue at the active site [31, 32]. Class II aldolases form an enolate intermediate from the substrate using metal ions that polarize the carbonyl group of the substrates [33]. Aldolases are further classified into more than 30 subfamilies according to their substrate specificities and the types of residues that participate in the aldol reaction and metal ion coordination. Phylogenetic tree (Fig. 1-2)

constructed for these aldolases showed the obvious differences between these subfamilies. In addition, aldolase existed widely in both eukaryote and prokaryote and were involved in glycolysis pathway [34].

1.4 asHPAL, a member of the HpaI/HpcH aldolase subfamily

4-Hydroxy-3-methyl-2-keto-pentanoate aldolase (asHPAL) is an aldolase from *Arthrobacter simplex* strain AKU 626 that belongs to the HpaI/HpcH aldolase subfamily of the class II aldolases. asHPAL uses Mg^{2+} as a prosthetic group to catalyze aldol reactions and has the potential for use in the synthesis of (2*S*,3*R*,4*S*)-4-hydroxyisoleucine (4-HIL) (Fig. 1-3) [35], which is a chiral amino acid extracted from the seeds of fenugreek *Trigonella foenum-graecum* [36]. Among the 8 possible enantiomers of 4-HIL, only (2*S*,3*R*,4*S*)-4-HIL exhibits the activity in enhancing the production of insulin from pancreatic β -cells [37-40]. Therefore, (2*S*,3*R*,4*S*)-4-HIL potentiates insulin secretion at supranormal glucose levels, whereas it is ineffective at low or basal glucose concentrations. The (2*S*,3*R*,4*S*)-4-HIL synthesis method using asHPAL involves two steps from the substrates 2-ketobutyrate and acetaldehyde (Fig. 1-3) [35]. In the first step, asHPAL catalyzes the aldol reaction between 2-ketobutyrate and acetaldehyde to form (3*S*,4*S*)-4-hydroxy-3-methyl-2-keto-pentanoate (HMKP). This product is converted to (2*S*,3*R*,4*S*)-4-HIL by branched-chain amino-acid aminotransferase (BCAT). The *S*-configuration of the C2 atom of (2*S*,3*R*,4*S*)-4-HIL is strictly controlled by BCAT [41, 42]. Therefore, the first step catalyzed by asHPAL is the key step in determining the spatial configuration of (2*S*,3*R*,4*S*)-4-HIL [35].

The HpaI/HpcH-aldolase subfamily is divided into three functional subgroups [15, 16]: 2,4-dihydroxyhept-2-ene-1,7-dioic acid (HHDE) aldolase, 2-keto-3-deoxyglucarate (KDG)

aldolase, and 4-hydroxy-2-oxovalerate (HKP) aldolase. YfaU (putative HHDE aldolase) [43] and YhaF (KDG aldolase) [44] from *Escherichia coli* and BphF (putative HKP-aldolase) from *Novosphingobium aromaticivorans* [45] were also used to examine whether they could stereoselectively catalyze the first step of the (2*S*,3*R*,4*S*)-4-HIL synthetic process similarly to asHPAL. The reaction was catalyzed by YfaU, YhaF, and BphF, but asHPAL exhibited the most preferential activity for the synthesis of (3*S*,4*S*)-HMKP (Fig. 1-4) [35]. Of the tested pH values, the stereoselectivity of asHPAL was highest at pH 6.0. However, the stereoselectivity is not strict for the production of (3*S*,4*S*)-HMKP. As described above, the stereoselective synthesis of (3*S*,4*S*)-HMKP is the key step of the designed (2*S*,3*R*,4*S*)-4-HIL biosynthetic process, which requires the uses of an enzyme with strict stereoselectivity. In addition, α -keto acids with several functional groups are potentially useful as intermediates for pharmaceutical synthesis. The enzymes with high stereoselectivity are expected to be useful for the stereoselective synthesis of other compounds.

Among the enzymes of the HpaI/HpcH-aldolase subfamily, 2,4-dihydroxyhept-2-ene- 1,7-dioic acid aldolase (HpcH) [46], YfaU [44], and YhaF [43] share 45%, 40%, and 38% sequence similarities to asHPAL, respectively. The catalytic mechanisms of HpcH, YfaU, and YhaF have been proposed based on their structures [43, 44, 46, 47]. Fig. 1-5 shows the proposed catalytic mechanism of YfaU in the reverse aldol reaction [47]. (a) The Mg^{2+} -bound water is activated to hydroxide ion by the intersubunit His49-Asp88 dyad. (b) The substrate, 4-hydroxy-2-oxopentanoate, binds to Mg^{2+} in a bidentate fashion with the C1 hydroxyl group and the C2 carbonyl oxygen. Arg74 interacts with the C2 carbonyl oxygen and the C4 hydroxyl group. An activated hydroxide ion abstracts the C4 hydroxyl proton, which is coupled with the breakage of the C3–C4 carbon–carbon bond to produce an aldehyde product and pyruvate enolate. (c) The C2 oxygen of pyruvate enolate is protonated by the Mg^{2+} -bound water. (d) The enzyme is returned to its ground state, and the catalytic cycle is completed by producing pyruvate and

acetaldehyde. In contrast, the aldol reaction of HpcH is thought to proceed inversely and is similar to that of YhaF (Fig. 1-6) [46]. (a) The Mg^{2+} -bound water is activated to hydroxide ion by His45. (b) The hydroxide ion abstracts a proton from the C2 methyl group of pyruvate to generate the nucleophilic enolate. (c) The enolate attacks the electrophilic carbon of the succinic semialdehyde acceptor. (d) The C4 oxygen is protonated by His45 to form a hydroxyl group. (e) The catalytic cycle is completed by producing 4-hydroxy-2-ketoheptane-1,7-dioate.

The sequence alignment of asHPAL with HpcH, YhaF, and YfaU shows that the proposed catalytic residues are conserved in asHPAL as His52, Arg77, and Asp91 (Fig. 1-7) [44, 47]. In addition, the Mg^{2+} -chelating residues of asHPAL are also conserved as Glu156 and Asp182. These correlations suggest that asHPAL works via a reaction mechanism similar to HpcH, YhaF, and YfaU. However, the sequence alignment cannot explain why asHPAL stereoselectively synthesizes (3*S*,4*S*)-HMKP. In addition, it remains unclear how asHPAL defines substrate specificity. asHPAL can catalyze the aldol reactions of small α -keto acids, including pyruvate and 2-ketobutyrate (Table 1-1). This selectivity also limits the utility of asHPAL for other stereoselective aldol reactions. The mechanistic bases of substrate specificities have not been reported for the other enzymes of the HpaI/HpcH-aldolase subfamily.

1.5 X-ray crystallography

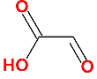
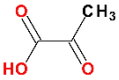
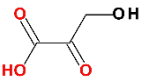
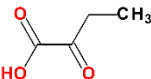
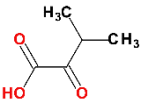
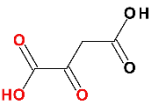
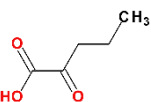
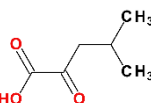
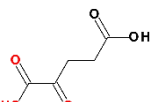
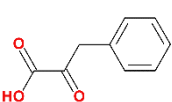
X-ray crystallography is a powerful tool that is used to identify molecular structure at the atomic level. A beam of incident X-rays is diffracted into a number of different specific directions according to the distribution of the atoms in a crystal [48]. Each of the diffracted X-rays is detected as a diffraction spot by the detector. Measuring the distribution of the diffraction spots and subsequent data processing produce a three-dimensional diagram of the electron

density, which is useful for determining the mean positions of the atoms in the crystal. The protein structure of interest can be determined by using molecular replacement methods considering its amino acid sequence and the known structures of similar proteins [49]. From the structural information including the distance between atoms, we can understand the interaction between an enzyme and its substrate, the changes of protein states, and other structure-function relationships of proteins. In addition, structural results are often useful for protein engineering, such as to control protein function, expand substrate specificity, etc.

1.6 Purpose of the study

α -Keto acids are valuable intermediates that are conventionally used for pharmaceutical synthesis, and the aldol reaction is a useful tool to extend the carbon chain. asHPAL has potential as a biocatalyst for stereoselective aldol reactions, especially the stereoselective synthesis of (2*S*,3*R*,4*S*)-4-HIL coupled with the reaction of BCAT. The catalytic mechanisms of the HpaI/HpcH-aldolase subfamily toward α -keto acid substrates have been proposed in previous reports [43, 46, 47]. However, the mechanistic bases of the HpaI/HpcH-aldolase subfamily's stereoselectivity and substrate specificity remain unclear. Understanding these points will be conducive to improving the enzymatic properties of asHPAL. Here, I applied X-ray crystallography to reveal the structural basis of the stereoselectivity and substrate specificity of the aldol reaction catalyzed by asHPAL. Moreover, the obtained structural information was successfully used to improve the stereoselectivity and expand the substrate specificity of asHPAL.

Table 1-1 Substrate specificity of asHPAL.

α -Keto acid	Chemical formula	Availability ^a
Glyoxylate		—
Pyruvate		+
Hydroxypyruvate		—
2-Ketobutyrate		+
3-Methyl-2-ketobutyrate		—
Oxalacetate		—
2-Ketopentanoate		—
4-Methyl-2-oxovalerate		—
2-Ketoglutarate		—
Phenylpyruvate		—

^a“+” indicates that the compounds are used as substrates of asHPAL.

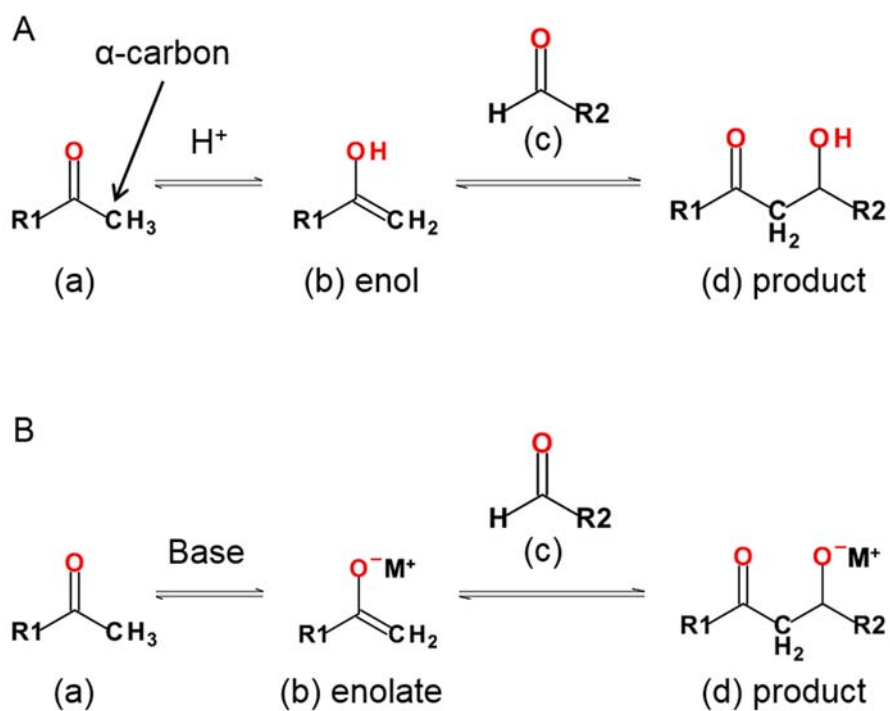


Fig. 1-1 Two different mechanisms of aldol reaction [15, 16].

(A) The pathway via an enol intermediate, in which carbonyl compound (a) is converted to enol (b) due to the nucleophilicity of α -carbon. The enol attacks aldehyde (c) to generate product (d).

(B) The pathway via an enolate intermediate, in which carbonyl compound (a) is deprotonated to form enolate (b). The enolate attacks the aldehyde (c) to generate product (d). “ M^+ ” indicates a metal ion.

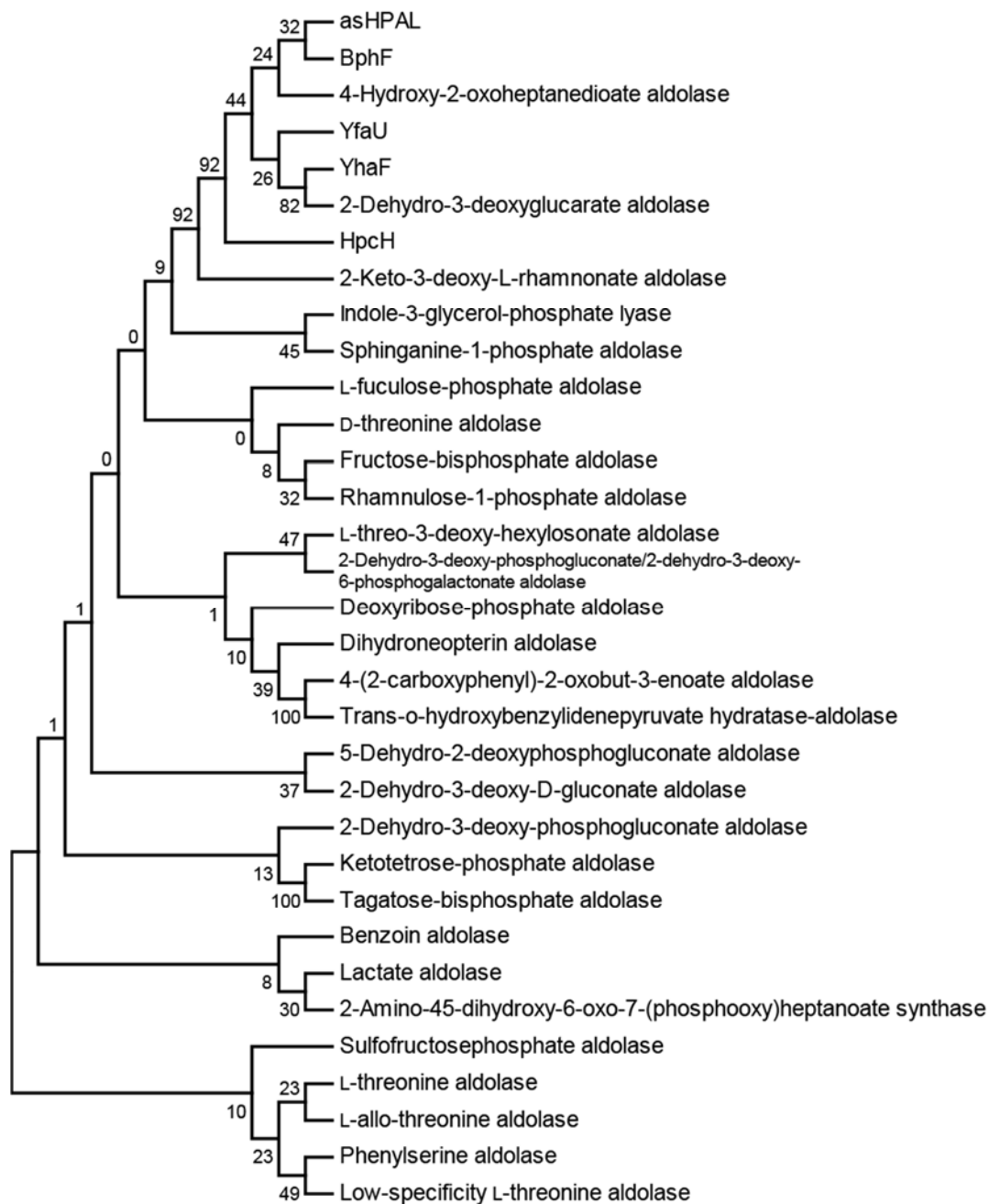


Fig. 1-2 Neighbor joining phylogenetic trees showing the relationship of asHPAL and other subfamilies of aldolase.

Similar results were obtained using maximum parsimony. The tree was constructed using the MEGA 6.0 program with the neighbor-joining algorithm[50]. Only bootstrap values greater than 50% are shown. The values are calculated with 0.2 substitution per amino acid site.

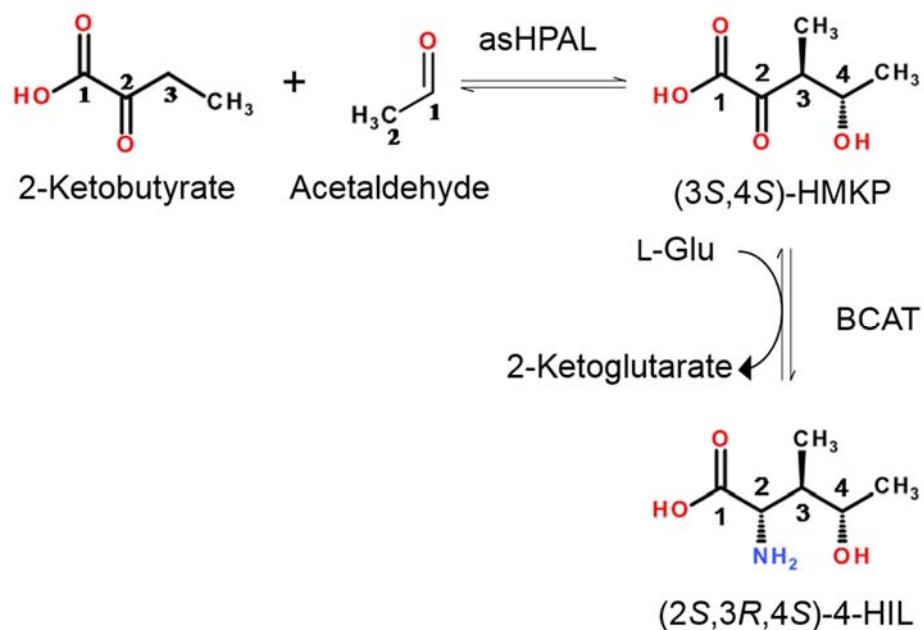


Fig. 1-3 Two-step enzymatic synthesis of (2*S*,3*R*,4*S*)-4-hydroxyisoleucine (HIL) by asHPAL and BCAT [35].

Firstly, asHPAL converts 2-ketobutyrate and acetaldehyde to (3*S*,4*S*)-4-hydroxy-3-methyl-2-keto-pentanoate (HMKP). Secondly, (3*S*,4*S*)-HMKP is converted to (2*S*,3*R*,4*S*)-4-HIL by BCAT. In the second reaction, the amino group of L-glutamic acid (L-Glu) is transferred to (3*S*,4*S*)-HMKP.

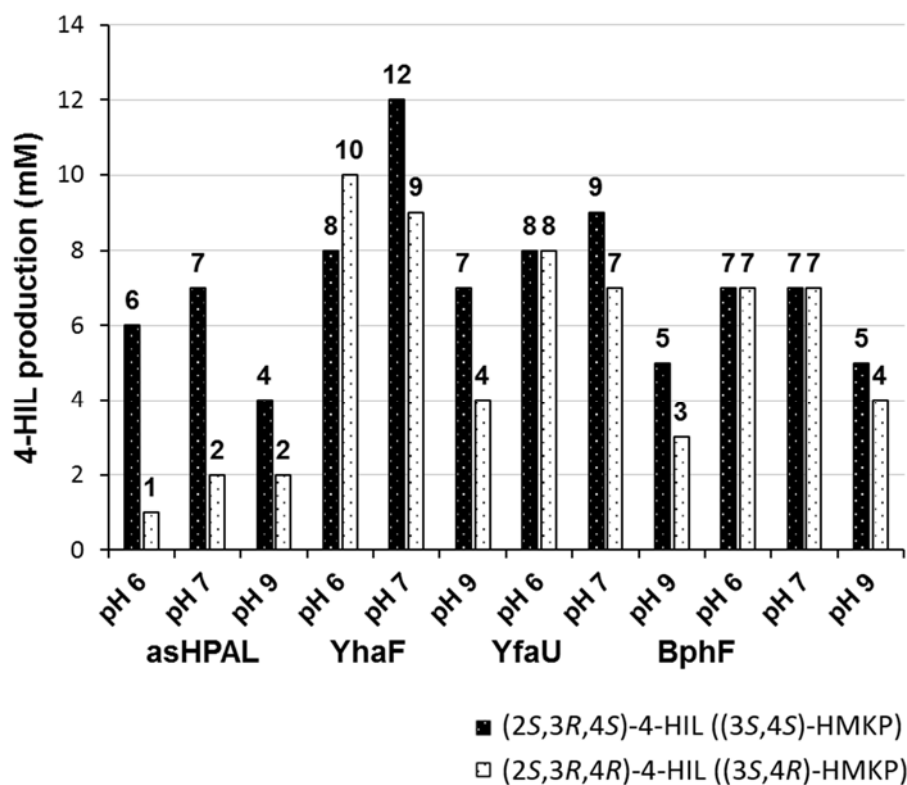


Fig. 1-4 pH dependency of 4-HIL enantiomer production catalyzed by each enzyme of the HpaI/HpcH-aldolase subfamily and BCAT.

The amounts of (2*S*,3*R*,4*S*)-4-HIL and (2*S*,3*R*,4*R*)-4-HIL are equivalently estimated as the amounts of (3*S*,4*S*)-HMKP and (3*S*,4*R*)-HMKP, respectively. The *S*-configuration of the C2 atom of 4-HIL is strictly controlled by the BCAT [41, 42]. In the sequential reaction to 4-HIL from 2-ketobutyrate and acetaldehyde (Fig. 1-2), the first reaction are catalyzed by each enzyme of the HpaI/HpcH-aldolase subfamily (asHPAL, YhaF, YfaU and BphF). asHPAL can preferentially catalyze the synthesis of (3*S*,4*S*)-HMKP [(2*S*,3*R*,4*S*)-4-HIL] [51].

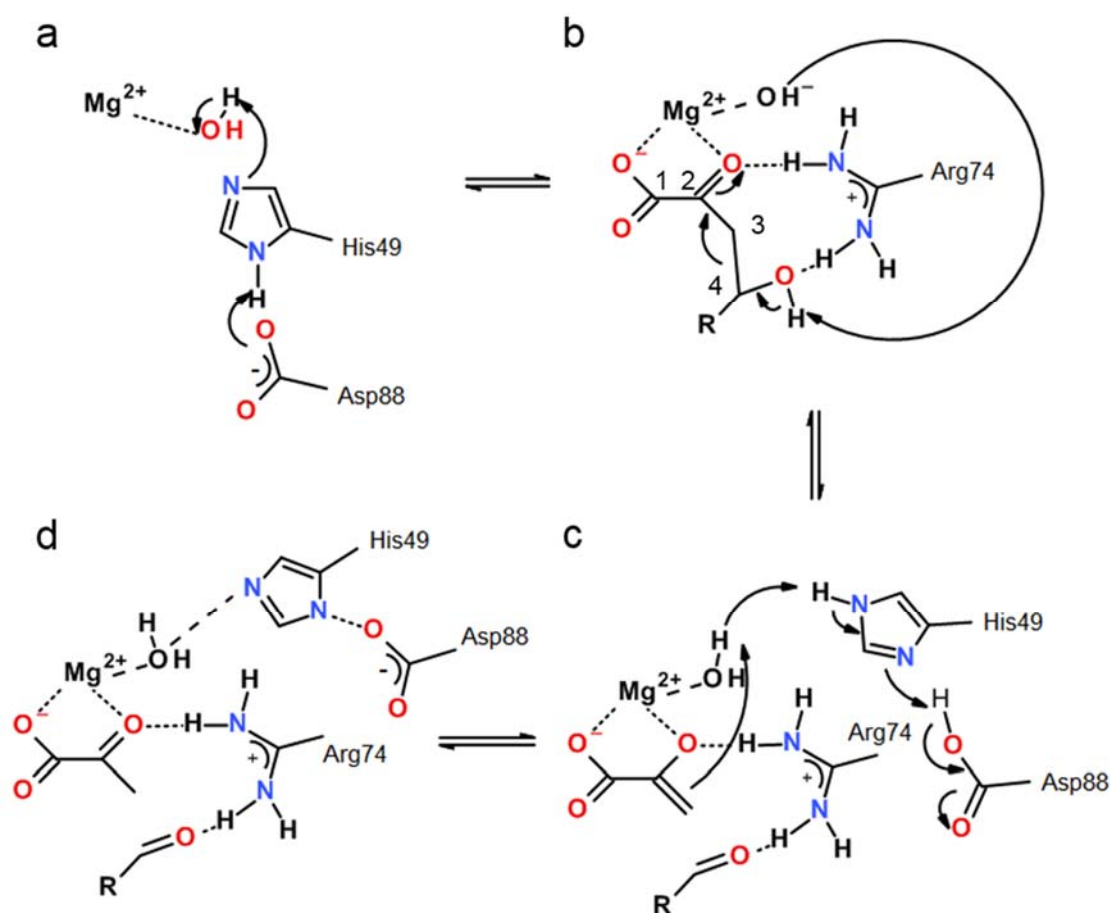


Fig. 1-5 Proposed catalytic mechanism of YfaU which catalyzes the decomposition of 2-keto-3-deoxy acid sugar.

(a) The Mg^{2+} -bound water is activated to hydroxide ion by the intersubunit His49-Asp88 dyad. (b) The substrate, 2-keto-3-deoxy acid sugar, binds to Mg^{2+} in a bidentate fashion with the C1 hydroxyl group and the C2 carbonyl oxygen. Arg74 interacts with the C2 carbonyl oxygen and the C4 hydroxyl group. An activated hydroxide ion abstracts the C4 hydroxyl proton, which is coupled with the breakage of the C3-C4 carbon-carbon bond to produce aldehyde product and pyruvate enolate. (c) The C2 oxygen of pyruvate enolate is protonated by the Mg^{2+} -bound water. (d) The enzyme is returned to its ground state, and the catalytic cycle is completed by producing pyruvate and acetaldehyde. [47].

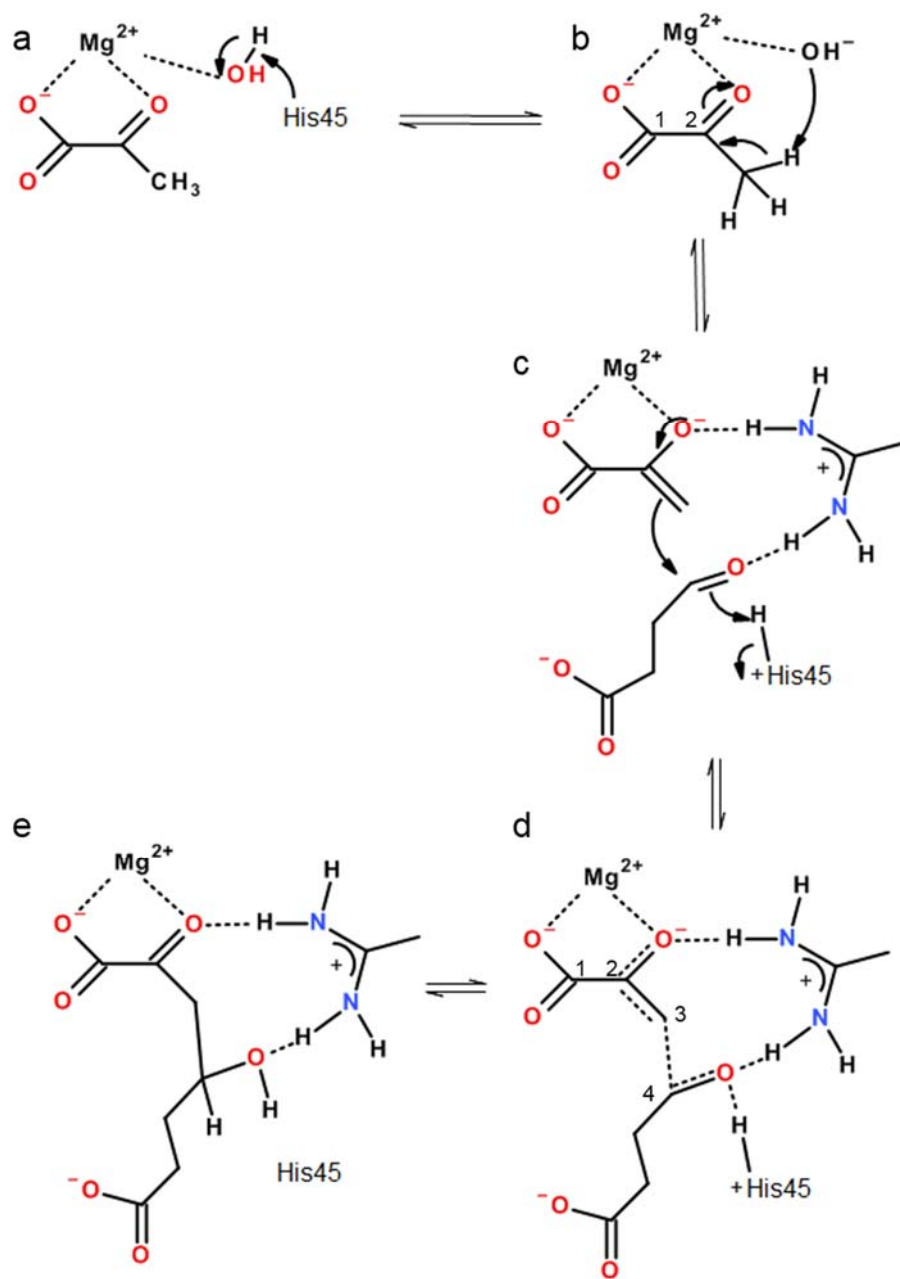


Fig. 1-6 The catalytic mechanism of HpcH which catalyzes aldol reaction.

(a) The Mg^{2+} -bound water is activated by a hydroxide ion from His45. (b) The hydroxide ion abstracts a proton from the C2 methyl group of pyruvate to generate the nucleophilic enolate. (c) The nucleophilic enolate attacks the electrophilic carbon of the succinic semialdehyde acceptor. (d) The C4 oxygen is protonated by His45 to form a hydroxyl group. (e) The enzyme adopts a ground state, and catalytic cycle is completed by producing 4-hydroxy-2-ketoheptane-1,7-dioate [46].

asHPAL	MFPFVELPDNFAKRVTDSDSAQVGLFISGGSETNAEIVASAGFDWLLIDAEHSPYGLETV	60
HpcH	—MDLPVNRFKQRLRSGEAQIGLWLGADPYCAELAAAGFDWLLLDGEHAPNDRSL	56
YhaF	—MNNDVFPNKFKAAALAAKQVQIGCWSALSNPISTEVLGLAGFDWLVLDGEHAPNDISTF	58
YfaU	—MNALLSNPFKERLRKGEVQIGLWLSSTTAYMAEIAATSGYDWLLIDGEHAPNTIQDL	57
BphF	—MQTPVNSFKAALREGPVQLGFWLALAHDPIDAEICAGGGYDWLLIDGEGPQTLPGI	56
	* * .*: : . :*: . *::*:*:*.**.* : .	
	▲	
asHPAL	TSLLRVAAYP-ATPVVRIPVNDTVLIKQYLDLGAQNLMPVMVHNAEQAEKAVAAMHYPP	119
HpcH	LGQLQALAPYP-GQPVI RPVQGD TALIKQLLDIGAQTLLVPMVDSAAQAEGLVRAVRYPP	115
YhaF	IPQLMALKGSA-SAPVV RVPTNEPVI I KRLLDIGFYNFLIPFVETKEEAELAVASTRYPP	117
YfaU	YHQLQAVAPYA-SQPVI RPVEGSKPLIKQVLDIGAQTLLIPMVDTAEQARQVVSATRYPP	116
BphF	VAQLRAVEATPPCSAIVRVPGHDSVTIKQVLDLGAQTLMPVMVETAEQAKAIVTASRYPP	116
	* : : :*: . **:* **.* .::*:*. .:*. * : :***	
	▲	
	▲	
asHPAL	RGVRGIGAALARSSRFNGVDDYLNKASETVSLTVQVESAEAVENAAEVAAVDGVDAIFIG	179
HpcH	AGVRG VGSALARASRWNSVAEYLDHADEQMCLLVQVENLEGLANLDAIAAVEGVDGVFIG	175
YhaF	EGIRGVSVS-HRANMFQTVADYFAQSNKNITILVQIESQQGVNDVDAIAATEGVDGIFVG	176
YfaU	YGERGVGASVARAARWGRIENYMAQVNDLCLLVQVESKALTDLNDEILDVEGIDGVFIG	176
BphF	AGERLGG-ARASRWGGYPAYVAEANAQVCIIAQIETATAVDNIEAIAAVDGDIDALFLG	174
	* **:. * : : * . . : :*.**.* .: * : .:*.**.*:	
	▲	
asHPAL	PSDLAASMGLLGQQHPAVLAAVDTTFKAVRDAGKLVGINAFNLQAQAYIDAGASFVCV	239
HpcH	PADLSAAMGHRGNPGHPEVQAATEDAIRRIRAAGKAAGILSADEALARRYLELGCASFVAV	235
YhaF	PSDLAALGHLGNASHPDVQKAIQHIFNRAAHGKPSGILAPVEADARRYLEWGATFVAV	236
YfaU	PADLSASLGYPDNAGHPEVQRIIETSIRRIRAAGKAAGFLAVAPDMAQQCLAWGANFVAV	236
BphF	PADLAATEGLLGASSFDALFKLTGEALARIVATGKPPAGILSRDERLVQQFLDGGARFIAN	234
	*:***:* * . : : ** * : : . : : * . *:	
	▲	
asHPAL	GADVQQLASATRALVEKFKG----- 259	
HpcH	GVDTSLLMRSLRELAGRFKGGAPAPSVSSSVYG 268	
YhaF	GSDLGVFRSATQKLADTFKK----- 256	
YfaU	GVDTMLYSDALDQRLAMFKSGKNGPPIKGSY- 267	
BphF	GIDSFTFAKGAGDGLRRWRERIAAAG-GV- 262	
	* * . : :	

Fig. 1-7 Sequence alignment of asHPAL with other class II aldolases.

The amino acid sequence of asHPAL is aligned with those of other enzymes of HpaI/HpcH-aldolase subfamily, HpcH (45% sequence identity to asHPAL), YhaF (38%), YfaU (40%), and BphF (39%). The sequence alignment was generated by ClustalW [52]. Identical and highly conserved residues are indicated with asterisks, and double or single dots, respectively. Active-site residues are shown by red triangles. These enzymes share the amino acid residues which are important for the catalytic reaction.

Chapter 2

Crystal structure of asHPAL

2.1 Exordium

X-ray crystallography is a powerful technique for analyzing enzymatic mechanisms. This technique has been used to understand the structural bases of the stereoselectivity and substrate specificity of asHPAL.

High quality crystals, which diffract X-rays at high resolution, provide detailed structural information including the catalytic mechanism of enzymatic reactions. The discovery and optimization of appropriate crystallization conditions are the bottlenecks of X-ray crystallography. In addition, a large amount of protein (> 10 mg) of high purity is often required for crystallization experiments. Therefore, protein expression and purification are also important steps in X-ray crystallography, and the fundamental asHPAL preparation procedure is the basis of further biochemical analyses. In this chapter, I describe the protein preparation, crystallization, and X-ray diffraction data collection and processing used to determine the crystal structure of asHPAL. The purified protein was also used to evaluate the properties of asHPAL such as enzymatic activity and oligomer formation in solution.

2.2 Materials and methods

2.2.1 Materials

An *E. coli* plasmid vector for the expression of recombinant asHPAL and purified (2*S*,3*R*,4*S*)-4-HIL were provided by Prof. Dr. OGAWA Jun (Kyoto University). All other chemicals were of biochemical research grade and were purchased from Nacalai Tesque, Sigma-Aldrich, Wako Pure Chemical Industries, Hampton Research, Merck, and Tokyo Chemical Industry.

2.2.2 Protein expression

asHPAL was overexpressed in *E. coli* Rosetta (DE3) (Novagen) harboring the plasmid vector for recombinant asHPAL. The expressed protein (residues 1–259) has an N-terminal sequence including a His-tag. The *E. coli* cells were cultivated in Luria-Bertani (LB) medium (Merck) containing 30 $\mu\text{g ml}^{-1}$ ampicillin at 310 K. The expression conditions for asHPAL were optimized by changing the induction temperature (291 K, 298 K, and 310 K) and the concentration of isopropyl β -D-thiogalactopyranoside (IPTG) (0.1 mM, 0.25 mM, 0.5 mM, and 1.0 mM final concentrations). Cell lysates were separated into soluble and insoluble fractions by centrifugation and then analyzed by sodium dodecyl sulfate-polyacrylamide gel electrophoresis (SDS-PAGE; total acrylamide concentration of the separation gel, 15%). The separation gel was stained with Coomassie Brilliant Blue (CBB) R-250. The optimal expression conditions were chosen based on the amount of asHPAL in the soluble fraction.

2.2.3 Purification of recombinant asHPAL

The harvested cells were suspended in buffer A (40 mM Tris-HCl, pH 7.5, 400 mM NaCl,

5 mM imidazole, and 1 mM DTT) and were then disrupted by sonication on ice. After centrifugation at $40,000 \times g$ at 277 K for 30 min, the supernatant was loaded onto a Ni-Sepharose 6 Fast Flow (GE Healthcare Life Sciences) column (3-ml gel bed) at 298 K. After washing with buffer B (40 mM Tris-HCl, pH 7.5, 400 mM NaCl, 50 mM imidazole, and 1 mM DTT), the asHPAL protein was eluted with buffer C (40 mM Tris-HCl, pH 7.5, 400 mM NaCl, 200 mM imidazole, and 1 mM DTT) at 298 K. The eluted protein was dialyzed against a 100-fold excess of the external solution (40 mM Tris-HCl, pH 7.5 and 1 mM DTT) at 277 K for 12 h.

The protein was further purified by anion-exchange column chromatography using the ÄKTA purifier system (GE Healthcare). The proteins were loaded onto a Resource Q 6-ml (GE Healthcare) column pre-equilibrated with 40 mM Tris-HCl (pH 7.5) at 277 K and were eluted with a linear gradient of 0–1 M NaCl in 40 mM Tris-HCl (pH 7.5) at 277 K. The purity of asHPAL was evaluated by SDS-PAGE (total acrylamide concentration of the separation gel, 15%). The separation gel was stained with CBB R-250. The purified asHPAL was dialyzed against 20 mM Tris-HCl (pH 7.5) at 277 K and was concentrated to 10 mg ml^{-1} using a Vivaspin 20 concentrator (molecular weight cut off, 5 k, hydrozart membrane; Vivascience) at 277 K. Protein concentrations were determined by the absorbance at 280 nm with a molar extinction coefficient of $14,565 \text{ M}^{-1} \text{ cm}^{-1}$ [53] and a molecular weight of 27,130.

2.2.4 Size-exclusion chromatography

To analyze the oligomeric state of asHPAL, 0.5 ml of purified protein (5 mg ml^{-1}) was loaded onto a Superdex 200 10/300 GL (GE Healthcare) column equilibrated with 20 mM Tris-HCl (pH 7.5), 300 mM NaCl, and 1 mM DTT. The flow rate was set at 1 ml min^{-1} . The Gel Filtration Calibration Kit HMW and Gel Filtration Calibration Kit LMW (GE Healthcare) were used for column calibration. Each standard protein was dissolved in buffer containing 20 mM

Tris-HCl (pH 7.5), 300 mM NaCl, and 1 mM DTT. All standard proteins were mixed at final concentrations of 1.0 mg ml⁻¹ each. The solution (0.5 ml) was applied to the size-exclusion chromatography under the same conditions as asHPAL.

2.2.5 Assay for the stereoselectivity of asHPAL

Both 2-ketobutyrate and acetaldehyde substrates were used to confirm the aldolase activity of asHPAL. Because the stereoselectivity of asHPAL is known to vary with pH, the reactions were performed at different pH values (6.0, 7.0, and 8.0) to confirm the pH-dependent stereoselectivity of asHPAL.

The reaction conditions were as follows: 100 mM 2-ketobutyrate, 100 mM acetaldehyde, 2 mM MgCl₂, 50 μM PLP, 200 mM L-glutamic acid (L-Glu), 369 nM asHPAL, 369 nM BCAT, and 20 mM buffer [bis-tris (pH 6.0), Tris-HCl (pH 7.0), or Tris-HCl (pH 8.0)]. After incubation at 303 K for 12 h, the reaction was confirmed by high performance liquid chromatography (HPLC). The reaction solutions were diluted with 40 volumes of acetonitrile and were incubated with 10 mM 2,3,4,6-tetra-*O*-acetyl-β-D-glucopyranosyl isothiocyanate (GITC) and 80 mM triethylamine (TEA) to derivatize the reaction products for UV detection (Fig. 2-1) [54].

Derivatized solution (20 μl) was loaded onto a CAPCELL C18 MG column (250 mm × 4.6 mm, 5 μm; Shiseido) equilibrated with solution A (10 mM KH₂PO₄, pH 2.95) using a Shimadzu 10ATvp HPLC system. The elution was performed with a linear gradient from 0% solution A (10 mM KH₂PO₄, pH 2.95) to 80% solution B (100% acetonitrile) for 120 min, and the flow rate was set at 1.0 ml min⁻¹. The enantiomers, (2*S*,3*R*,4*S*)-4-HIL and (2*S*,3*R*,4*R*)-4-HIL, were separately detected with a UV detector (254 nm) as GITC derivatives. The purified (2*S*,3*R*,4*S*)-4-HIL (10 mM) was derivatized with GITC and was used as a standard for the identification of retention time and for quantification. The peak area of the standard was

compared to those of the derivatized 4-HIL enantiomers produced by asHPAL to determine the concentrations of the enantiomers.

The fraction eluted at the retention time of 69.5 and 70.8 min was mixed with an equal volume of methanol and was then injected into the JMS-T100LLP time of flight mass spectrometer (JEOL) equipped with an electrospray ionization (ESI) source (JEOL) to confirm that each fraction contained 4-HIL. The mobile phase was 100% methanol and was constantly pumped at 0.50 ml min⁻¹. The conditions for ESI-MS detection were as follows: positive ion mode; needle voltage, 2,000 V; ring lens voltage, 10 V; orifice 1 voltage, 70 V; orifice 2 voltage, 10 V; desolvation gas temperatures, 523 K; desolvation gas flow, 573 l h⁻¹; and the orifice 1 temperatures, 353 K. Data were obtained using Mass Center software, MS-56010MP (JEOL).

2.2.6 Crystallization of asHPAL

The purified asHPAL (10 mg ml⁻¹) was used for crystallization experiments. Initial crystallization trials were performed by the sitting-drop vapor diffusion method using sparse-matrix screening kits: Crystal Screen HT, Index HT (Hampton Research), and Wizard I and II (Emerald Biosystems). Each drop was prepared by mixing equal volumes (0.7 µl) of the protein solution and a reservoir solution and was then equilibrated against 70 µl of the reservoir solution at 277 or 293 K.

After obtaining crystals, the 2D grid optimization of crystallization conditions (pH vs. precipitant concentration) was performed by the sitting-drop vapor diffusion method using 24-well Cryschem plates (Hampton Research). Each drop was prepared by mixing equal volumes (2.0 µl) of the protein solution and a reservoir solution and was then equilibrated against 400 µl of the reservoir solution at 293 K.

2.2.7 Data collection and processing

Each asHPAL crystal was picked up in a nylon loop (Hampton Research) and then transferred to a cryoprotectant solution prepared by mixing 76% (v/v) of the reservoir solution and 24% (v/v) of glycerol. The crystals were mounted on the X-ray diffractometers and were flash-cooled in a cryo-nitrogen stream (95 K). The X-ray diffraction data set (600 images) of an asHPAL crystal grown at pH 7.7 was collected with synchrotron radiation and an ADSC Quantum 210 detector on BL-5A beamline at Photon Factory (Ibaraki, Japan). The parameters of data collection were as follows: wavelength, 1.0000 Å; collection angle, 180°; oscillation angle, 0.3°; crystal-to-detector distance, 142 mm; and exposure time, 0.5 sec.

2.2.8 Structure determination and model refinement

The scaled data sets were subsequently processed using the CCP4 software package [55]. Molecular replacement was performed using MOLREP [56] with the coordinates of 4-hydroxy-2-oxo-heptane-1,7-dioate aldolase (HpcH) from *E. coli* (45% sequence identity to asHPAL; PDB ID, 2v5j) [46] as a search model. The automatic chain tracing using ARP-wARP [57] was used to build almost the entire sequence. Alternate cycles of refinement were performed using WinCoot [58] and Refmac5 [59]. The final model of asHPAL was evaluated by PROCHECK [60].

All figures for asHPAL structures were prepared using PyMOL [16]. The search for similar structures was performed using the Dali server [61], and the RMSD values for superimposed structures were calculated using the Dali pairwise comparison service [62].

2.3 Results and discussion

2.3.1 Expression and purification of asHPAL

After optimizing expression conditions, asHPAL expression was induced by the addition of IPTG to a final concentration of 0.5 mM when the optimal density at 600 nm reached 0.6, and the cells were then cultivated at 293 K for 16 h. The cultivated cells were harvested by centrifugation at 5,000 $\times g$ at 277 K for 20 min. The cell pellets were rapidly frozen in liquid nitrogen and stored at 193 K.

Soluble and insoluble fractions were separated by centrifugation after cell lysis. The supernatant was loaded onto a Ni-Sepharose 6 Fast Flow (GE Healthcare) column. The eluate was analyzed by SDS-PAGE (Fig. 2-2). The results showed that the eluate contained abundant asHPAL and small amounts of other proteins. Further purification was performed by anion-exchange chromatography to remove the contaminants. A major peak was observed in the resulting chromatogram at the NaCl concentration of 42% (Fig. 2-3A). The three fractions comprising the major peak were assessed by SDS-PAGE (Fig. 2-3B). The results showed that the major peak primarily contained asHPAL; however, small amounts of other proteins remained in the major peak. According to the shape of the major peak, the purified asHPAL was not electrostatically heterogeneous, but the small peak appeared to overlap with the major peak. The first two fractions were chosen to avoid the small peak and were used for crystallization and other assays. After concentration, the yield of soluble asHPAL was 15 mg per one liter of *E. coli* culture.

2.3.2 Oligomeric state of asHPAL

In the size-exclusion chromatography of asHPAL, a major peak was observed at an elution

volume from 10.5 ml to 14.5 ml (Fig. 2-4A). The elution volume of the peak top was estimated to be 12.8 ml, although the peak top was difficult to discern due to the high intensity. Compared with the elution volume of standard proteins for calibration, the molecular weight of asHPAL (27.1 k) was calculated to be 160 k in solution (Fig. 2-4B) [63]. The estimated molecular weight suggested that asHPAL formed a homo-hexamer in solution.

2.3.3 Stereoselective activity of purified asHPAL

asHPAL catalyzes the aldol reaction between 2-ketobutyrate and acetaldehyde to produce HMKP. It is difficult to detect HMKP directly because it is unstable. The coupled reaction with the aminotransferase, BCAT, has been proposed to detect HMKP indirectly (Fig. 2-5) [51]. In the reaction process, BCAT immediately converts HMKP to 4-HIL, which is a stable compound. BCAT also produces the byproducts 2-ketoglutarate, 2-aminobutyrate, and 2-ketobutyrate. The enantioselective detection of 4-HIL in the reaction mixtures was performed using chromatography with a chiral column, and 4-HIL was acquired for derivatization using GITC.

The chromatogram of the reaction mixture is shown in Fig. 2-6A. Four major peaks were detected on the chromatogram, which is expected because GITC derivatizes the compounds with an amino group, thus producing L-Glu (peak 1), (2*S*,3*R*,4*R*)-4-HIL (peak 2), (2*S*,3*R*,4*S*)-4-HIL (peak 3), and 2-aminobutyrate (peak 4). The peaks were assigned by comparison with pure (2*S*,3*R*,4*S*)-4-HIL (Fig. 2-6B), pure L-Glu (Fig. 2-6C), and a control mixture without acetaldehyde, in which 4-HIL was not produced (Fig. 2-6D). Peaks 2 and 3 were further analyzed by ESI-TOF-MS (Fig. 2-7 A and B). The results showed a single peak with m/z 537.21, which was consistent with the m/z value of protonated GITC-4-HIL ($[M+H]^+$, m/z 537.21). These results indicated that the recombinant asHPAL had the ability to produce (3*S*,4*S*)-HMKP and (3*S*,4*R*)-HMKP, which were detected as GITC-(2*S*,3*R*,4*R*)-4-HIL (peak 2) and GITC-

(2*S*,3*R*,4*S*)-4-HIL (peak 3), respectively.

Further HPLC analyses were performed on the reaction mixtures at pH 6.0, 7.0, and 8.0 (Fig. 2-8 and Table 2-1). Both of the peaks of GITC-(2*S*,3*R*,4*R*)-4-HIL (peak 2) and GITC-(2*S*,3*R*,4*S*)-4-HIL were observed in the chromatograms, which showed that asHPAL catalyzes the reaction under pH values from 6.0 to 8.0. The concentrations of each 4-HIL enantiomer were calculated from the areas of peaks 2 and 3, and the results are summarized in Fig. 2-9. The ratios of (2*S*,3*R*,4*S*)-4-HIL to (2*S*,3*R*,4*R*)-4-HIL were elevated under decreased pH. These results are consistent with a previous report in which the activities were detected as the asHPAL separated from *Arthrobacter simplex* strain AKU 626 [51].

2.3.4 Crystallization of asHPAL

asHPAL crystals were obtained with the reservoir solution containing 100 mM HEPES (pH 7.5), 30% (v/v) PEG 400, and 200 mM MgCl₂ at 293 K. After 2D grid optimization of crystallization conditions, the best crystals of asHPAL were reproducibly obtained with the reservoir solution containing 100 mM HEPES-Na (pH 7.7), 30% (v/v) PEG 400, and 200 mM MgCl₂ at 293 K (Fig. 2-10) for 1 day.

2.3.5 Data collection and structure determination

The crystals obtained at pH 7.7 diffracted X-rays to 1.60 Å resolution (Fig. 2-11). The asHPAL crystals belonged to space group *C*2, with unit cell parameters $a = 116.8$ Å, $b = 88.2$ Å, $c = 85.3$ Å and $\beta = 122.3^\circ$. The Matthews coefficient (V_m) was estimated at 2.17 Å³ Da⁻¹ [64], which indicated that the crystals contained three asHPAL molecules per asymmetric unit with solvent contents of 43.4%.

The structure of asHPAL was determined at 1.60 Å resolution by a molecular replacement

method using the atomic coordinates of HpcH (45% sequence identity to asHPAL; PDB ID, 2v5j) [46] as a search model. After density modification, automated model building, manual rebuilding and the addition of Mg^{2+} and water molecules using COOT and the CCP4 program suite, the final crystal structure was refined to $R_{work} = 17.3\%$ and $R_{free} = 19.5\%$. An asymmetric unit of the crystal contained three asHPAL molecules constituting the residues 1–259, three Mg^{2+} ions, and 786 water molecules. PROCHECK analysis showed that 94.9% of the residues were in the most favored region and that the remaining residues were in the additionally allowed region of a Ramachandran plot. The refinement statistics are summarized in Table 2-2.

2.3.6 Overall structure of asHPAL

asHPAL adopted a $(\beta/\alpha)_8$ triosephosphate isomerase (TIM) barrel fold (Fig. 2-12), which was characterized by a central barrel formed by parallel β -sheets and 8 α -helices surrounding the central barrel. There were three asHPAL molecules per asymmetric unit. The 259 C α atoms of chains A and B were superposed with a root-mean-square deviation (RMSD) of 0.201 Å, whereas the RMSD between chains A and C was 0.170 Å (Fig. 2-13). Mg^{2+} was observed in the central barrel and was coordinated with oxygen atoms of Glu156, Asp182, and four water molecules (Fig. 2-14). Because class II aldolases use the divalent metal ion to stabilize the interaction between substrate and enzymes, the position of Mg^{2+} was considered to be the active site of asHPAL.

asHPAL adopted a homohexamer conformation, which was formed by the crystallographic twofold rotational symmetry of an asHPAL homotrimer in an asymmetric unit (Fig. 2-15). There were predominantly hydrophilic contacts between the two subunits in the homotrimeric part (Fig. 2-16). The hydrophilic contacts were composed of Ala50, Glu51, His52, Thr59, Pro79, Arg134, and Arg251 from one subunit and Glu58, Lys87, Gln88, Asp91, and Phe135 from the

neighboring subunit. The residues Tyr55, Val80, and Pro118 were involved in the hydrophobic contacts. In the interface between two homotrimeric parts, hydrophilic contacts were also predominant and were composed of Thr33, Glu36, Arg65, Tyr70, Arg131, and Arg134 on the domain-swapped helix 8 (Fig. 2-17). The hydrophobic contacts were formed by the residues Val5, Ile37, Ser40, and Phe135. The homo-hexamers were supported by the results of size exclusion chromatography (Fig. 2-4) and were considered to contribute to the stabilization of the asHPAL structure due to the additional contacts among subunits, as mentioned above. Moreover, the Mg^{2+} was located at the interface between two asHPAL molecules (Fig. 2-18), indicating that the homo-hexamers formation may be important in the reaction process.

2.3.7 Structural comparison of asHPAL with the other enzymes of the HpaI/HpcH-aldolase subfamily

A structural similarity search using the DALI server [61] revealed that the structure of asHPAL protomer was similar to the enzymes of the HpaI/HpcH-aldolase subfamily, HpcH (Z-score, 37.5; RMSD, 1.5 Å; number of C_{α} atoms, 257), YfaU (Z-score, 37.5; RMSD, 1.3 Å; number of C_{α} atoms, 256), and YhaF (Z-score, 37.5; RMSD, 1.2 Å; number of C_{α} atoms, 252) (Table 2-3). The other proteins with similar structures to asHPAL were HpcH/HpaI aldolase from *Desulfitobacterium* (Z-score, 31.2; RMSD, 1.8 Å; number of C_{α} atoms, 249) and macrophomate synthase from *Macrophoma* (Z-score, 27.3; RMSD, 2.3 Å; number of C_{α} atoms, 250). These proteins were classified into the enzymes of the HpaI/HpcH-aldolase subfamily; however, their functions were not reported. The searched enzymes possessed similar structures that were composed of the TIM barrel fold (Fig. 2-19). Although the TIM barrel fold is one of the most common protein folds, the enzymes with the TIM barrel fold showed diverse activities [65].

The catalytic mechanisms of HpcH, YfaU, and YhaF have been proposed in previous reports [43, 44, 46, 47]. The active site of asHPAL was superposed with those of HpcH, YfaU, and YhaF (Fig. 2-20). asHPAL shared the residues involved in the catalytic reaction of HpcH, YfaU, and YhaF as His52, Arg77, Glu156, and Asp182 [44, 47], indicating that asHPAL may have the same reaction mechanism as the HpaI/HpcH-aldolase subfamily. However, asHPAL has greater stereoselectivity than YfaU or YhaF [35]. In the superposed structures of the active site, two residues of asHPAL, Phe26 and Asn219, were different from the residues of YfaU and YhaF. These structural differences may affect the stereoselectivity of the HpaI/HpcH-aldolase subfamily.

2.4 Conclusion

The method for asHPAL preparation was established by optimizing expression and purification conditions. The purified asHPAL was electrostatically homogeneous, and the purity was estimated to be >98% based on SDS-PAGE. Size-exclusion chromatography showed that asHPAL adopted a stable homohexamer conformation in solution. The HPLC experiments using a chiral column indicated that the recombinant asHPAL catalyzed the aldol reaction to produce two enantiomers of HMKP. The purified protein could then be used in other assays to characterize its enzymatic activity in detail.

The asHPAL crystals were obtained using the recombinant protein, and the crystal structure of asHPAL was determined at 1.60 Å resolution, which is the highest resolution among the structures of the enzymes of the HpaI/HpcH-aldolase subfamily. The structure adopted a $(\beta/\alpha)_8$ triosephosphate isomerase (TIM) barrel fold, and Mg^{2+} was observed in the structure. Because the HpaI/HpcH-aldolase subfamily uses the divalent metal ion to stabilize the interaction between substrate and enzymes, the position of Mg^{2+} was predicted to be the active site of asHPAL. The structure of asHPAL was aligned with those of other HpaI/HpcH-aldolase subfamily members—HpcH, YfaU, and YhaF. The results showed that the active site residues were spatially conserved among the aldolases, indicating that the catalytic mechanism of asHPAL may be similar to that of HpcH, YfaU, and YhaF. However, the differences in stereoselectivity suggested some differences at the active site of asHPAL compared with those of the other enzymes. This interesting point will be described in the next chapter.

Table 2-1 Relative production of the 4-HIL stereoisomers in asHPAL/BCAT bienzymatic reaction under different pH conditions

		4-HIL production (mM)		
aldolase	pH	(2 <i>S</i> ,3 <i>R</i> ,4 <i>S</i>)-4-HIL	(2 <i>S</i> ,3 <i>R</i> ,4 <i>S</i>)-4-HIL	ρ^a
Wild	pH 6	7.1 ± 0.3	1.1 ± 0.2	6.5
	pH 7	8.7 ± 0.6	2.3 ± 0.3	3.8
	pH 8	6.1 ± 0.5	2.5 ± 0.1	2.4

^aThe relative production of 4-HIL isomers was calculated as (2*S*,3*R*,4*S*)-4-HIL / (2*S*,3*R*,4*S*)-4-HIL.

Table 2-2 Data collection and refinement statistics of asHPAL.

<i>Data collection</i>	
X-ray source	PF BL5A
Wavelength (Å)	1.00000
Space group	<i>C2</i>
Unit cell dimensions (Å)	$a = 116.8, b = 88.2, c = 85.3$
(°)	$\beta = 122.3$
Resolution (Å)	70.3–1.60 (1.64–1.60) ^a
Observed reflections	350730
Unique reflections	95766
Completeness (%)	99.4 (98.0) ^a
R_{meas} (%) ^b	4.2 (22.5) ^a
$I/\sigma(I)$	19.44 (4.97) ^a
 <i>Refinement</i>	
Resolution (Å)	70.3–1.60
$R_{\text{work}} / R_{\text{free}}$ (%) ^c	17.3 / 19.5
RMSD bond length (Å)	0.006
RMSD bond angle (°)	1.072
Ramachandran plot (%)	
Favored	94.9
Additionally allowed	5.1
Generously allowed	0
disallowed	0

^a Values in parentheses are for highest-resolution shell.

^b $R_{\text{meas}} = \sum_{hkl} [(\sum_i |I_i - \langle I \rangle) / \sum_i |I_i|]$.

^c $R_{\text{work}} = (\sum_{hkl} ||F_o| - |F_c||) / \sum_{hkl} |F_o|$. R_{work} was calculated with 95% of the data used for refinement, and R_{free} was calculated with 5% of the data excluded from refinement.

Table 2-3 Structural alignment of asHPAL and related structures.

Protein	PDB ID	Z-score	RMSD	Seq. identity (%)	Number of C ^α atoms superimposed
2,4-dihydroxyhept-2-ene-1,7-dioic acid aldolase (HpcH)	2v5k	37.5	1.5	45	257
2-keto-3-deoxy sugar aldolase (YfaU)	2vwt	37.5	1.3	40	256
2-dehydro-3-deoxy-galactarate aldolase (YhaF)	1dxk	37.5	1.2	38	252
HpcH/HpaI aldolase from <i>Desulfitobacterium hafniense</i> DCB-2	3qz6	31.2	1.8	27	249
macrophomate synthase from <i>Macrophoma commelinae</i>	1izc	27.3	2.3	22	250

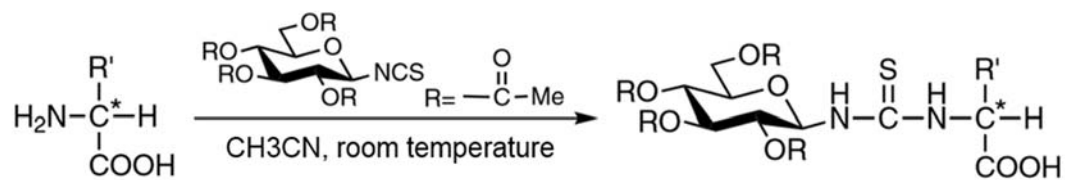


Fig. 2-1 Reaction scheme in the derivatization of amino group using GITC [54]

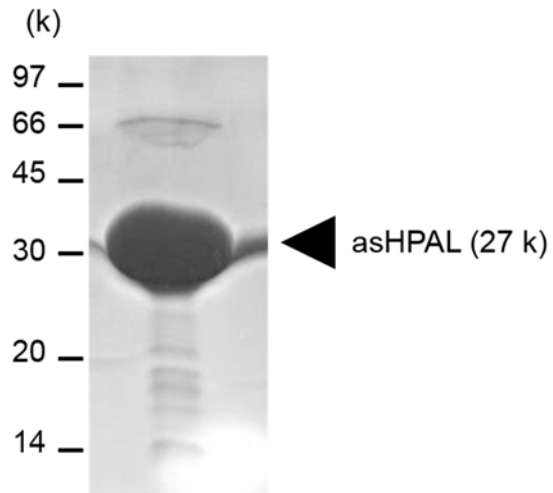


Fig. 2-2 Proteins contained in the eluate after purification using Ni-Sephrose 6 Fast Flow.

Each protein was separated by SDS-PAGE and was visualized by Coomassie staining.

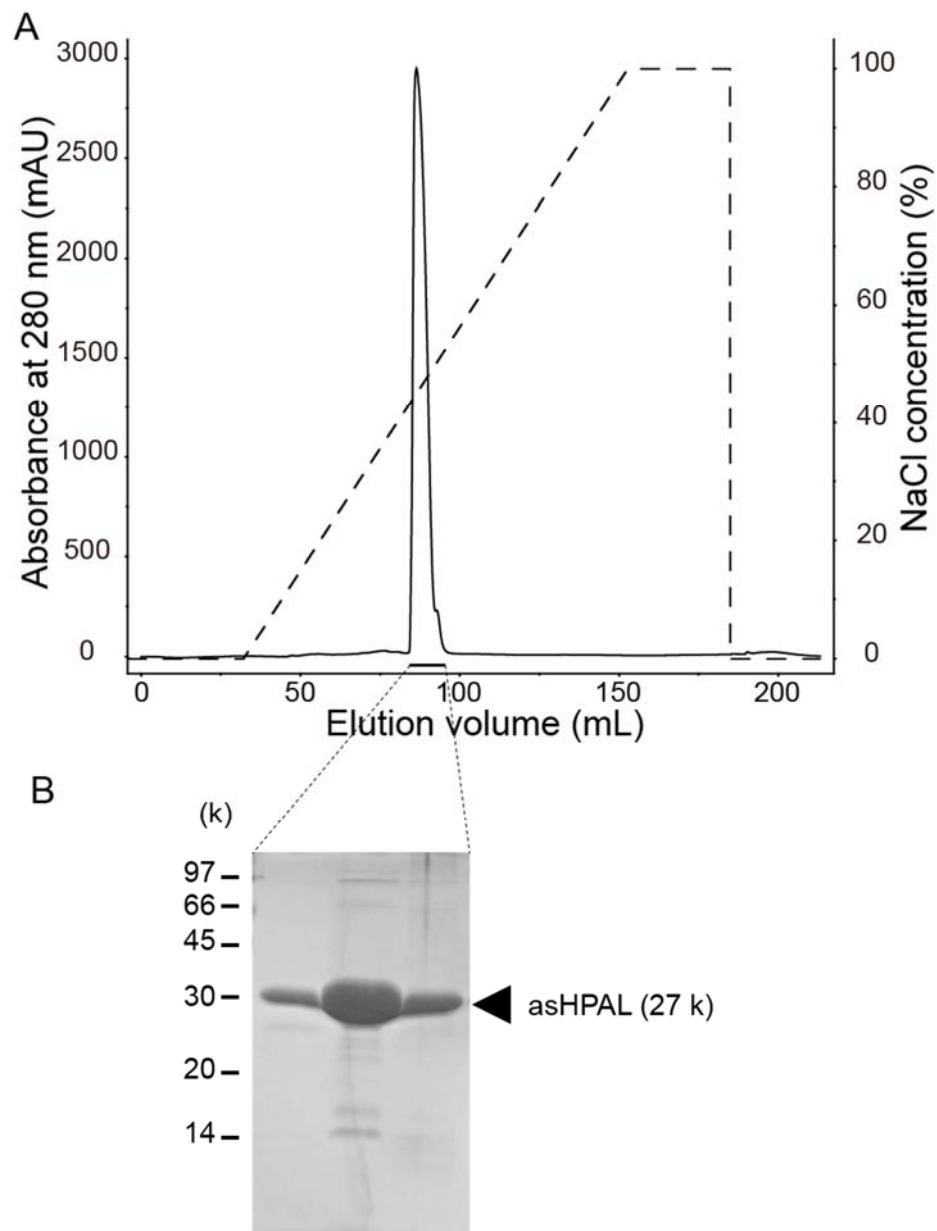


Fig. 2-3 Purification of asHPAL using anion-exchange chromatography.

(A) Chromatogram for purification of asHPAL using Resource Q 6-ml column.

(B) Proteins contained in the eluates of the major peak. Each protein was separated by SDS-PAGE and was visualized by Coomassie staining.

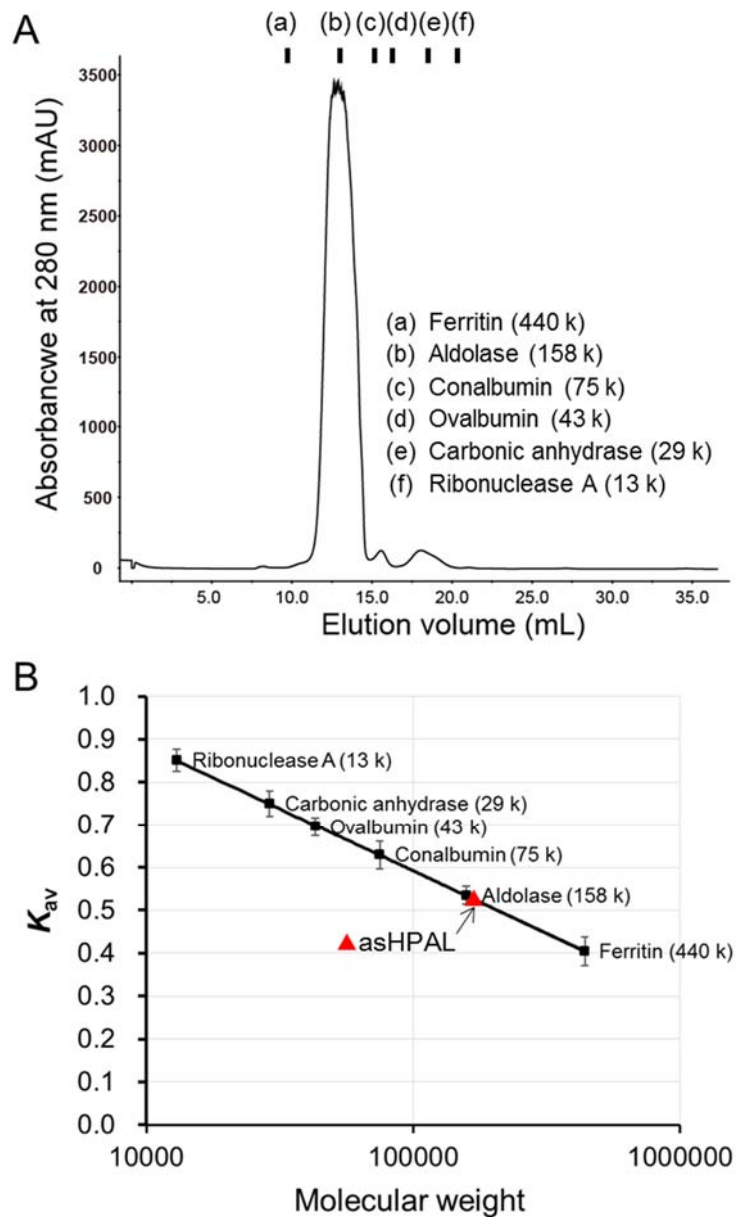


Fig. 2-4 Oligomeric state of asHPAL in solution.

(A) Chromatogram of purified asHPAL. The proteins were separated using 10/300 GL column equilibrated with 20 mM Tris-HCl (pH 7.5), 300 mM NaCl and 1 mM DTT. The elution volume of the major peak was estimated to be 12.8 ml, which corresponds to the average partition coefficient (K_{av}) of 0.53.

(B) Calibration curve for calculating molecular weight from the elution volume of the chromatogram shown in panel (A). The molecular weight of asHPAL is estimated to be 160 k using the calibration curve.

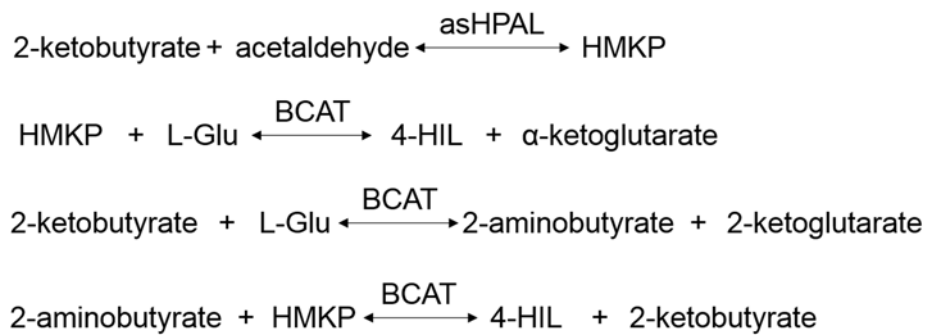


Fig. 2-5 Reactions in the mixture containing asHPAL and BCAT [51].
 The reactions were required to detect unstable HMKP as stable 4-HIL.

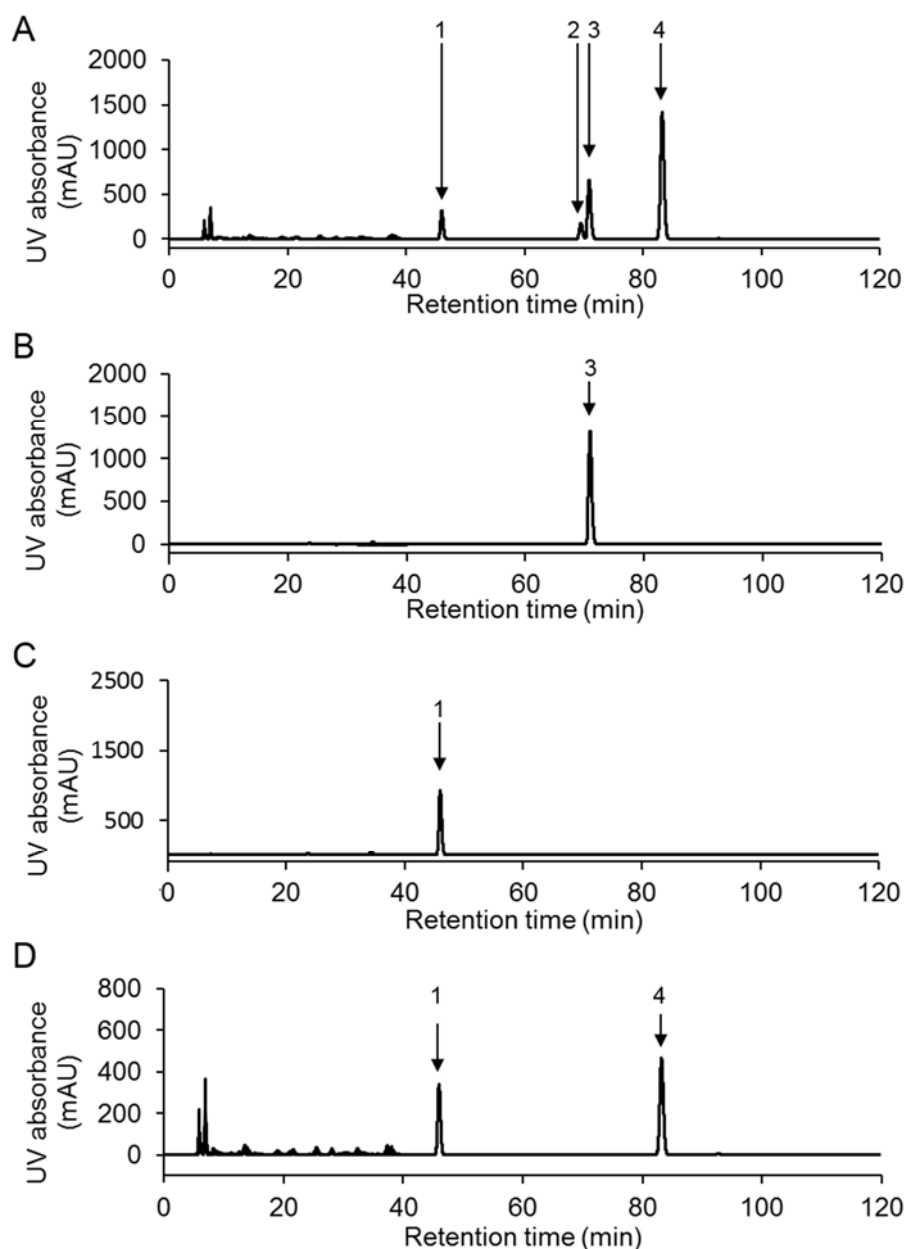


Fig. 2-6 HPLC analysis of asHPAL activity using chiral column.

(A) Reaction mixture containing asHPAL, BCAT and other essential compounds for detecting the asHPAL activity.

(B) Standard solution of (2*S*,3*R*,4*S*)-4-HIL.

(C) Standard solution of L-Glu.

(D) Control mixture. The constitution was the same as the reaction mixture (A) except for acetaldehyde. The reaction did not proceed.

Peak 1, L-Glu; peak 2, (2*S*,3*R*,4*R*)-4-HIL; peak 3, (2*S*,3*R*,4*S*)-4-HIL; and peak 4, 2-aminobutyrate.

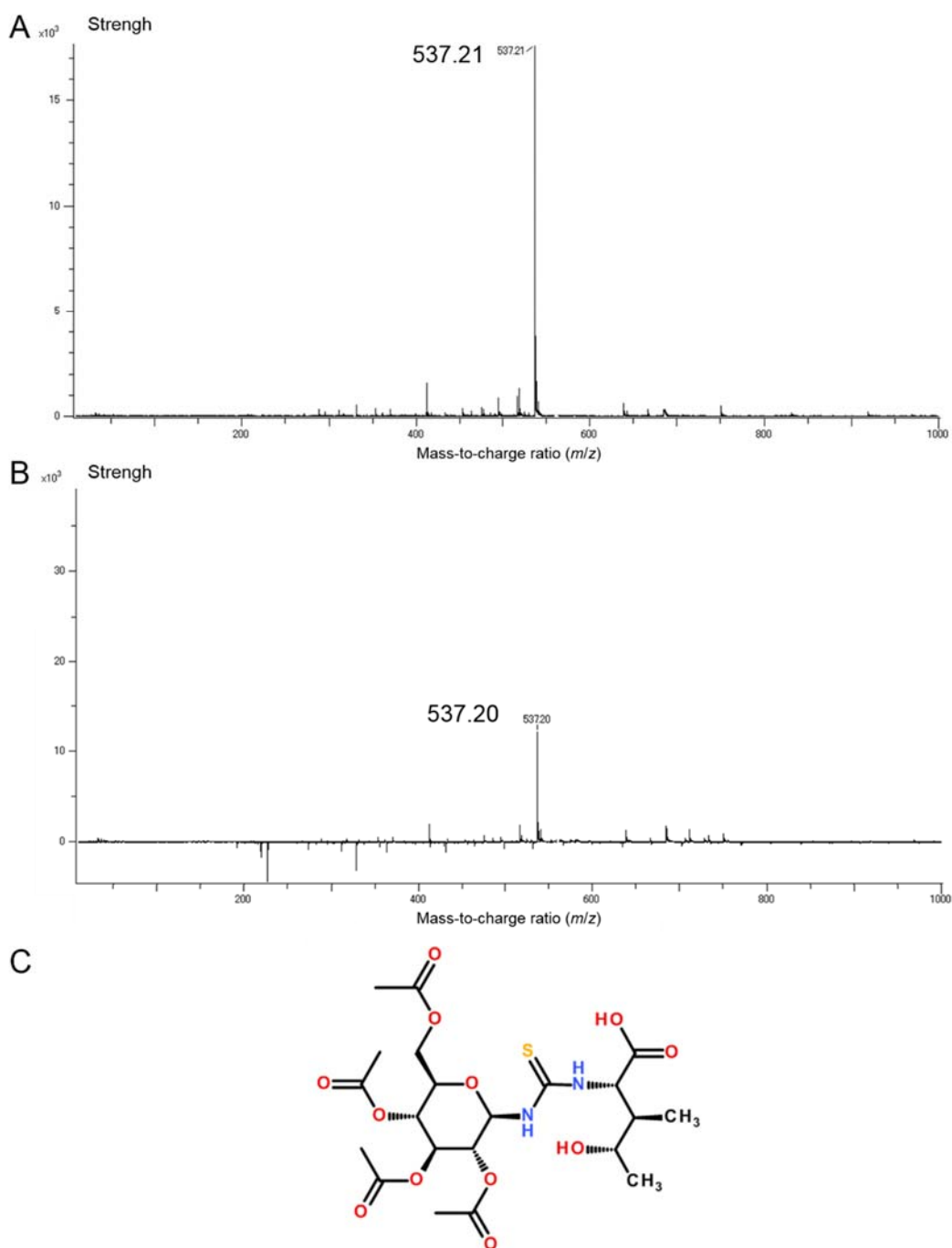


Fig. 2-7 Detection of GITC-4-HIL in the peaks separated by chiral column

(A) MS spectrum of the peak 2 on the chromatogram shown in Fig. 2-6A.

(B) MS spectrum of the peak 3 on the chromatogram shown in Fig. 2-6A.

(C) The structure of GITC-4-HIL.

The derivative was detected with m/z 537.21 as $[M+H]^+$.

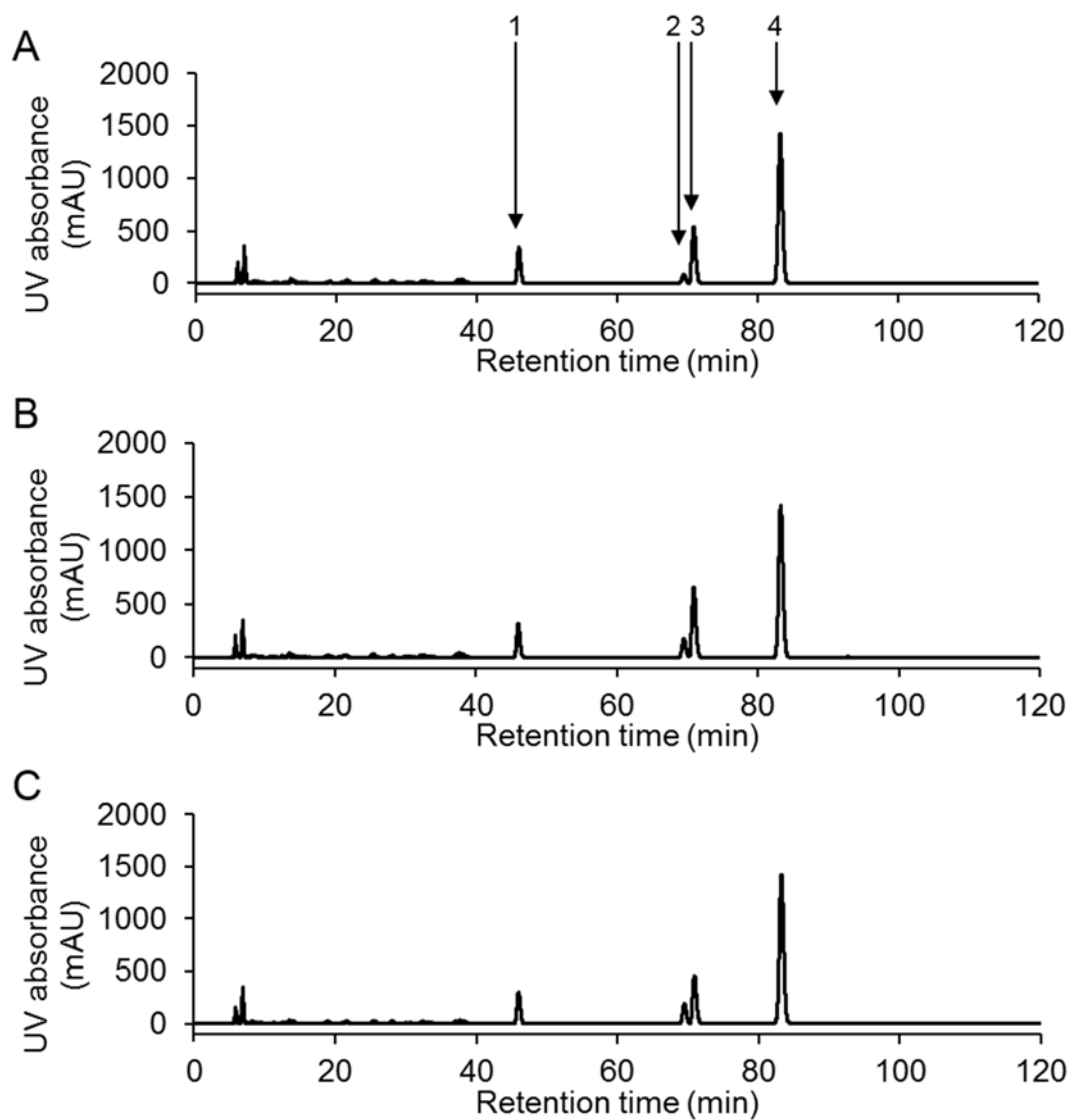


Fig. 2-8 HPLC analysis of asHPAL activity using chiral column at the different pH conditions.

Reaction mixtures were set at pH 6.0 (A), 7.0 (B), and 8.0 (C).

Peak 1, L-Glu; peak 2, (2*S*,3*R*,4*R*)-4-HIL; peak 3, (2*S*,3*R*,4*S*)-4-HIL; and peak 4, 2-aminobutyrate

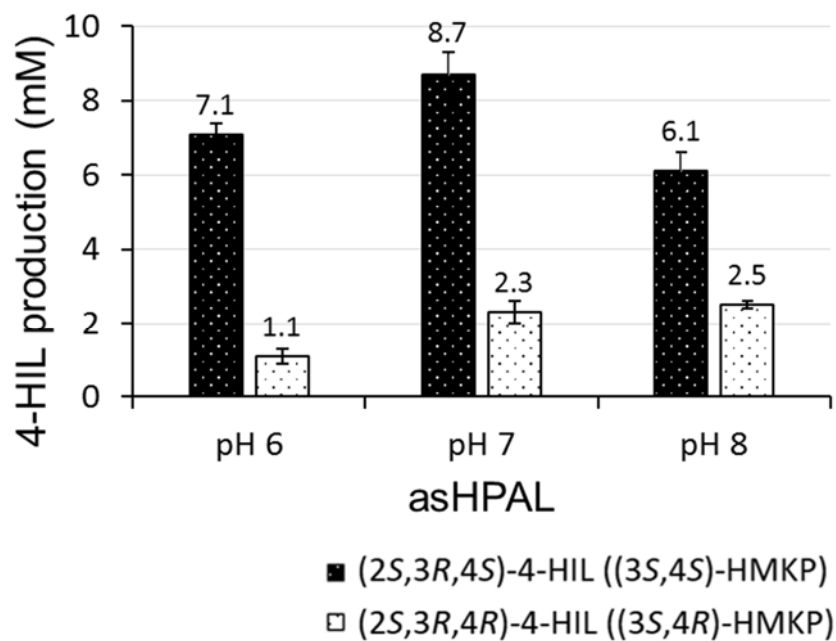


Fig. 2-9 pH dependency of 4-HIL enantiomers produced by the sequential reactions of asHPAL and BCAT

All determinations were performed in triplicate. Error bars show standard deviations.

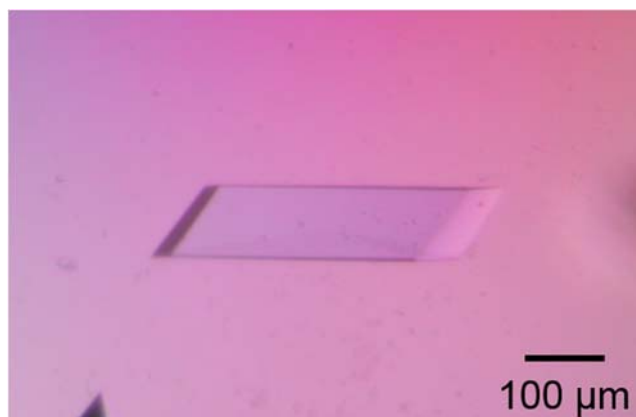


Fig. 2-10 A typical crystal of asHPAL.

The crystal was grown in the reservoir solution containing 100 mM HEPES-Na (pH 7.7), 30% (v/v) PEG 400, and 200 mM MgCl₂ at 293 K for 1 day.

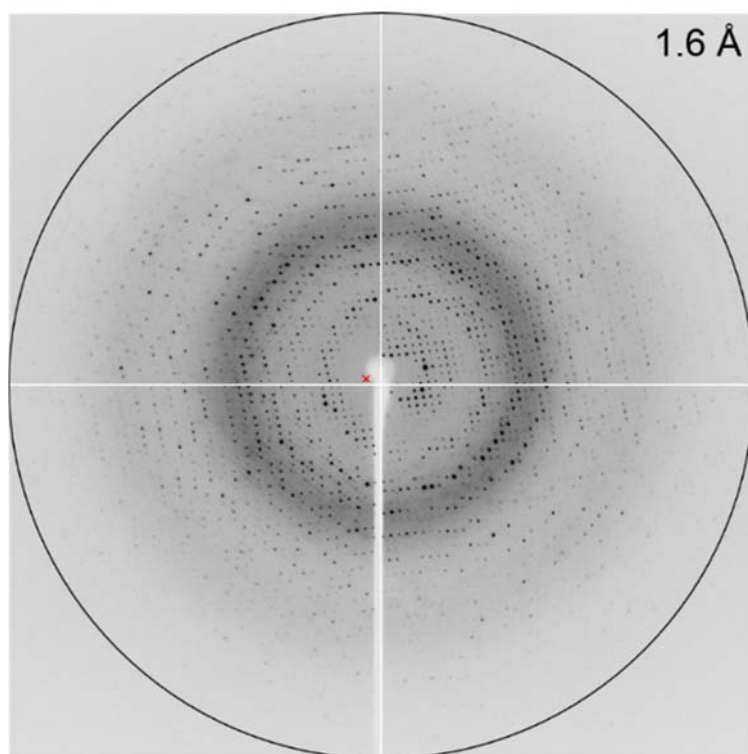


Fig. 2-11 X-ray diffraction image obtained from the asHPAL crystal.

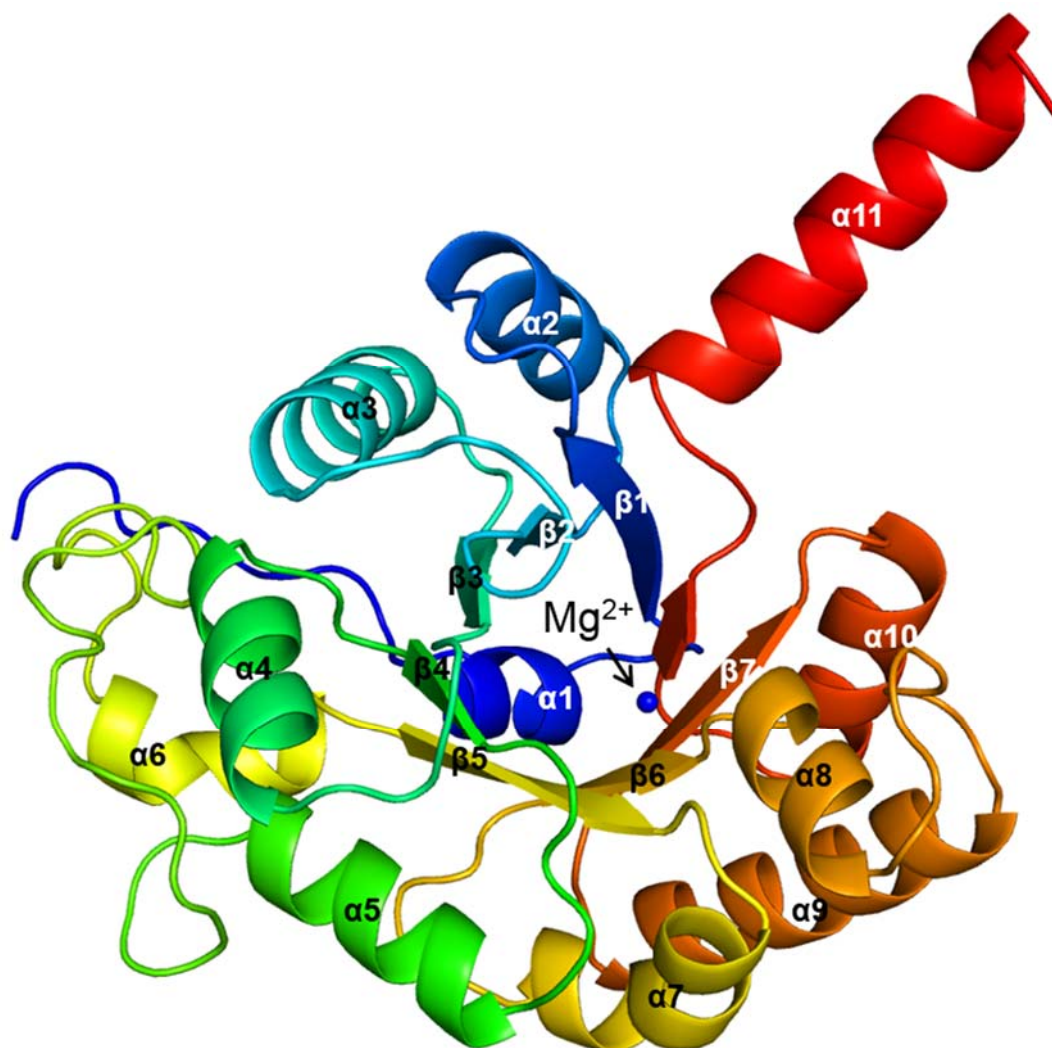


Fig. 2-12 Crystal structure of asHPAL.

asHPAL adopts a $(\beta/\alpha)_8$ triosephosphate isomerase (TIM) barrel fold. Blue sphere represents the Mg^{2+} ion.

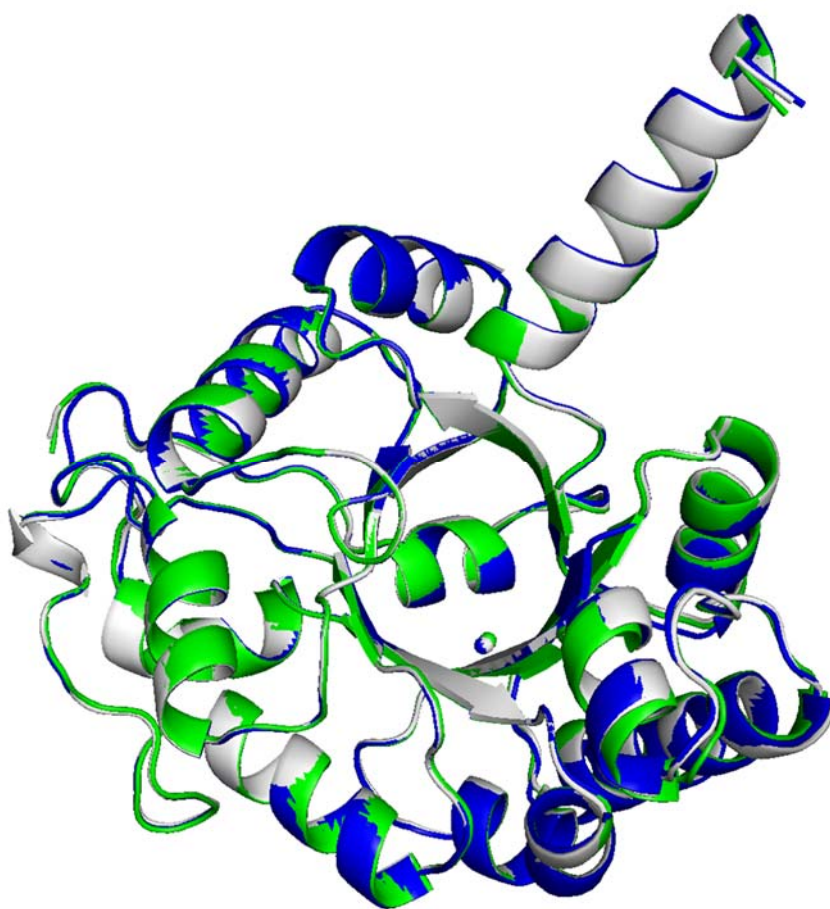


Fig. 2-13 Superposed structures of three asHPAL molecules in an asymmetric unit.

asHPAL and Mg²⁺ in the chains A, B and C are shown in white, blue, and green, respectively. Mg²⁺ is represented with a sphere model.

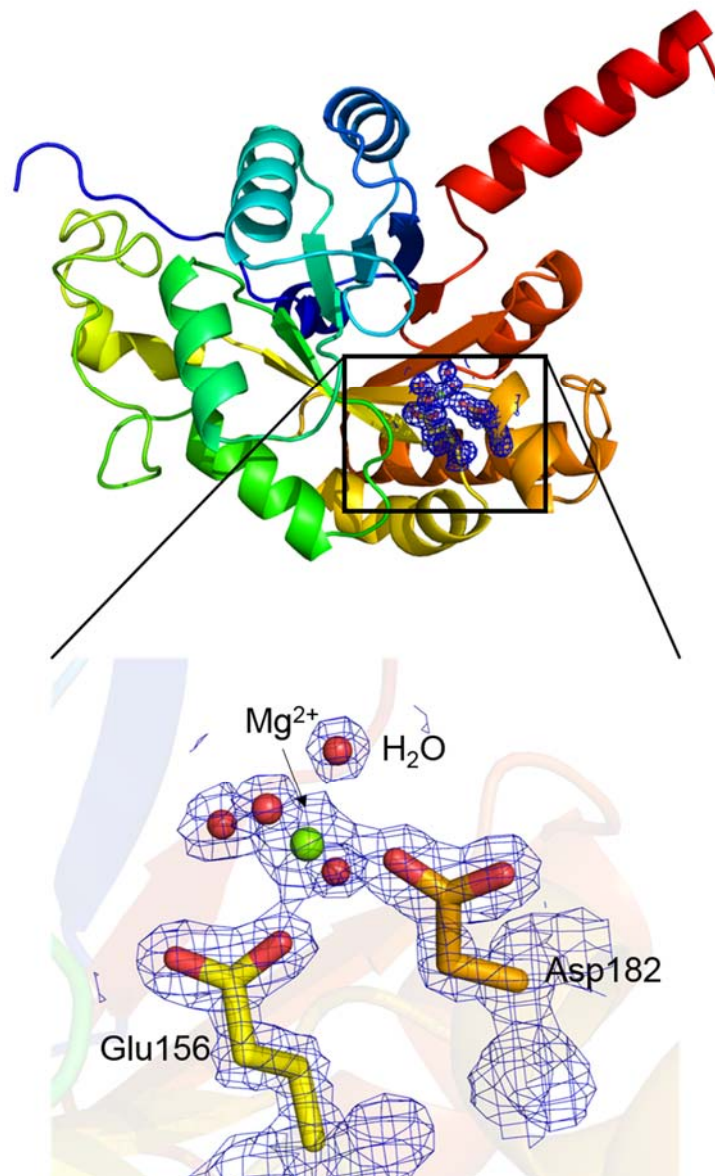


Fig. 2-14 Mg^{2+} coordination with the oxygen atoms of Glu156, Asp182, and four water molecules.

Water molecules are represented by red spheres. Blue mesh showed the $2|F_o|-|F_c|$ omit map (1.5σ).

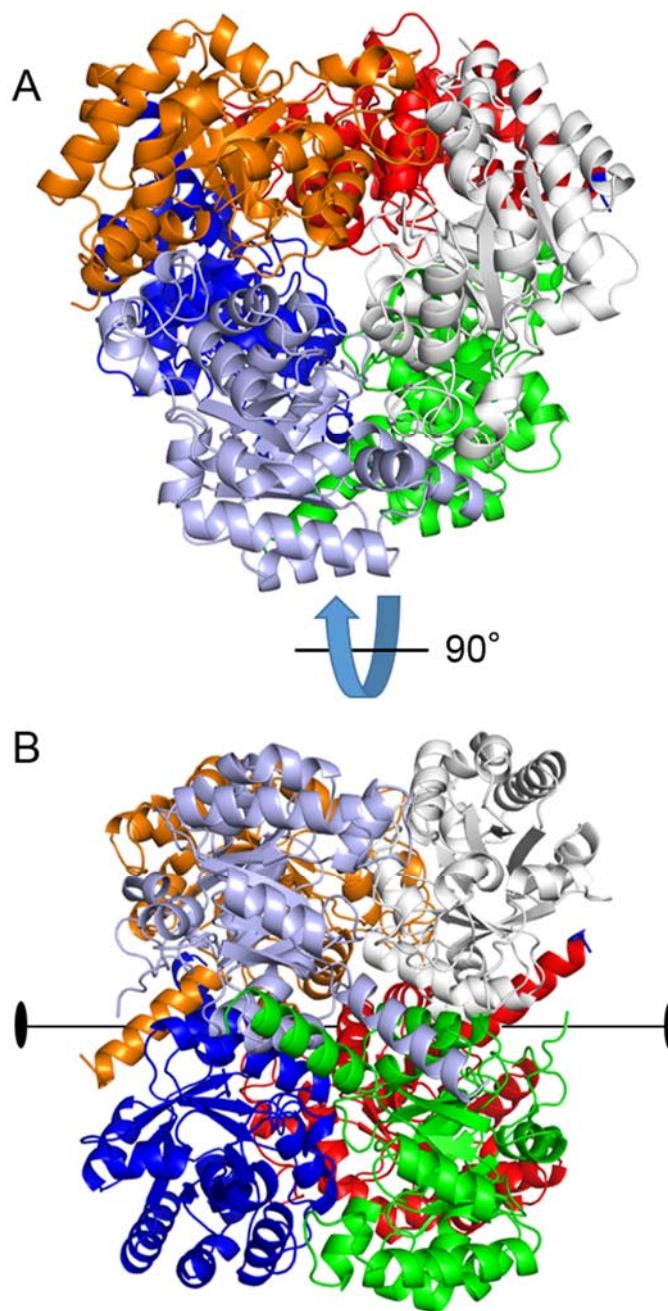


Fig. 2-15 Hexameric structure of asHPAL.

(A) Top view of homohexamer conformation of asHPAL. The molecules colored white, orange and light blue form homotrimer existing in an asymmetric unit.

(B) Side view of homohexamer conformation of asHPAL. The transverse line shows a crystallographic twofold rotational axis.

Individual chains are shown in different colors.

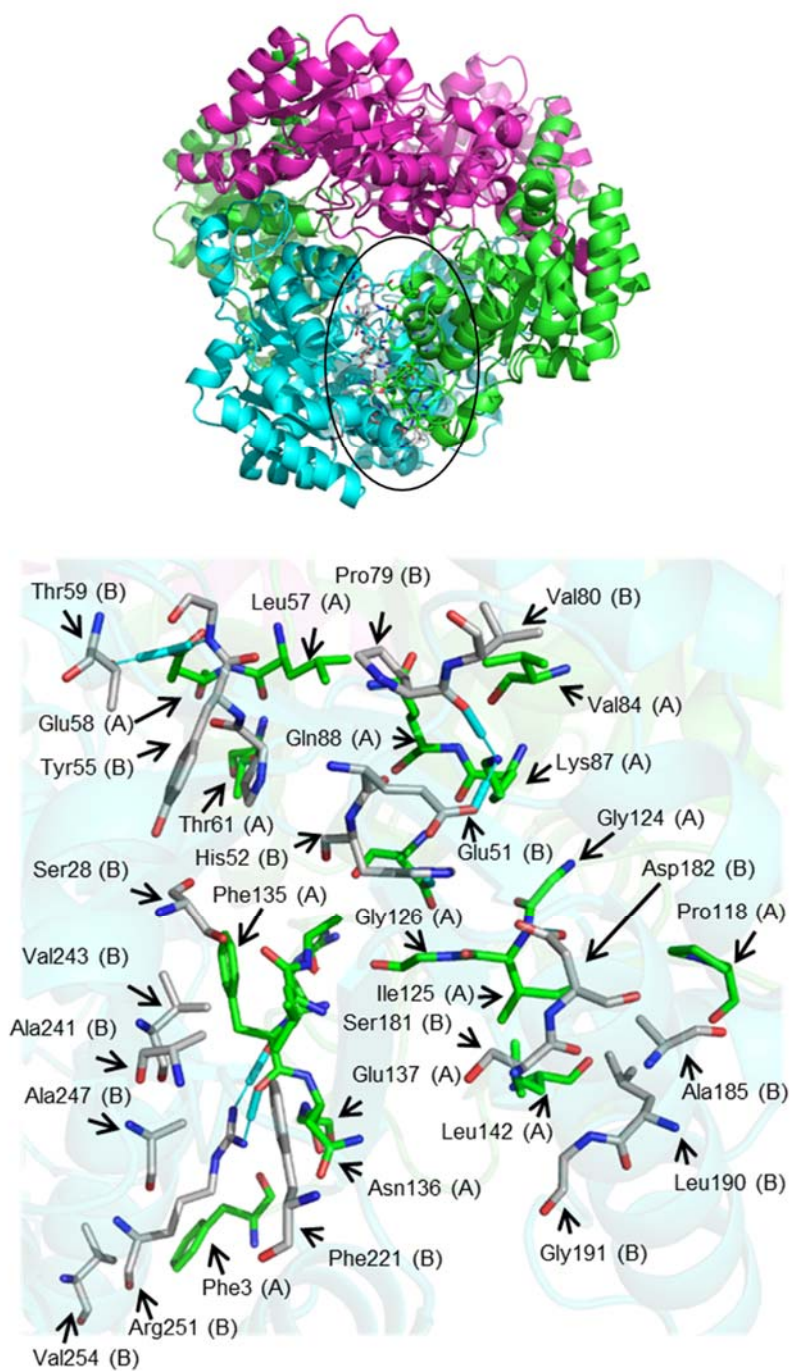


Fig. 2-16 Interactions between two subunits of homotrimer existing in an asymmetric unit.

The residues on a subunit (A) and the neighboring subunit (B) are shown by green sticks and white sticks, respectively. Cyan lines represent hydrogen bonds.

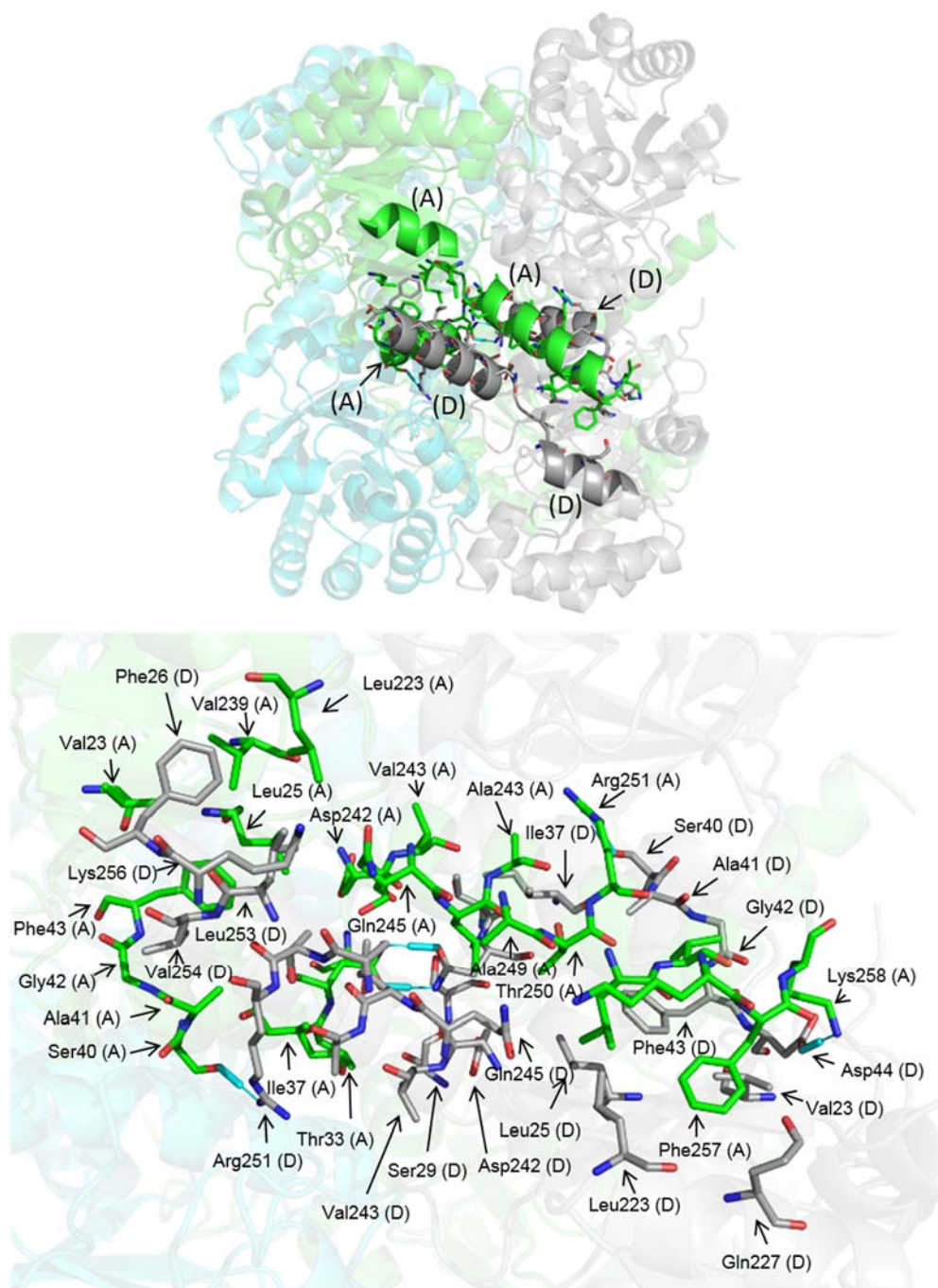


Fig. 2-17 Interactions between the domain-swapped helices.

The residues on a domain-swapped helix (A) and the other domain-swapped helix (D) are shown by green sticks and white sticks, respectively. Cyan lines represent hydrogen bonds.

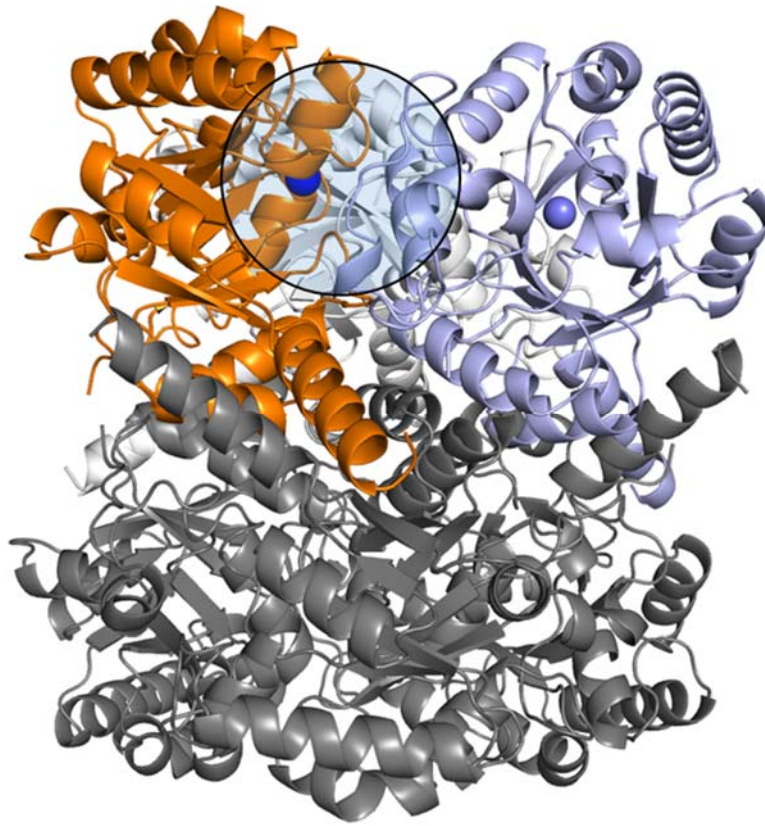


Fig. 2-18 Position of the Mg²⁺ ions between two subunits of homotrimer existing in an asymmetric unit.

Mg²⁺ ions are represented with sphere models, and are located at the interface of two subunits as shown by a circle.

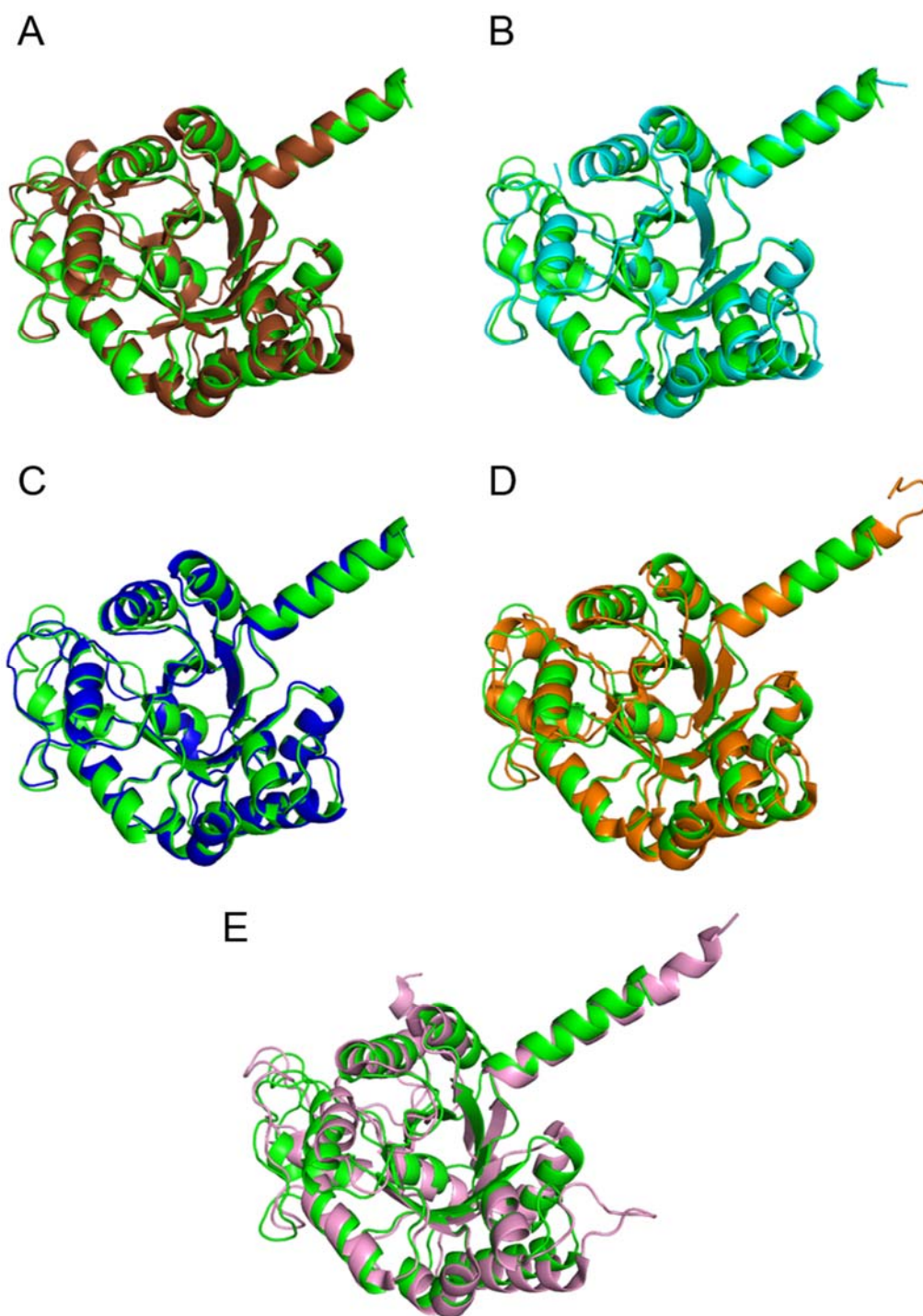


Fig. 2-19 Superposed structures of (A) asHPAL (green) and HpcH (brown), (B) asHPAL and YfaU (cyan), (C) asHPAL and YhaF (blue), (D) asHPAL and HpcH/HpaI aldolase (orange), and (E) asHPAL and macrophomate synthase (pink).

These enzymes share the core structure composed of the TIM barrel fold.

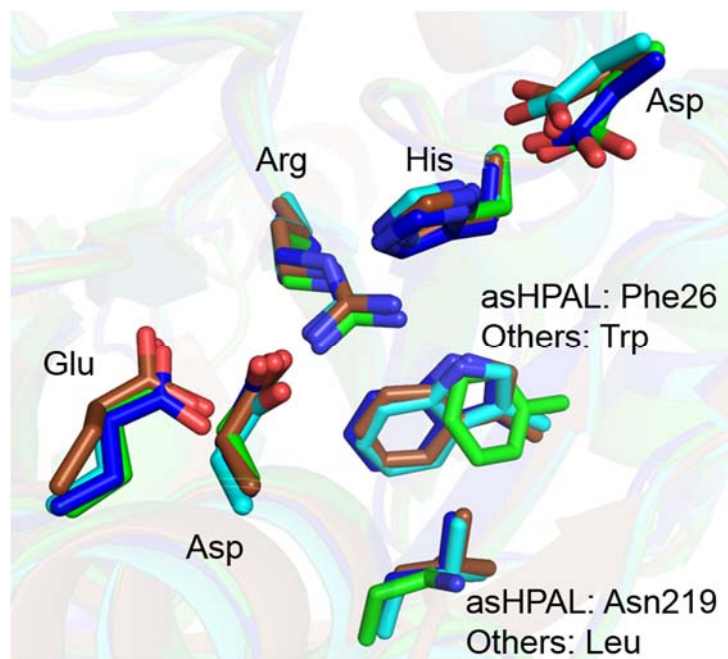


Fig. 2-20 Superposed structures of the active site of asHPAL (green), HpcH (brown), YfaU (cyan) and YhaF (blue).

These enzymes share five residues essential for the reaction. Two residues of asHPAL, Phe26 and Asn219, are different from those of the other enzymes.

Chapter 3

Structural basis for the stereoselective aldol reaction of asHPAL

3.1 Exordium

The structures of enzymes in complex with substrates provide information about their catalytic mechanisms, including the amino acid residues that interact with substrates and form the active sites and the binding states of substrates and reaction intermediates in the active site. However, the enzyme-substrate complex is often unstable due to the progression of the catalytic reaction and the weak and transient recognition of substrates, which makes it difficult to observe the substrates/intermediates binding. In these cases, additional kinetic experiments and computer simulations help us to understand the catalytic mechanisms.

The catalytic mechanism of the HpaI/HpcH-aldolase subfamily in the aldol reaction has been proposed based on the structure of HpcH (Fig. 3-1) [43, 46, 47], as described in Section 1-4. In the active site, there are four water molecules bound with Mg^{2+} , which is coordinated by two acidic residues. One of the water molecules also interacts with the catalytic His residue and is deprotonated to generate a hydroxide ion. The hydroxide ion is speculated to deprotonate the C3 position of pyruvate to promote nucleophilic enolate formation. The nucleophilic enolate attacks the electrophilic C1 atom of acetaldehyde. The reaction is completed by the protonation of the C4 oxygen of the product to form a hydroxyl group. The proposed mechanism helps us understand the aldol reaction catalyzed by the HpaI/HpcH-aldolase subfamily. However, this mechanism does not explain the stereoselectivity of the HpaI/HpcH-aldolase subfamily.

This chapter focuses on the mechanism of the stereoselectivity of asHPAL. The crystal structure of asHPAL in complex with 2-ketobutyrate was determined at 1.58 Å resolution. The structure and additional kinetic data have been improved the catalytic mechanism of asHPAL as a member of the HpaI/HpcH-aldolase subfamily. On the other hand, simulated docking of acetaldehyde to the structure of the asHPAL-2-ketobutyrate complex was utilized to analyze the possible binding mode of acetaldehyde at the active site of asHPAL. The structural basis for

the stereoselective reaction was predicted based on the binding mode and was validated by further enzymatic analyses using asHPAL mutants. An additional structure of asHPAL at pH 6.0 was solved to study the mechanism underlying the pH-dependent stereoselectivity. Finally, mutants were designed to improve the stereoselectivity of asHPAL based on the mechanism of the stereoselective reaction.

3.2 Materials and methods

3.2.1 Crystallization of the asHPAL-2-ketobutyrate complex

The protein was prepared according to the same procedure described in Sections 2.2.3 and 2.2.4. The co-crystallization of asHPAL and 2-ketobutyrate was performed by the vapor diffusion method. Each drop was prepared by mixing equal volumes (2.0 μ l) of the protein solution and the reservoir solution containing 200 mM 2-ketobutyrate, 100 mM HEPES-Na (pH 7.7), 30% (v/v) PEG 400, and 200 mM MgCl₂ and was equilibrated against 400 μ l of the reservoir solution without 2-ketobutyrate at 293 K.

3.2.2 Crystallization of the asHPAL-2-ketobutyrate-acetaldehyde complex

The crystals were prepared by the method described in Section 3.2.1 and were soaked in the reservoir solution containing 200 mM acetaldehyde, 100 mM HEPES-Na (pH 7.7), 30% (v/v) PEG 400, 200 mM MgCl₂, and 200 mM 2-ketobutyrate. The soaking time was 5, 30, or 60 min.

3.2.3 Crystallization of asHPAL at pH 6.0

asHPAL exhibits a higher stereoselectivity toward (3*S*,4*S*)-HMKP at pH 6.0 than at pH 7.0 or 8.0. asHPAL crystals were obtained at pH 6.0 to study the mechanism of pH dependency. The protein was prepared according to the same methods described in Sections 2.2.3 and 2.2.4. Purified asHPAL was dialyzed against 20 mM Bis-Tris (pH 6.0) at 277 K and was concentrated to 10 mg ml⁻¹ using a Vivaspin 20 concentrator (Molecular weight cutoff, 5 k; hydrozart membrane; Vivascience) at 277 K. Initial crystallization trials were performed by the sitting-drop vapor diffusion method using the following sparse-matrix screening kits: Crystal Screen

HT, Index HT (Hampton Research), and Wizard I and II (Emerald Biosystems). Each drop was prepared by mixing equal volumes (0.7 μl) of the protein solution and a reservoir solution and was then equilibrated against 70 μl of the reservoir solution at 277 K or 293 K. After obtaining crystals, the 2D grid optimization of crystallization conditions (pH vs. precipitant concentration) was performed by the sitting-drop vapor diffusion method using 24-well Cryschem plates (Hampton Research). Each drop was prepared by mixing equal volumes (2.0 μl) of the protein solution and a reservoir solution and was then equilibrated against 400 μl of the reservoir solution at 293 K.

3.2.4 Data collection and processing

Each asHPAL crystal was picked up in a nylon loop (Hampton Research) and was transferred to a cryoprotectant solution prepared by mixing 76% (v/v) of the reservoir solution and 24% (v/v) of glycerol. The crystals were mounted on the X-ray diffractometers and were flash-cooled in a cryo-nitrogen stream (95 K).

For the asHPAL crystals obtained in the presence of 2-ketobutyrate, the X-ray diffraction data set (360 images) was collected with synchrotron radiation and an ADSC Quantum 210 detector on BL-26B2 at SPring-8 (Hyogo, Japan). The parameters of data collection were as follows: wavelength, 1.0000 \AA ; total collection angle, 180° ; oscillation angle, 0.5° ; crystal-to-detector distance, 150 mm; and exposure time, 3.7 sec. The diffraction data sets were indexed, integrated, and scaled with the XDS Program Package [66].

For the asHPAL-2-ketobutyrate crystals soaked with acetaldehyde, the X-ray diffraction data set (360 images) was collected with synchrotron radiation and an ADSC Quantum 210 detector on BL-26B2 at SPring-8 (Hyogo, Japan). The parameters of data collection were as follows: wavelength, 1.0000 \AA ; total collection angle, 180° ; oscillation angle, 0.5° ; crystal-to-

detector distance, 150 mm; and exposure time, 1.0 sec. All data sets of the crystals soaked for different times were collected to confirm whether acetaldehyde was bound to asHPAL. The diffraction data sets were indexed, integrated, and scaled with the XDS Program Package [66].

The X-ray diffraction data set (360 images) of the asHPAL crystals obtained at pH 6.0 was collected with an FR-E SuperBright rotating anode generator (Rigaku) and an R-AXIS VII detector (Rigaku). The parameters of data collection were as follows: wavelength, 1.54 Å (Cu $K\alpha$); total collection angle, 180°; oscillation angle, 0.5°; crystal-to-detector distance, 150 mm; and exposure time, 60 sec. The diffraction data sets were indexed, integrated, and scaled with the XDS Program Package [66].

3.2.5 Structure determination and refinement.

Subsequent data processing was performed using the CCP4 software package [55]. Molecular replacement was achieved using the coordinate of asHPAL, which was determined in Section 2.3.5, as a search model with the MOLREP [56]. ARP-wARP [57] was used to perform the automatic chain tracing to build almost the entire sequence. Alternate cycles of refinement were conducted using WinCoot [58] and Refmac5 [59]. PROCHECK [60] was used to evaluate the refinement results. Figures were prepared using PyMOL [16]. The RMSD values for superimposed structures were calculated using Dali pairwise comparison service [62].

3.2.6 Docking simulation of acetaldehyde

All computer simulations were performed using the program suite MOE [67]. The crystal structure of the asHPAL-2-ketobutyrate complex was used as a starting model for the simulations. All water molecules were removed from the model, and the hydrogen atoms were then generated with the Protonate3D module of MOE program. MMFF94x forcefield was used

for the energy minimization. A series of minimizations was performed using the Energy Minimize module with the Tether Atoms set as Heavy, which means that the forcefield is applied to non-hydrogen and non-lone pair atoms.

Site Finder [68] module was used to find the potential binding site of acetaldehyde, and the site located near Mg²⁺, His52, and Arg77 was chosen for the simulated docking of acetaldehyde. The docking simulations for acetaldehyde at the selected site were performed using the ASEDock [69] module in which the forcefield was set to MMFF94x. In the simulation, the docking models were roughly searched with the following parameters: cutoff, 4.5 Å; RMS gradient, 10 kcal mol⁻¹ Å⁻¹; and energy threshold, 500 kcal mol⁻¹. The binding mode of each model was optimized by energy minimization with the following parameters: lowest energy, 5 kcal mol⁻¹; cutoff, 8 Å; and RMS gradient, 0.1 kcal mol⁻¹ Å⁻¹. The obtained docking models were evaluated by the U_dock value, which corresponds to the docking energy.

3.2.7 Site-directed mutagenesis

For the preparation of asHPAL mutants (H52L, R77L, D91L, F26W, F26L, F26Y, and F26N/N219Y), PCR-based site-directed mutagenesis was performed using PrimeSTAR Max DNA Polymerase (Takara). The plasmid for the expression of asHPAL (Section 2.2.1) was used as template. The mutagenic primers were purchased from Operon, and their sequences are summarized in Table 3-1. The PCR was performed with the following cycle parameters: 30 cycles of 98°C for 10 sec, 55°C for 15 sec, and 72°C for 30 sec, followed by cooling to 4°C. The resulting plasmid was amplified in *E. coli* XL1-Blue (Stratagene), and was then extracted from the cells using the Wizard *Plus SV* Minipreps DNA Purification System (Promega). The mutation sites were verified by a DNA sequencing service of FASMAC.

The H52L, R77L, and D91L mutants were expressed as soluble proteins according to the

same method as for the wild-type asHPAL (Section 2.2.3). The F26L, F26W, F26Y, and F26N/N219Y mutants were overexpressed in *E. coli* KRX (Promega) harboring the plasmid for each mutant. The cells were cultivated in LB medium (Merck) containing 30 $\mu\text{g ml}^{-1}$ ampicillin at 310 K. Expression conditions of asHPAL were optimized by changing the induction temperatures (291 K, 298 K, and 310 K) and the concentrations of IPTG (final concentration, 0.1 mM, 0.25 mM, 0.5 mM, and 1.0 mM). Cell lysate was separated by centrifugation and analyzed by SDS-PAGE. The condition to obtain the most soluble and least insoluble target protein was chosen for the extensive expression of asHPAL.

All of the asHPAL mutants were purified using the same method as for the wild-type asHPAL (Section 2.2.4).

3.2.8 Kinetics studies of asHPAL and its mutants

Conventional ultraviolet, visible, and fluorescence spectrophotometry cannot be used for the kinetics studies of asHPAL because 2-ketobutyrate, acetaldehyde, HMKP, and 4-HIL have no characteristic chromophores in their structures. The α -proton signals of 2-ketobutyrate and acetaldehyde were separately observed in the ^1H NMR spectra. The aldol reaction of asHPAL was measured by observing the signals of the two substrates, 2-ketobutyrate (α -proton, m, 2.77 ppm) and acetaldehyde (α -proton, m, 2.16 ppm), on the ^1H NMR spectra of the reaction solution (Fig. 3-2).

All of the reagents were dissolved in deuterium oxide (D_2O , 99.9% D, ISOTEC). The reaction solution was composed of 20 mM MOPS (pD 6.0), 2 mM MgCl_2 , 0.1 mM 3-(trimethylsilyl)-1-propane-1,1,2,2,3,3- d_6 -sulfonate (DDS- d_6) as a quantitative standard, 369 nM asHPAL, and the different concentrations of 2-ketobutyrate and acetaldehyde (Table 3-2). After adding the enzyme to the reaction solution to initiate the reaction, the solution (600 μl)

was immediately moved into a 5-mm NMR tube (Shigemi), and the tube was loaded into the NMR spectrometer.

The ^1H NMR spectra were measured using a Varian Unity INOVA-500 spectrometer (500 MHz of ^1H observation frequency) equipped with a triple resonance probe (Agilent) at 310 K. The acquisition parameters were as follows: number of data points, 56 k; spectral width, 7997 Hz; acquisition time, 3.50 s; delay time, 2.0 s; and number of scans, 32. The ^1H NMR spectra of each reaction solution were recorded 12 times every 3 min 36 s over a period of 43 min 12 s. The first acquisition was initiated 10 min after the addition of the asHPAL solution into the reaction solution. Therefore, the total reaction time was 53 min 12 s. The acquired FID data sets were converted to ^1H NMR spectra by NMRV4 Spectrum software [70]. By comparison with the signal strength of DDS- d_6 , remaining substrate concentrations were calculated as integrated values of the signals.

The reduced substrate concentrations were considered as the produced concentrations of HMKP. The concentration at each detection time was plotted, and the initial velocity of the reaction was measured by the linear fitting of the plotted data. The Lineweaver–Burk plot [71] was used to determine the K_m and V_{\max} of asHPAL, and k_{cat} was calculated using the following formula [72]:

$$k_{\text{cat}} = V_{\max} / [\text{ET}]$$

where [ET] is the concentration of asHPAL in the reaction solution.

3.2.9 Assays for the stereoselectivity of asHPAL mutants

The stereoselectivity of asHPAL mutants were analyzed by HPLC using the method described in Section 2.2.5. The reaction conditions were as follows: 100 mM 2-ketobutyrate, 100 mM acetaldehyde, 2 mM MgCl_2 , 50 μM PLP, 200 mM L-Glu, 369 nM asHPAL, 369 nM BCAT, and 20 mM buffer [Bis-tris (pH 6.0), Tris-HCl (pH 7.0), or Tris-HCl (pH 8.0)]. After

incubation at 303 K for 12 h, the reaction was confirmed by HPLC. The reaction solutions were diluted with 40 volumes of acetonitrile and incubated with 10 mM GITC and 80 mM TEA to derivatize the reaction products for UV detection [54].

Derivatized solution (20 μ l) was loaded onto a CAPCELL C18 MG column (250 mm \times 4.6 mm, 5 μ m; Shiseido) equilibrated with solution A (10 mM KH₂PO₄, pH 2.95) using a Shimadzu 10ATvp HPLC system. The elution was performed with a linear gradient from 0% solution A (10 mM KH₂PO₄, pH 2.95) to 80% solution B (100% acetonitrile) for 120 min, and the flow rate was set at 1.0 ml min⁻¹. The enantiomers, (2*S*,3*R*,4*S*)-4-HIL and (2*S*,3*R*,4*R*)-4-HIL, were separately detected with a UV detector (254 nm) as GITC derivatives. The peak area of the standard was compared to those of the derivatized 4-HIL enantiomers produced by asHPAL to determine the concentrations of enantiomers.

3.3 Results and discussion

3.3.1 Crystallographic analyses of asHPAL and its complex with 2-ketobutyrate

The asHPAL crystals were obtained as co-crystals with 2-ketobutyrate (Fig. 3-3A) and diffracted X-rays to 1.58 Å resolution (Fig. 3-4A). The crystal belonged to the space group *C2* with the unit cell parameters, $a = 116.2$ Å, $b = 88.1$ Å, $c = 85.1$ Å, and $\beta = 122.3^\circ$ (Tables 3-3). The Matthews coefficients of the crystals were 2.21 Å³ Da⁻¹, indicating that the crystals contained three asHPAL molecules per asymmetric unit. However, the electron density of acetaldehyde cannot be observed despite that the X-ray diffraction data were obtained from the asHPAL-2-ketobutyrate crystals soaked with acetaldehyde (data not shown).

The asHPAL crystals at pH 6.0 were obtained with the reservoir solution containing 100 mM Bis-Tris (pH 6.0), 1.5 M (NH₄)₂SO₄, and 100 mM NaCl at 293 K (Fig. 3-3B). The typical crystal diffracted X-rays to 2.15 Å resolution (Fig. 3-4B) and belonged to the space group *P1* with the unit cell parameters $a = 125.3$ Å, $b = 125.3$ Å, $c = 129.9$ Å, $\alpha = 95.3^\circ$, $\beta = 122.3^\circ$, and $\gamma = 93.3^\circ$ (Tables 3-4). The Matthews coefficients of the crystals were 2.19 Å³ Da⁻¹, indicating that the crystals contained three asHPAL molecules per asymmetric unit.

3.3.2 Crystal structure of asHPAL-2-ketobutyrate complex

The structure of the asHPAL-2-ketobutyrate complex was determined at 1.58 Å resolution and was refined to an R_{work} of 18.2% and an R_{free} of 20.0%. Clear electron density was observed for 2-ketobutyrate, which enabled the model building of 2-ketobutyrate (Fig. 3-5). Finally, an asymmetric unit of the crystal contained three asHPAL molecules constituting the residues 1–259, three Mg²⁺ ions, three 2-ketobutyrate molecules, and 705 water molecules. SFCHECK analysis showed that 95.0% of all of the residues were in the most favored region and that the

remaining residues were in the additionally allowed region of a Ramachandran plot. The refinement statistics are summarized in Table 3-3.

There is no significant change in the overall structures of asHPAL or the asHPAL-2-ketobutyrate complex (Fig. 3-6A, C_α RMSD of 0.076 Å). However, Mg^{2+} and the side chain of Glu156 and Asp182 moved toward 2-ketobutyrate because the complex formation also required the interaction between 2-ketobutyrate and Arg77 (Fig. 3-6B). The active site of the asHPAL-2-ketobutyrate complex is shown in Fig. 3-7. Two water molecules (W2 and W3) were coordinated with Mg^{2+} , and the O2 and O3 atoms of 2-ketobutyrate also interacted with Mg^{2+} by coordination bonds (2.2 Å and 2.1 Å, respectively). The water molecule W3 formed hydrogen bonds with the N1 atom of His52 (3.3 Å) and the O3 atom of 2-ketobutyrate (3.0 Å). The N2 atom of His52 interacted with the side chain of Asp91 (2.6 Å) on an adjacent asHPAL molecule through a hydrogen bond. The N1 and N2 atoms of Arg77 formed hydrogen bonds with the O3 atom of 2-ketobutyrate (2.8 Å) and water molecule W4 (2.9 Å), respectively. These hydrogen bonding networks may be important for the catalytic reaction of asHPAL because all networks were formed among 2-ketobutyrate, Mg^{2+} , and the catalytic residues proposed in the HpaI/HpcH-aldolase subfamily—His52, Arg77, and Asp91.

3.3.4 Docking simulation of acetaldehyde

Although I tried to determine the crystal structure of asHPAL in complex with 2-ketobutyrate and acetaldehyde, no electron density of acetaldehyde was observed in the obtained crystallographic data (data not shown). Thus, a docking simulation was used to analyze the possible binding mode of acetaldehyde in the active site of asHPAL. Simulated docking models were selected by the U_dock score. The lower score means that the binding model is more stable. The top 6 stable binding models of acetaldehyde are shown in Fig. 3-8.

When the O1 atoms of acetaldehyde were bound to the side chain of Arg77 in the docking model, the U_dock score was remarkably low compared with the U_dock scores of other binding models. The lowest binding model was chosen as the most suitable model of acetaldehyde among the simulated models.

As shown in Fig. 3-9, the O1 atom of acetaldehyde in model 1 was located at the same position as the oxygen atom of water molecule W4 (Fig. 3-7), which suggested that the O1 atom of acetaldehyde formed a hydrogen bond with the N2 atom of Arg77 (3.1 Å). The distance between the C3 atom of 2-ketobutyrate and the C1 atom of acetaldehyde is 3.1 Å, which is close enough to catalyze the aldol reaction. In addition, the methyl group of acetaldehyde was oriented toward the phenyl ring of Phe26, and a π -CH interaction was predicted to be formed between them.

3.3.5 Kinetics studies of asHPAL

In this study, NMR measurements were used to analyze the kinetics of the enzymatic reaction of asHPAL. As shown in Fig. 3-10, the concentrations of 2-ketobutyrate and acetaldehyde linearly decreased under the optimized reaction conditions, which confirmed that the initial consumption rates of substrates could be estimated as the initial reaction rate of asHPAL by the NMR method. The residues His52, Arg77, and Asp91 were connected with the substrates through hydrogen bonds. Their roles in the catalytic reaction were evaluated by changes in the kinetic parameters of their mutations. Lineweaver–Burk plots of asHPAL and its mutants were drawn by the initial reaction rates measured at different concentrations of the substrates 2-ketobutyrate and acetaldehyde (Figs. 3-11, 3-12, 3-13, and 3-14). The kinetic parameters calculated from the plots are summarized in Tables 3-5 and 3-6.

The kinetic parameters toward 2-ketobutyrate showed that the k_{cat} value of the H52L

mutant was reduced to nearly zero but that the K_m value showed no significant change (Table 3-5). The results suggest that His52 is an essential catalytic residue but not the residue for 2-ketobutyrate binding. In the proposed catalytic mechanism of HpcH and YhaF, the histidine residue corresponding to asHPAL His52 is considered to be a catalytic residue for the deprotonation of a water molecule in the initial step of the catalytic reaction, which was supported by the kinetic data of the H52L mutant in the present study of asHPAL. Compared with wild-type asHPAL, the k_{cat} values of R77L decreased to 20% and 6% toward 2-ketobutyrate (Table 3-5) and acetaldehyde (Table 3-6), respectively. The K_m value toward 2-ketobutyrate did not change by the R77L mutation, but the mutation caused a 12-fold increase of the K_m value toward acetaldehyde. These results indicate that Arg77 affects both the catalytic rate and acetaldehyde binding, which is supported by the results of docking simulations. However, the decreased k_{cat} value and no change of the K_m value in the D91L mutant demonstrated that Asp91 was the residue involved in the control of the catalytic rate (Table 3-6). These data suggest that the formation of a hydrogen bond between His52 and Asp91 could enhance the catalytic potential of His52 as an intersubunit His52-Asp91 dyad. These kinetic data further detail the roles of His52, Arg77, and Asp91 in the aldol reaction of the HpaI/HpcH-aldolase subfamily [43, 44, 46, 47].

3.3.6 Improved catalytic mechanism of the HpaI/HpcH-aldolase subfamily

Based on the crystal structure, docking simulation, and kinetics, I propose the catalytic mechanism of asHPAL (Fig. 3-15), which could improve upon the mechanism proposed in previous reports [43, 44, 46, 47]. The significant decreases of the k_{cat} values of H52L and D91L indicate that the catalytic dyad of His52 and Asp91 has a potential promoting effect on the deprotonation of a water molecule (W3). In the previously proposed model, the water molecule,

which is deprotonated by the histidine residue, directly attacks the C3 atom of 2-ketobutyrate and then promotes the enolate formation of 2-ketobutyrate [44, 47]. However, in the structure of the asHPAL-2-ketobutyrate complex, the distance between the water molecule (W3) connected with His52 and the C3 atom of 2-ketobutyrate is too far for the W3 molecule to attack the C3 atom (4.4 Å). The electron density of W4 molecule was observed only in the structure of asHPAL. This water molecule (W4) located near the C3 atom of 2-ketobutyrate (3.3 Å) interacted with the W3 molecule (2.9 Å). His52 could abstract a proton (H^+) from the C3 atom of 2-ketobutyrate through the W3 and W4 molecules, to promote the enolate formation of 2-ketobutyrate. Docking simulation and kinetic parameters showed that the O1 atom of acetaldehyde bound to the N1 atom of Arg77, which is shared as the binding site of the W4 molecule, and therefore, the W4 molecule could be substituted by the O1 atom of acetaldehyde. In this case, the distance from the C1 atom of acetaldehyde to the C3 atom of 2-ketobutyrate was 3.1 Å, which is near enough to allow nucleophilic attack from the enolate form of 2-ketobutyrate to acetaldehyde. The interaction between Arg77 and two substrates could stabilize the reaction intermediate and ensure that the reaction proceeds. The O4 atom of the intermediate accepts a proton from the N1 atom of His52 through the water molecule W3, thus completing the reaction cycle.

As shown in Fig. 3-16, 2-ketobutyrate immediately converts to the enolate form by supporting the catalytic His52-Asp91 dyad through water molecules in the first step of the reaction. In the enolate form, the O3 atom is negatively charged, which is preferable for coordinating Mg^{2+} . However, the reaction product HMKP adopts the keto form and thus decreases the nucleophilicity of the O3 atom. Thus, the binding of HMKP at the active site is weaker than that of the substrate 2-ketobutyrate, which may enhance the turnover rate of the aldol reaction.

3.3.7 Structural basis for stereoselectivity

Docking simulations suggested that the methyl group of acetaldehyde formed a π -CH interaction with the phenyl ring of Phe26 (Fig. 3-9). This interaction appears to ensure the particular direction of the methyl group of acetaldehyde. In the binding model of acetaldehyde with the lowest U_dock score (Fig. 3-9), the orientation of acetaldehyde is suitable to react with the nucleophilic enolate for a preferable (3*S*,4*S*)-HMKP production. As described in Section 2.3.7, asHPAL has a phenylalanine residue near the active site, but the corresponding residue is substituted by tryptophan in the other the HpaI/HpcH-aldolase subfamily enzymes YfaU and YhaF (Fig. 3-17).

To evaluate the effect of Phe26 on stereoselectivity, the F26W and F26L mutants were tested using the HPLC assay for chiral separation. The activities of these mutants were observed as the peaks of GITC-4-HIL enantiomers on the chromatograms (Figs. 3-18 and 3-19). As shown in Fig. 3-20 and Table 3-8, the stereoselectivity of asHPAL toward (3*S*,4*S*)-HMKP was decreased by the F26W and F26L mutations at the tested pH conditions. The ratios of (2*S*,3*R*,4*S*)-4-HIL to (2*S*,3*R*,4*R*)-4-HIL were 1.0 (5.2 to 5.3, pH 6.0), 1.3 (6.7 to 5.2, pH 7.0), and 2.0 (6.1 to 3.1, pH 8.0) in the F26W mutant. The results were similar to the stereoselectivities of YfaU and YhaF (Fig. 1-3), which possess the tryptophan residue at the position corresponding to asHPAL Phe26. In addition, the F26L mutant of asHPAL exhibited no stereoselectivity toward the two enantiomers (3*S*,4*S*)-HMKP and (3*S*,4*R*)-HMKP. It was concluded that the stereoselectivity of asHPAL was primarily governed by the phenyl ring of Phe26.

The stereoselectivity of asHPAL varies with pH; however, the mechanism remains unclear. To obtain a structural basis for the pH dependency, the asHPAL structure at pH 6.0 was determined at 2.15 Å resolution and was refined to an R_{work} of 19.5% and an R_{free} of 23.3%.

Finally, an asymmetric unit of the crystal contained three asHPAL molecules consisting of the residues 1–259 and 621 water molecules. SFCHECK analysis showed that 93.8% of all the residues were in the most favored region and that the remaining residues were in the additionally allowed region of a Ramachandran plot. The refinement statistics are summarized in Table 3-4.

The overall structure and the residues around the active site were compared between the asHPAL structures at pH 6.0 and pH 7.7. The overall structures showed no significant differences (Fig. 3-21A, C_{α} RMSD of 0.273 Å). In the active site, the orientation of Asp182 was changed in the structure at pH 6.0 (Fig. 3-21B). However, the change was believed to be caused by the absence of Mg^{2+} . Based on the mutational data of Phe26, the stereoselectivity could be defined by the orientation of acetaldehyde at the active site of asHPAL. The orientation is affected by Phe26 and Arg77, which are the residues responsible for acetaldehyde recognition. In general, the pH range from 6.0 to 8.0 does not greatly change electrostatic properties in the side chains of Phe26 and Arg77. However, the configuration of acetaldehyde is known to be affected by pH [73]. As a future study, quantum chemistry calculations will be required to understand the pH dependency of stereospecificity.

3.3.8 Improving the stereoselectivity of asHPAL

Although the exact position of acetaldehyde cannot be confirmed due to the absence of the structure complexed with acetaldehyde, the distance between the methyl group of acetaldehyde and the phenyl ring of Phe26 may not be optimal to form the π -CH interaction. To improve the stereoselectivity of asHPAL, further mutations of the acetaldehyde binding site of asHPAL were created.

First, the effects of the F26Y mutation on stereoselectivity were evaluated. The π -CH

interaction may be changed by introducing a hydroxyl group on the phenyl ring. The HPLC analysis of reaction mixtures containing the F26Y mutant showed a nearly identical pattern as the wild-type asHPAL (Fig. 3-22). The ratios of (2*S*,3*R*,4*S*)-4-HIL to (2*S*,3*R*,4*R*)-4-HIL were 5.8 (6.9 to 1.2, pH 6.0), 3.2 (7.9 to 2.5, pH 7.0), and 2.3 (6.3 to 2.7, pH 8.0) (Fig. 3-25 and Table 3-8). The results showed that the hydroxyl group did not improve the stereoselectivity of asHPAL toward (3*S*,4*S*)-HMKP.

Next, I focused on Asn219 as a mutation site. The phenyl ring introduced by the N219F mutation might form a π -CH interaction with the methyl group of acetaldehyde. However, it was predicted that the phenyl ring could cause steric hindrance with the phenyl ring of Phe26. To avoid such a steric hindrance, the N219Y/F26N double mutant was designed. The side-chain amino group of Asn26 may interact with the hydroxyl group of Tyr219 through a hydrogen bond (Fig. 3-23), which may allow the side-chain conformation of Tyr219 to form the π -CH interaction with the methyl group of acetaldehyde. The HPLC analyses of the N219Y/F26N mutant showed that the ratio of (2*S*,3*R*,4*S*)-4-HIL to (2*S*,3*R*,4*R*)-4-HIL was increased to 10.2 (5.1 to 0.5) at pH 6.0 (Figs. 3-24 and 3-25). The kinetic parameters of the N219Y/F26N mutant were measured toward 2-ketobutyrate and acetaldehyde by NMR at pH 6.0 (Fig. 3-26 and Table 3-7). The k_{cat} value of the N219Y/F26N mutant was almost the same as that of the wild-type asHPAL. However, the K_{m} value toward acetaldehyde was decreased to ~70% of the wild-type enzyme, indicating that the interaction between asHPAL and acetaldehyde was enhanced by the N219Y/F26N mutation. This result may imply that the mutant forms a more suitable π -CH interaction.

3.4 Conclusion

The structure of asHPAL in complex with 2-ketobutyrate was determined at 1.58 Å resolution, which revealed the binding mode of 2-ketobutyrate at the active site. The possible binding mode of acetaldehyde was predicted by docking simulation. Based on these structural findings and the detailed kinetic data, there are three active-site residues involved in acetaldehyde binding (Arg77) and the catalytic reaction (His52, Arg77, and Asp91). The kinetic data also demonstrated that these residues do not affect 2-ketobutyrate binding, indicating that the Mg²⁺ coordination is critical for the binding.

Here, the catalytic mechanism of asHPAL was proposed as follows (Fig. 3-15): (1) The proton (H⁺) at the C3 atom of 2-ketobutyrate is abstracted by the His52-Asp91 catalytic dyad through the water molecules W3 and W4, and then 2-ketobutyrate forms the nucleophilic enolate; (2) Acetaldehyde is replaced with the W4 molecule to interact with Arg77; (3) Attack of the nucleophilic enolate on the electrophilic C1 atom of the acetaldehyde leads to the formation of the intermediate form of HMKP; and (4) The C4 oxygen of the HMKP intermediate captures a proton from His52 through the water molecule W3 to form a hydroxyl group.

The present structural findings also showed that Phe26 could be the residue involved in the stereoselectivity of asHPAL. The loss of stereoselectivity in the F26W and F26L mutants indicated that Phe26 controlled the stereoselectivity to preferably produce (2*S*,3*R*,4*S*)-4-HIL in the coupled reaction with BCAT. Based on the structure, the stereoselectivity of asHPAL was successfully improved by the N219Y/F26N double mutation. However, no differences were observed between the structures determined at pH 6.0 and 7.7, which suggested that quantum chemistry approaches may be required to understand the pH dependency of stereoselectivity.

Table 3-1 Mutagenic primers.^a

Mutants	Forward primer	Reverse primer
H52L	5-gccgag ctct ccccttacggccttgaa-3	5-aggggag gag ctcggcacgataagcag-3
R77L	5-gtggt actg attccagtcaacgacaca-3	5-tggaat cagt accactggggtagcagg-3
D91L	5-tacctg ctct ttgggtgcgcaaacctc-3	5-accca gag caggtactgcttgatcag-3
F26W	5-ggactc ggg atctcgctgggctcggaa-3	5-cgagat ccag agtcctacctgcgcact-3
F26L	5-ggactc ttg atctcgctgggctcggaa-3	5-cgagat caag agtcctacctgcgcact-3
F26Y	5-ggactc tac atctcgctgggctcggaa-3	5-cgagat gtag agtcctacctgcgcact-3
F26N	5-ggactc aac atctcgctgggctcggaa-3	5-cgagat gtt gagtcctacctgcgcact-3
N219Y	5-ggcatc tat gcctcaatctcgcacaa-3	5-gaaggc atag atgccaacgagcttgcc-3

^aLabeled bases are the variation locus.

Table 3-2 Concentrations of 2-ketobutyrate and acetaldehyde used for kinetics studies of asHPAL.

Substrate	Concentration (mM)	
	2-Ketobutyrate	Acetaldehyde
2-ketobutyrate	100	100
	50	100
	33	100
	25	100
	20	100
acetaldehyde	100	100
	100	50
	100	33
	100	25
	100	20

Table 3-3 Data collection and refinement statistics of asHPAL-2-ketobutyrate complex.

<i>Data collection</i>	
X-ray source	SPring-8 BL26B2
Wavelength (Å)	1.00000
Space group	C2
Unit cell dimensions (Å)	$a = 116.2, b = 88.1, c = 85.1$
(°)	$\beta = 122.3$
Resolution (Å)	20.00–1.58 (1.60–1.58) ^a
Observed reflections	355489
Unique reflections	96467
Completeness (%)	98.5 (96.8) ^a
R_{meas} (%) ^b	4.3 (14.8) ^a
$I/\sigma(I)$	26.84 (5.84) ^a
<i>Refinement</i>	
Resolution (Å)	20.0–1.58
$R_{\text{work}} / R_{\text{free}}$ (%) ^c	18.2 / 20.0
RMSD bond length (Å)	0.006
RMSD bond angle (°)	1.079
Ramachandran plot (%)	
Favored	95.0
Additionally allowed	5.0
Generously allowed	0
disallowed	0

^a Values in parentheses are for highest-resolution shell.

^b $R_{\text{meas}} = \sum_{hkl} [(\sum_i |I_i - \langle I \rangle|) / \sum_i |I_i|]$.

^c $R_{\text{work}} = (\sum_{hkl} ||F_o| - |F_c||) / \sum_{hkl} |F_o|$. R_{work} was calculated with 95% of the data used for refinement, and R_{free} was calculated with 5% of the data excluded from refinement.

Table 3-4 Data collection and refinement statistics of asHPAL at pH 6.0.

<i>Data collection</i>	
X-ray source	FR-E SuperBright
Wavelength (Å)	1.00000
Spacegroup	<i>P1</i>
Unit cell dimensions (Å)	$a = 125.3, b = 125.3, c = 129.9$
(°)	$\alpha = 95.3, \beta = 122.3, \gamma = 93.3$
Resolution (Å)	20.0–2.15 (2.20–2.15) ^a
Observed reflections	792458
Unique reflections	423517
Completeness (%)	97.0 (96.1) ^a
R_{meas} (%) ^b	5.2 (23.3) ^a
$I/\sigma(I)$	18.63 (4.36) ^a
 <i>Refinement</i>	
Resolution range (Å)	20.0–2.15
$R_{\text{work}} / R_{\text{free}}$ (%) ^c	19.5 / 23.3
RMSD bond length (Å)	0.013
RMSD bond angle (°)	1.156
Ramachandran plot (%)	
Favored	93.8
Additionally allowed	6.9
Generously allowed	0
disallowed	0

^a Values in parentheses are for the highest-resolution shell.

^b $R_{\text{meas}} = \sum_{hkl} [(\sum_i |I_i - \langle I \rangle|) / \sum_i |I_i|]$.

^c $R_{\text{work}} = (\sum_{hkl} ||F_o| - |F_c||) / \sum_{hkl} |F_o|$. R_{work} was calculated with 95% of the data used for refinement, and R_{free} was calculated with 5% of the data excluded from refinement.

Table 3-5 Kinetic parameters toward 2-ketobutyrate.

	K_m (mM)	k_{cat} (s^{-1})
Wild type	25.5 ± 2.5	213.2 ± 7.7
H52L	27.3 ± 1.5	11.7 ± 0.2
R77L	29.0 ± 0.3	43.1 ± 1.1
D91L	23.2 ± 3.7	113.2 ± 6.3

Table 3-6 Kinetic parameters toward acetaldehyde.

	K_m (mM)	k_{cat} (s^{-1})
Wild-type	24.1 ± 4.3	230.6 ± 14.3
R77L	310.3 ± 17.2	15.7 ± 0.5

Table 3-7 Kinetic parameters of N219Y/F26N mutant toward 2-ketobutyrate and acetaldehyde.

	K_m (mM)	k_{cat} (s ⁻¹)
2-Ketobutyrate	24.1 ± 2.7	196.8 ± 8.5
Acetaldehyde	16.7 ± 0.3	203.1 ± 3.2

Table 3-8 Relative production of the 4HIL stereoisomers in asHPAL/BCAT bienzymatic reaction dependent on the reaction pH

aldolase	pH	4-HIL production (mM)		
		(2S,3R,4S)-4-HIL	(2S,3R,4S)-4-HIL	ρ^1
Wild	pH 6	7.1 ± 0.3	1.1 ± 0.2	6.5
	pH 7	8.7 ± 0.6	2.3 ± 0.3	3.8
	pH 8	6.1 ± 0.5	2.5 ± 0.1	2.4
F26W	pH 6	5.2 ± 0.3	5.3 ± 0.2	1.0
	pH 7	6.7 ± 0.5	5.2 ± 0.3	1.3
	pH 8	6.1 ± 0.3	3.1 ± 0.1	2.0
F26L	pH 6	5.3 ± 0.5	5.1 ± 0.6	1.0
	pH 7	7.5 ± 0.6	7.3 ± 0.5	1.0
	pH 8	5.7 ± 0.3	5.3 ± 0.3	1.1
F26Y	pH 6	6.9 ± 0.3	1.2 ± 0.2	5.8
	pH 7	7.9 ± 0.6	2.5 ± 0.3	3.2
	pH 8	6.3 ± 0.5	2.7 ± 0.1	2.3
N219Y/F26N	pH 6	5.1 ± 0.5	0.5 ± 0.1	10.2
	pH 7	6.3 ± 0.7	1.3 ± 0.3	4.8
	pH 8	6.4 ± 0.9	2.1 ± 0.3	3.0

¹The relative production of 4HIL isomers was calculated as [2S, 3R, 4S]/[2S, 3R, 4R].

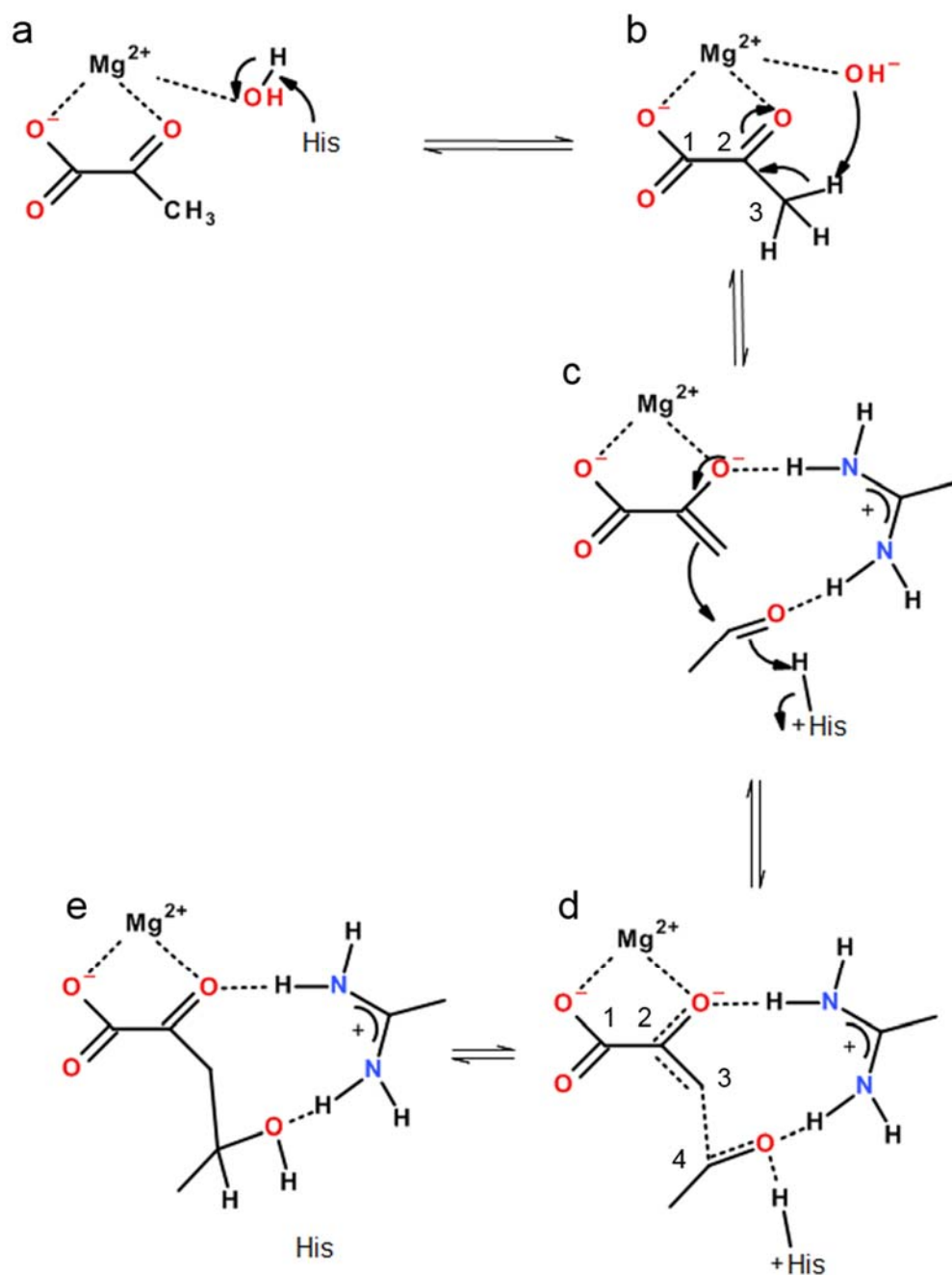


Fig. 3-1 Proposed catalytic mechanism of the HpaI/HpcH-aldolase subfamily based on the structure of HpcH.

(a) The Mg^{2+} -bound water is activated to hydroxide ion by His. (b) The hydroxide ion abstracts a proton from the C3 atom of pyruvate to generate the nucleophilic enolate. (c) The nucleophilic enolate attacks the electrophilic carbon of the acetaldehyde acceptor. (d) The C4 oxygen is protonated by His to form the hydroxyl group. (e) The enzyme adopts a ground state, and catalytic cycle is completed by producing HMKP.

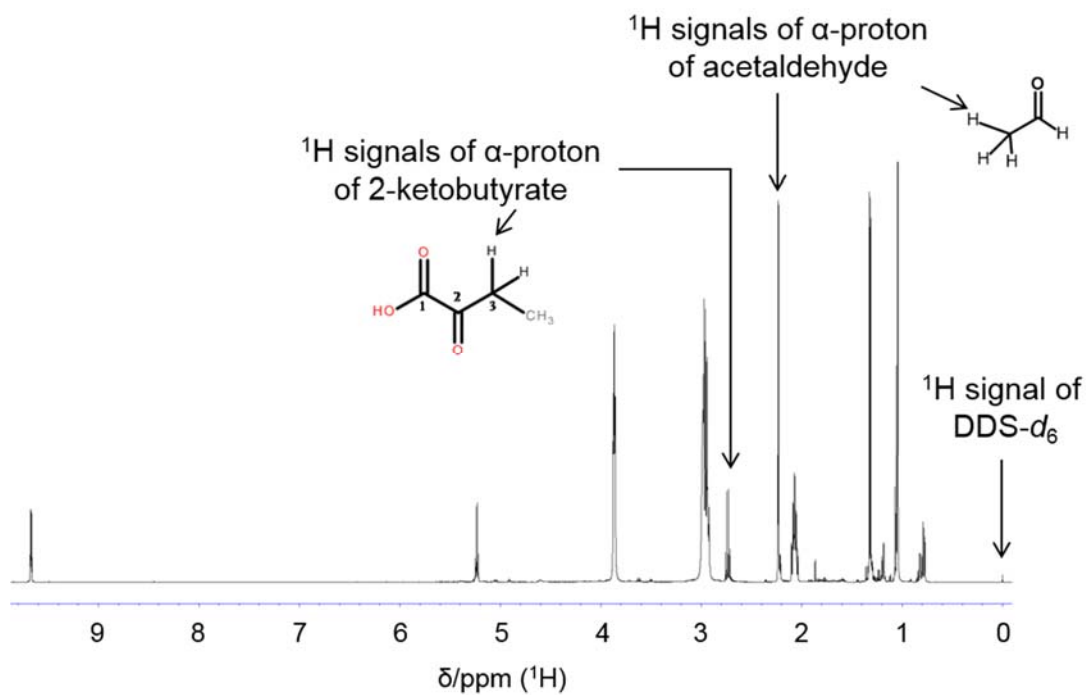


Fig. 3-2 ^1H NMR spectrum of asHPAL reaction solution.

^1H NMR signals shown by the arrows were used for quantification.

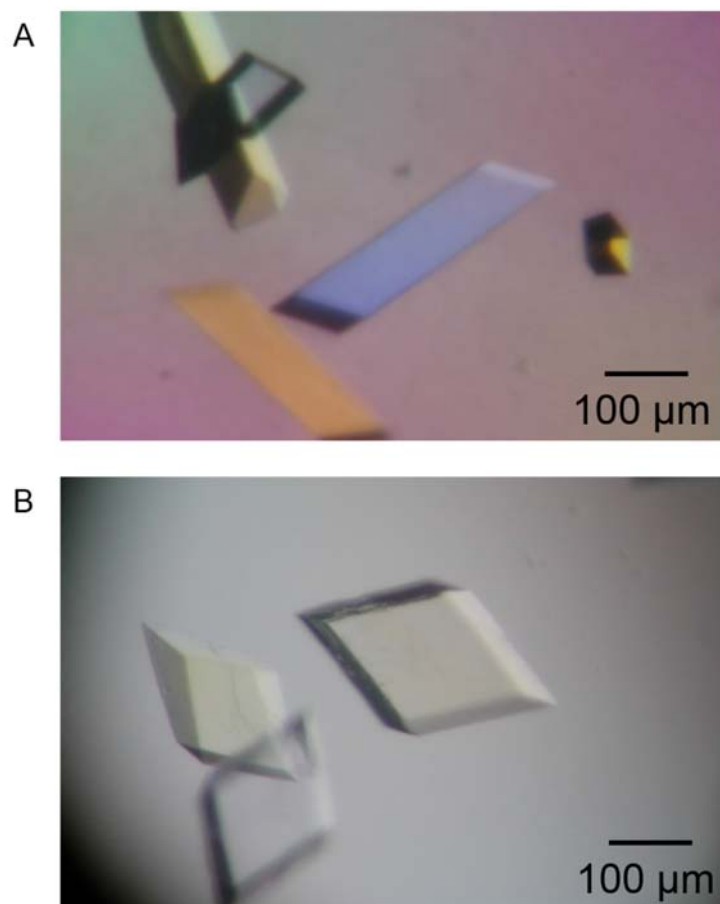


Fig. 3-3 asHPAL crystals in the presence of 2-ketobutyrate or at pH 6.0.

(A) Crystals of asHPAL obtained as co-crystals with 2-ketobutyrate. The crystal was grown in the reservoir solution containing 100 mM HEPES-Na (pH 7.7), 30% (v/v) PEG 400, 200 mM MgCl₂, and 200 mM 2-ketobutyrate at 293 K for 1 day.

(B) Crystals of asHPAL at pH 6.0. The crystal was grown in the reservoir solution containing 100 mM BIS-TRIS (pH 6.0), 1.5 M (NH₄)₂SO₄, and 100 mM NaCl at 293 K for 2 days.

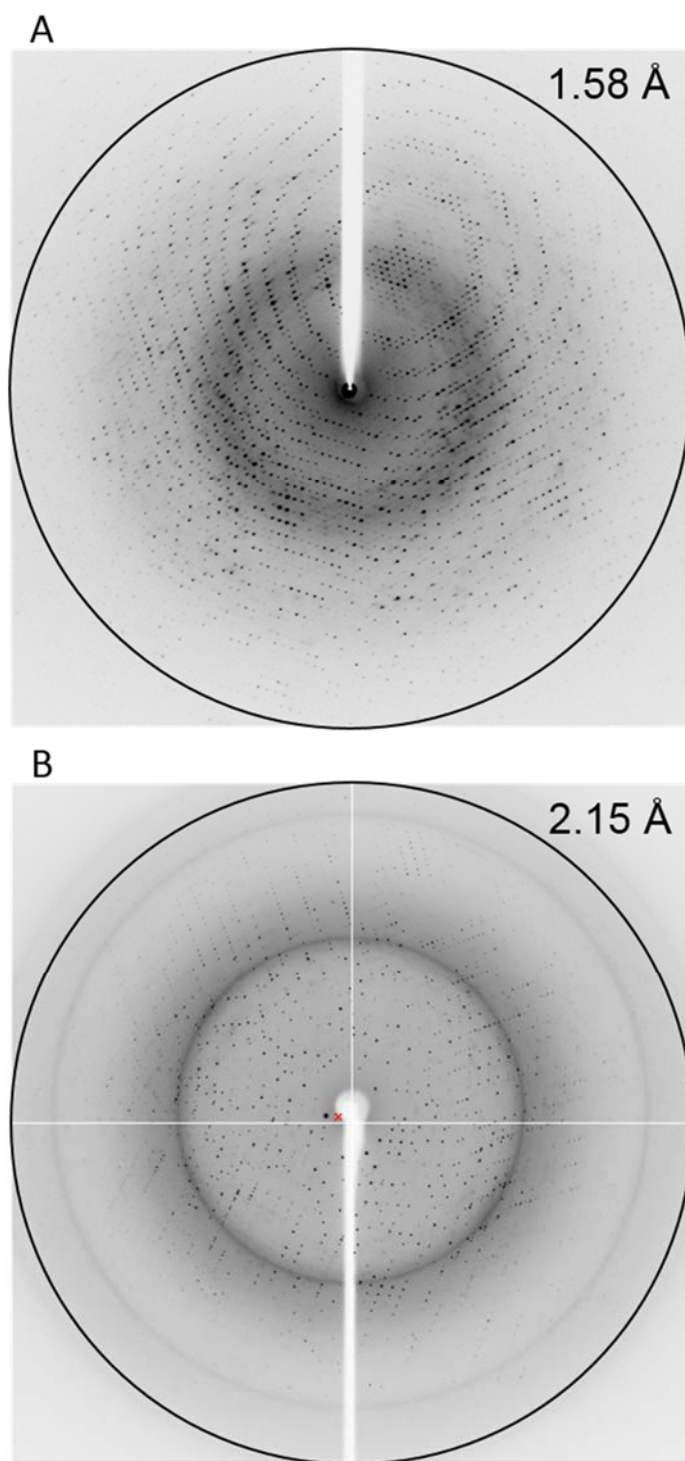


Fig. 3-4 X-ray diffraction images obtained from the asHPAL crystals obtained in the presence of 2-ketobutyrate (A) and at pH 6.0 (B).

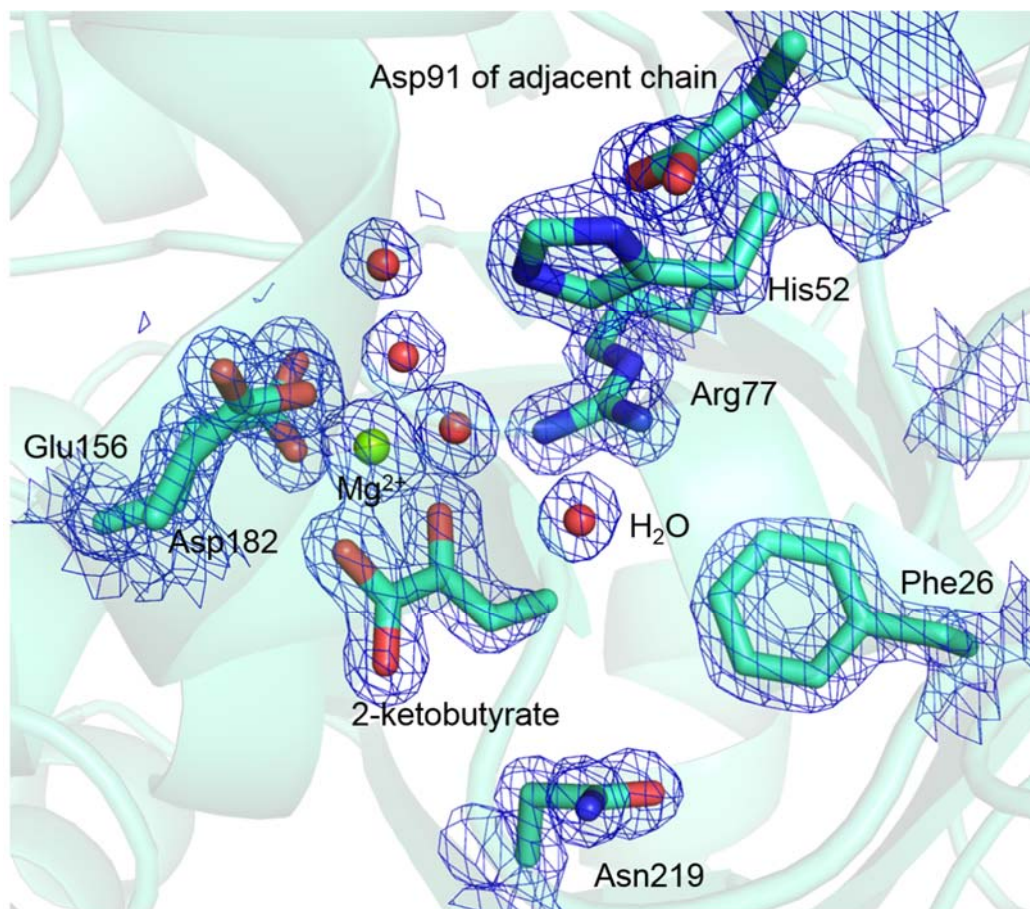


Fig. 3-5 Structure of the active site of asHPAL-2-ketobutyrate complex.

Clear electron density was observed for 2-ketobutyrate molecule, Mg^{2+} , 4 water molecules, and residues near the active site. Blue mesh showed the $2|F_o|-|F_c|$ omit map (1.5σ).

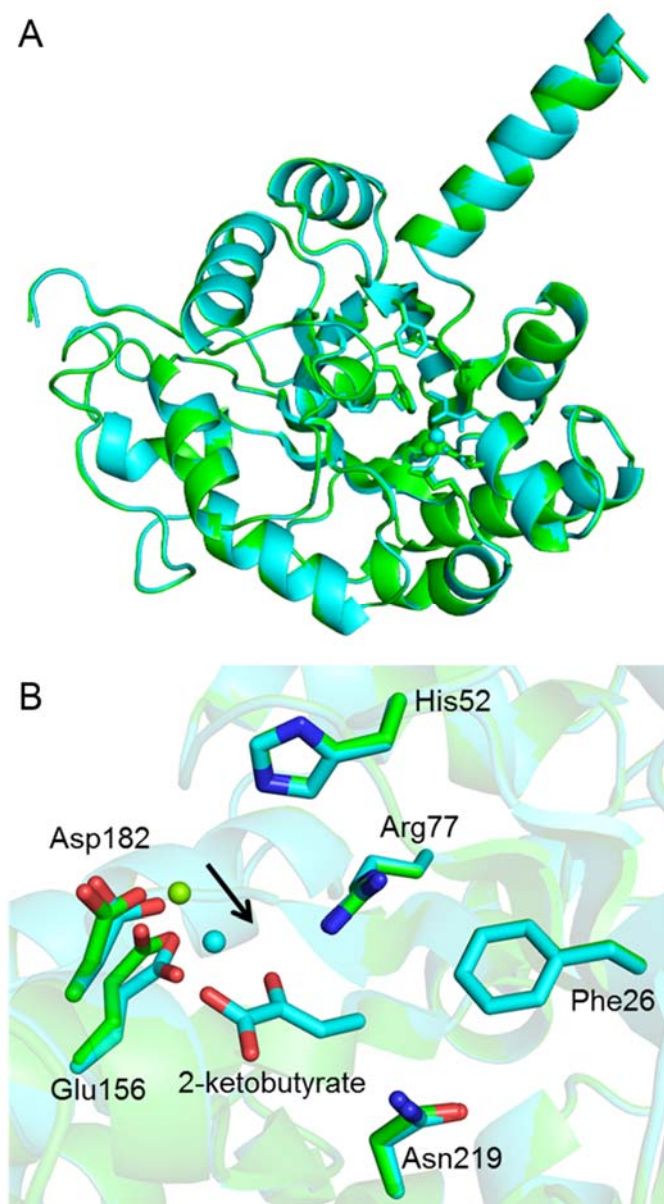


Fig. 3-6 Comparison between the structures of asHPAL and its complex with 2-ketobutyrate.

(A) The structural alignment of asHPAL (green) and asHPAL-2-ketobutyrate complex (cyan). There is no significant change in the overall structures of asHPAL and asHPAL-2-ketobutyrate complex (C_{α} RMSD of 0.076 Å).

(B) The structural alignment of active site of asHPAL (green) and asHPAL-2-ketobutyrate complex (cyan). Mg^{2+} and the side chain of Glu156 and Asp182 moves toward 2-ketobutyrate because the complex formation also required the interaction between 2-ketobutyrate and Arg77. Mg^{2+} ions are represented by spheres.

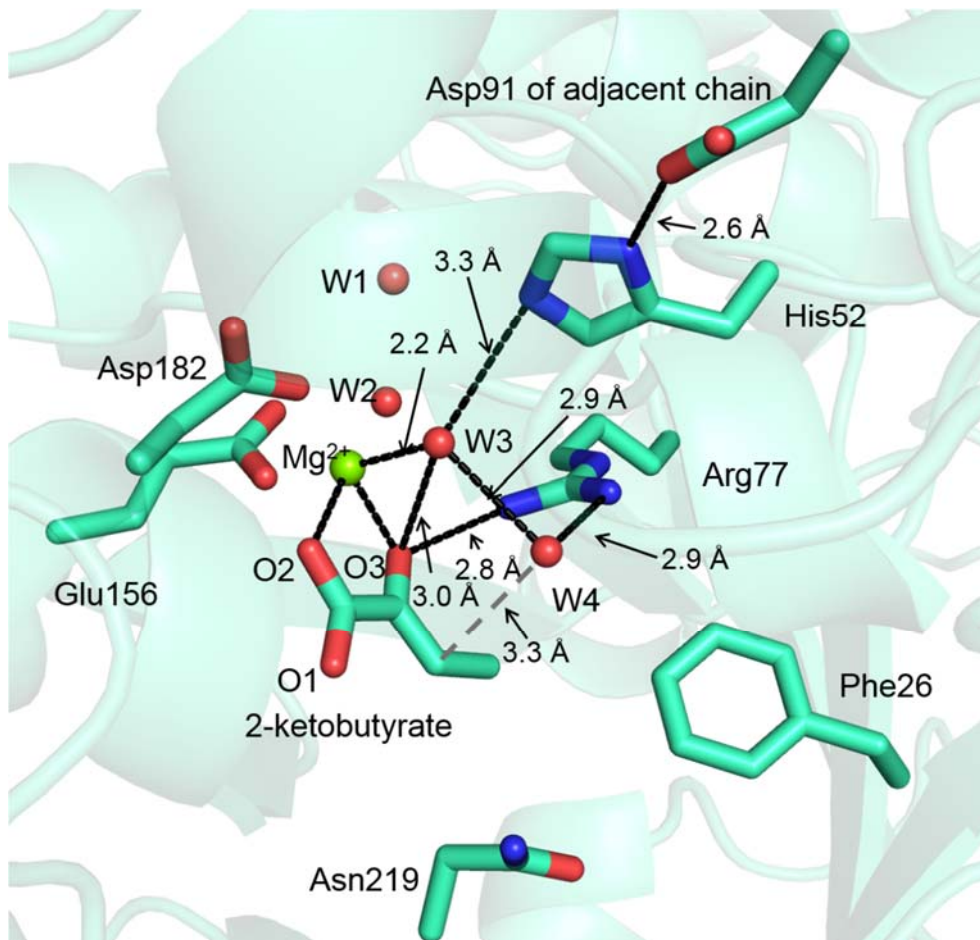


Fig. 3-7 Active site of the asHPAL-2-ketobutyrate complex.

Mg^{2+} ion (green) and water molecules (red) are represented with sphere models. Hydrogen bonds are represented by black dashed lines.

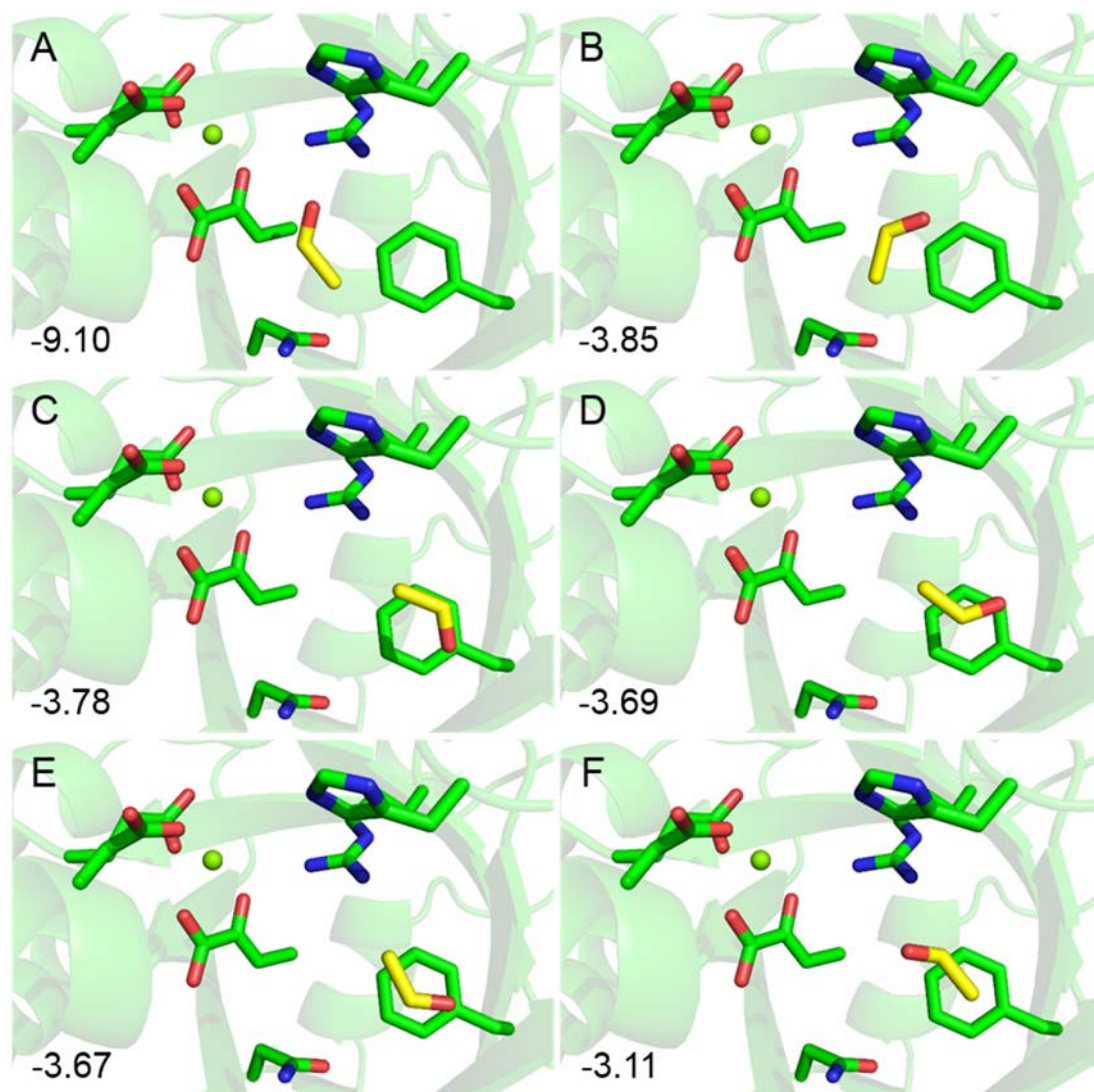


Fig. 3-8 Top 6 of the stable binding models of acetaldehyde.

(A) Model 1; (B) Model 2; (C) Model 3, (D) Model 4; (E) Model 5; and (F) Model 6. The values show U_{dock} scores (kcal mol⁻¹), which are calculated by U_{ele} (electric energy)+ U_{vdw} (van der Waals energy)+ U_{solv} (Solvation energy)+ U_{strain} (Strain energy)]. Mg^{2+} ions and acetaldehydes are represented by spheres and yellow sticks, respectively.

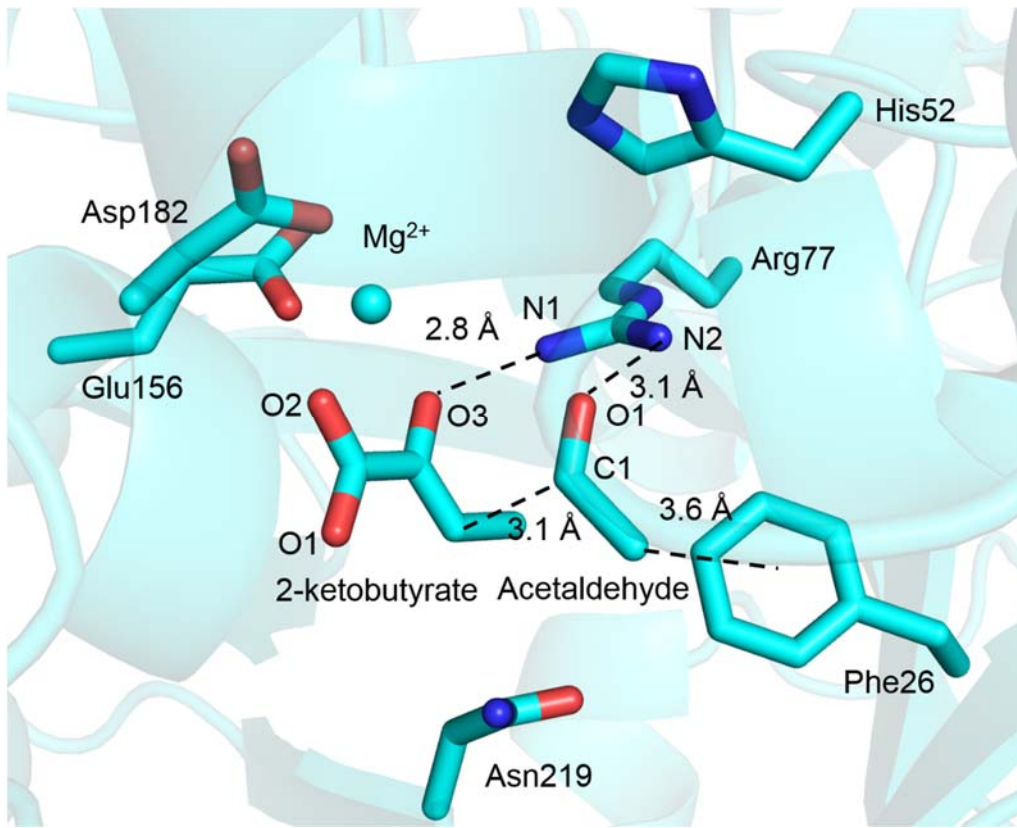


Fig. 3-9 Probable binding mode of acetaldehyde at the active site of asHPAL.

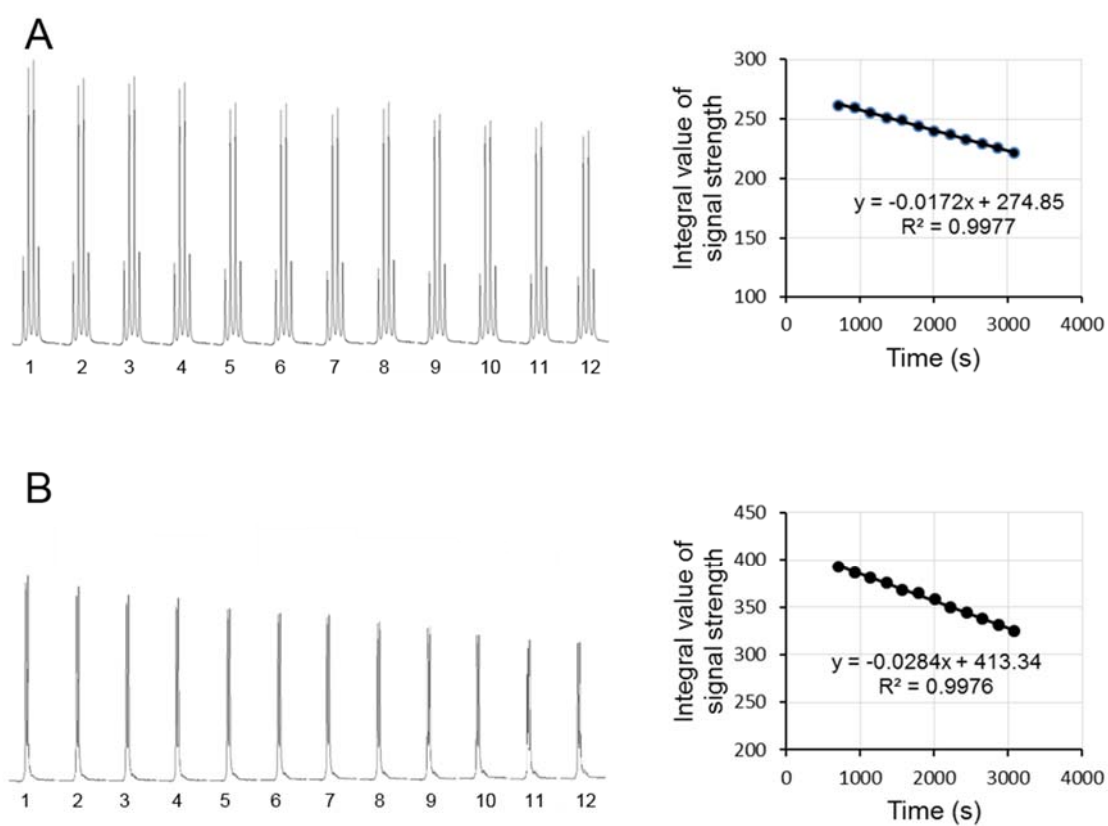


Fig. 3-10 Time-dependent signal changes of 2-ketobutyrate (A) and acetaldehyde (B). Concentrations of 2-ketobutyrate and acetaldehyde were linearly decreased under the optimized reaction conditions.

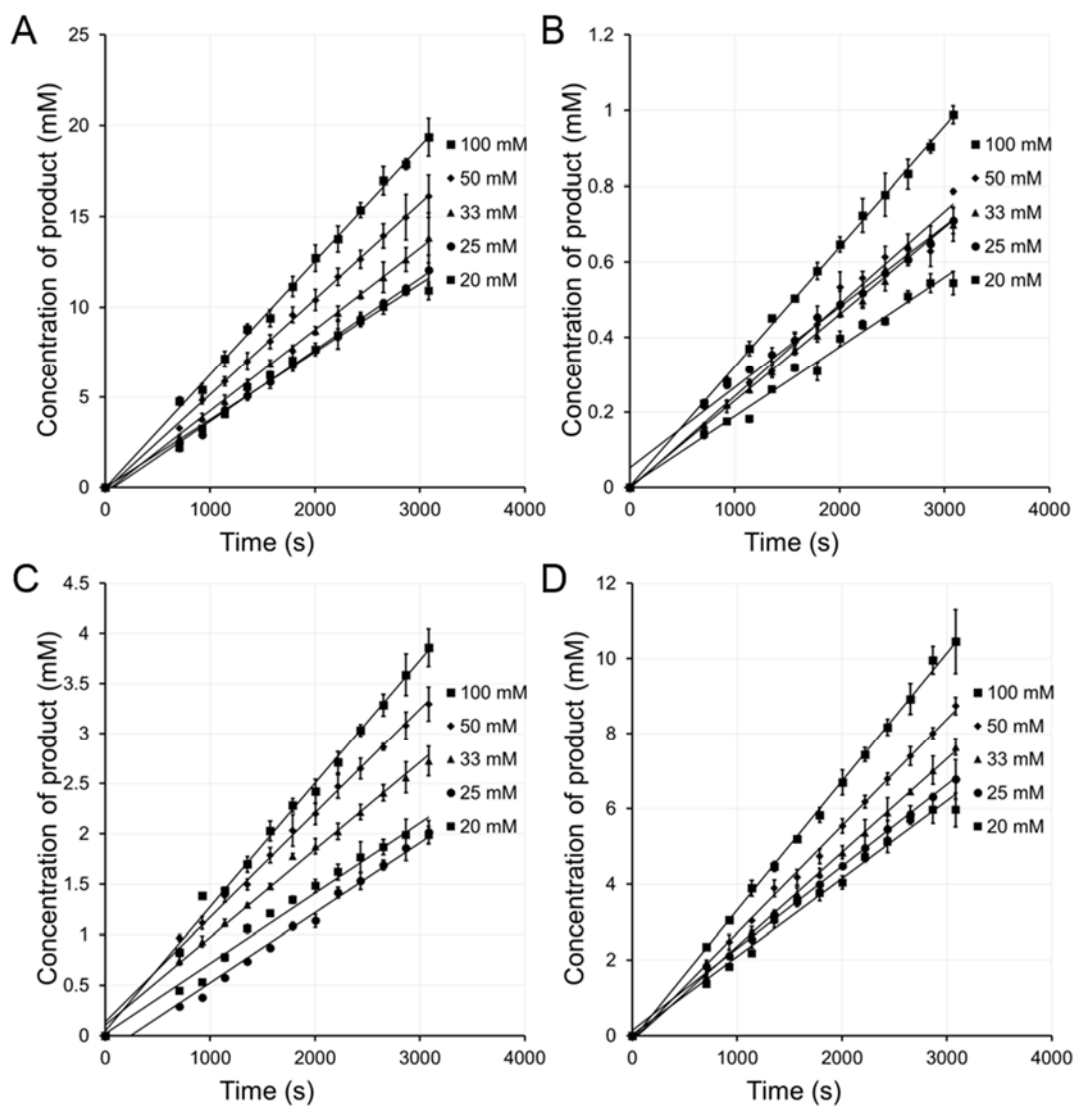


Fig. 3-11 Time-dependent HMKP production by asHPAL and its mutants.

(A) Wild type; (B) H52L mutant; (C) R77L mutant; and (D) D91L mutant.

The reduced 2-ketobutyrate concentrations are considered as the produced concentrations of HMKP. All determinations were performed in triplicate. Error bars show standard deviations.

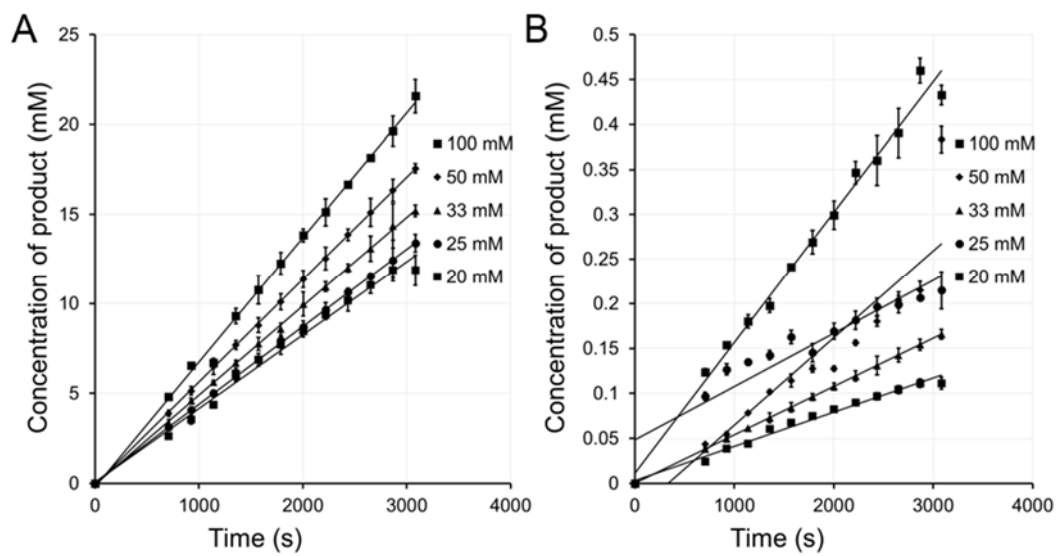


Fig. 3-12 Time-dependent HMKP production asHPAL and the R77L mutant.

(A) Wild type; and (B) R77L mutant.

The reduced acetaldehyde concentrations are considered as the produced concentrations of HMKP. All determinations were performed in triplicate. Error bars show standard deviations.

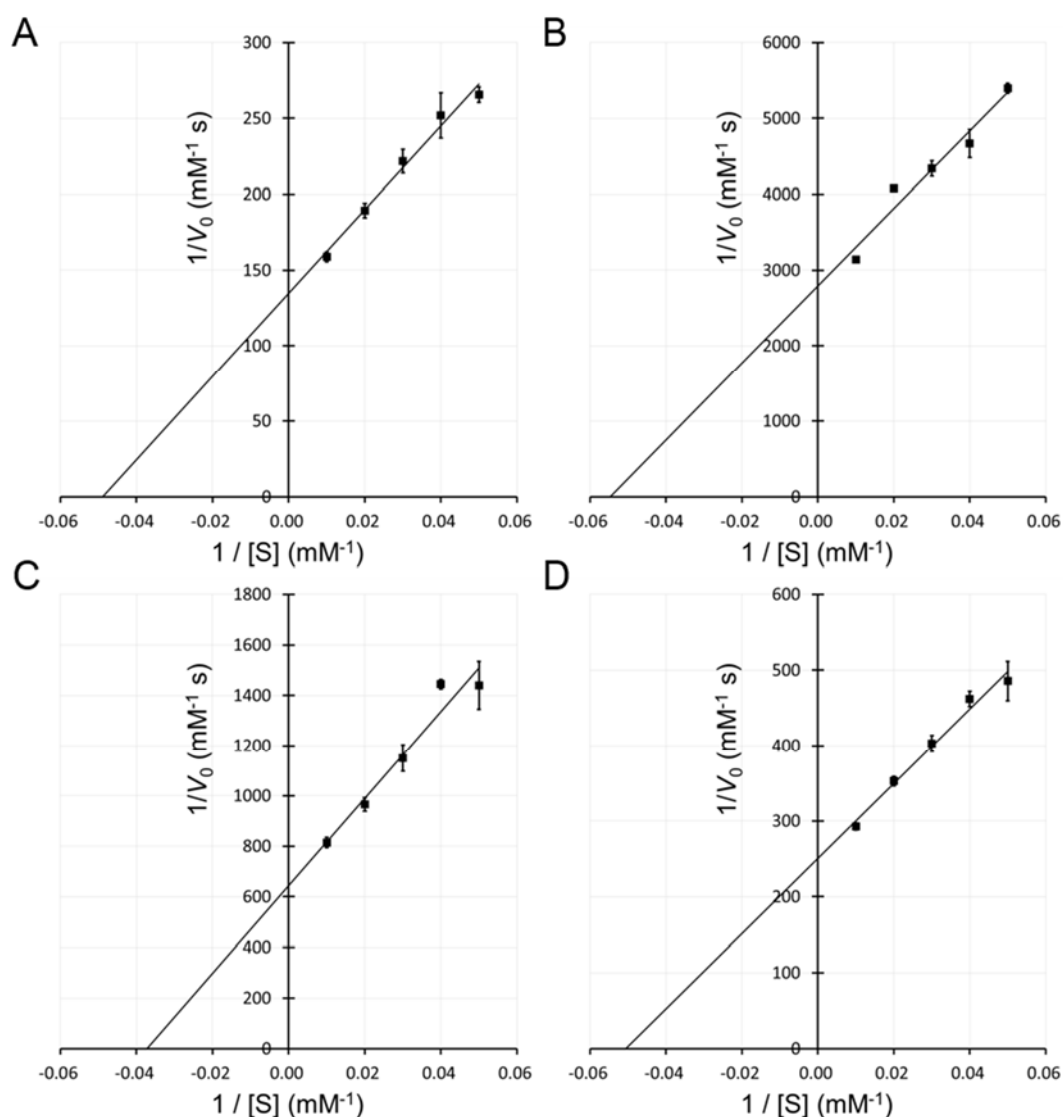


Fig. 3-13 Lineweaver–Burk plots for kinetic analysis of asHPAL and its mutants.

(A) Wild type; (B) H52L mutant; (C) R77L mutant; and (D) D91L mutant.

The reduced 2-ketobutyrate concentrations are considered as the produced concentrations of HMKP. All determinations were performed in triplicate. Error bars show standard deviations.

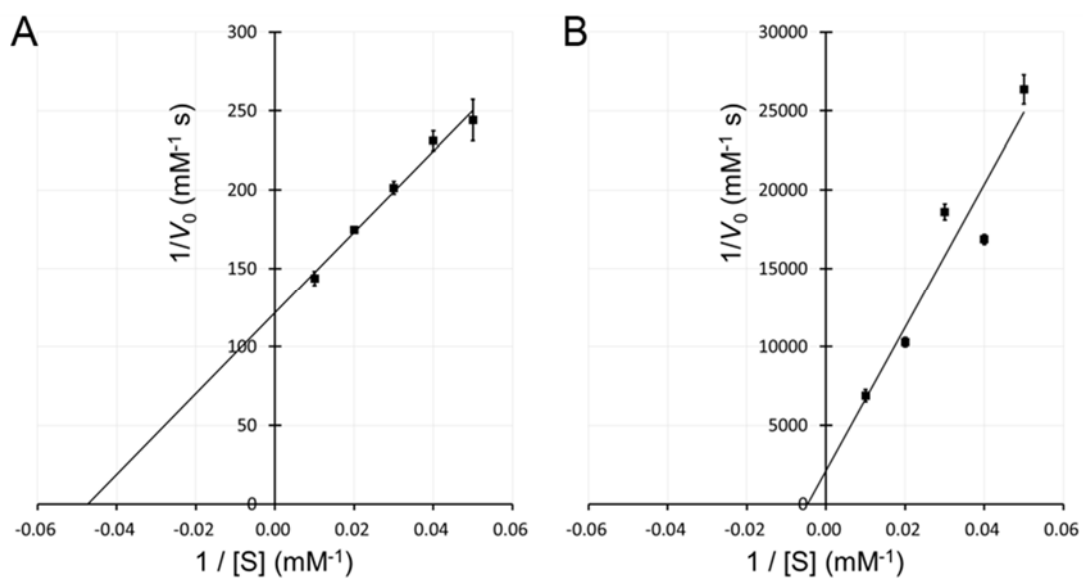


Fig. 3-14 Lineweaver–Burk plots for kinetic analysis of asHPAL and R77L mutant at varying concentrations of HMKP.

(A) Wild type; (B) R77L mutant.

The reduced 2-ketobutyrate concentrations are considered as the produced concentrations of HMKP. All determinations were performed in triplicate. Error bars show standard deviations.

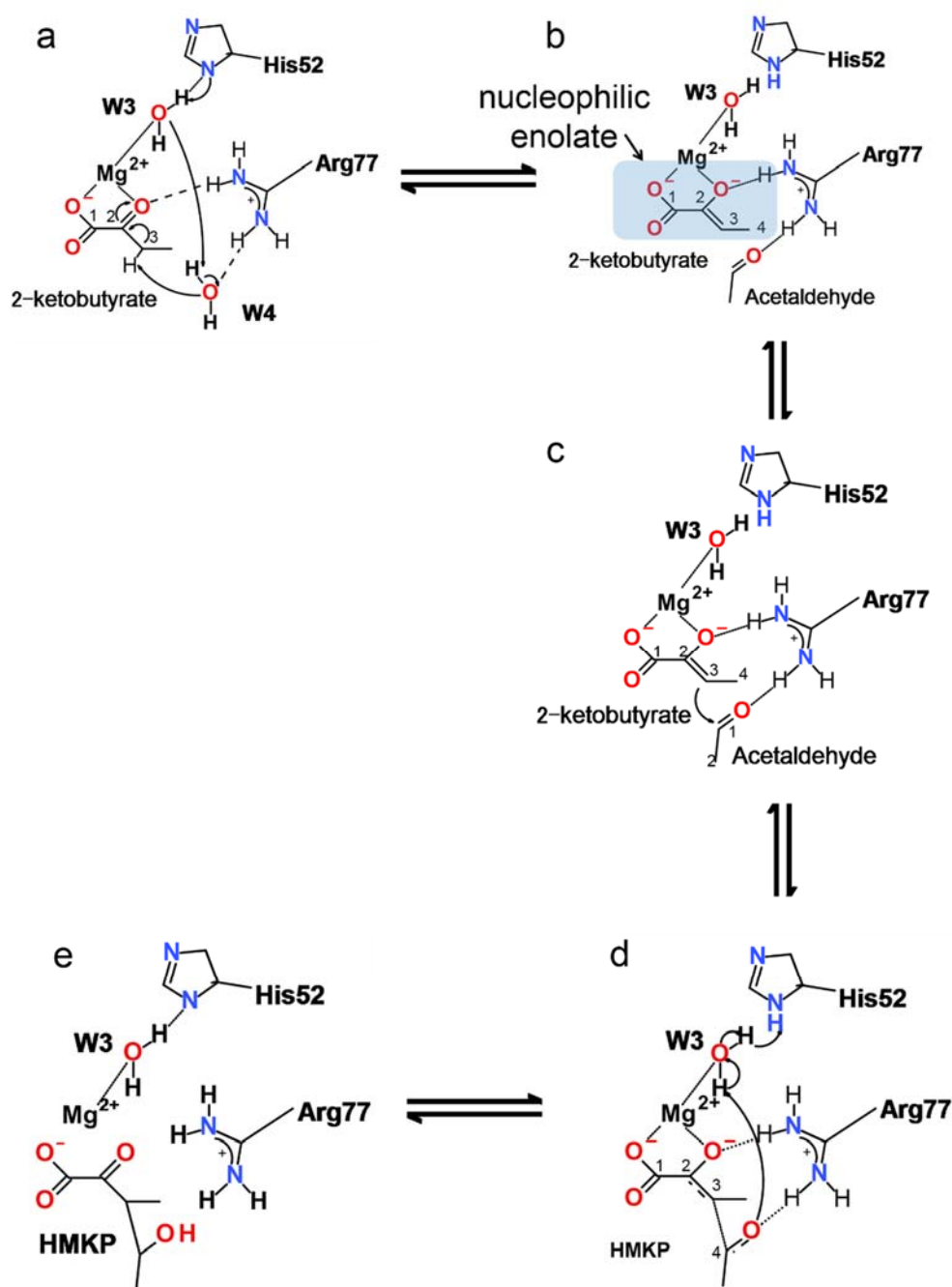


Fig. 3-15 Proposed catalytic mechanism of asHPAL.

(a) The proton (H^+) at the C3 atom of 2-ketobutyrate is abstracted by the His52-Asp91 catalytic dyad, through the water molecules W3 and W4, and then 2-ketobutyrate forms the nucleophilic enolate. (b) The W4 molecule is substituted by acetaldehyde. (c) Attack of the nucleophilic enolate on the electrophilic C1 atom of the acetaldehyde led to the formation of intermediate of HMKP. (d) The C4 oxygen of HMKP intermediate captures a proton from His52 through the water molecule W3 to form a hydroxyl group. (e) The enzyme is returned to its ground state, and the catalytic cycle is completed by producing HMKP.

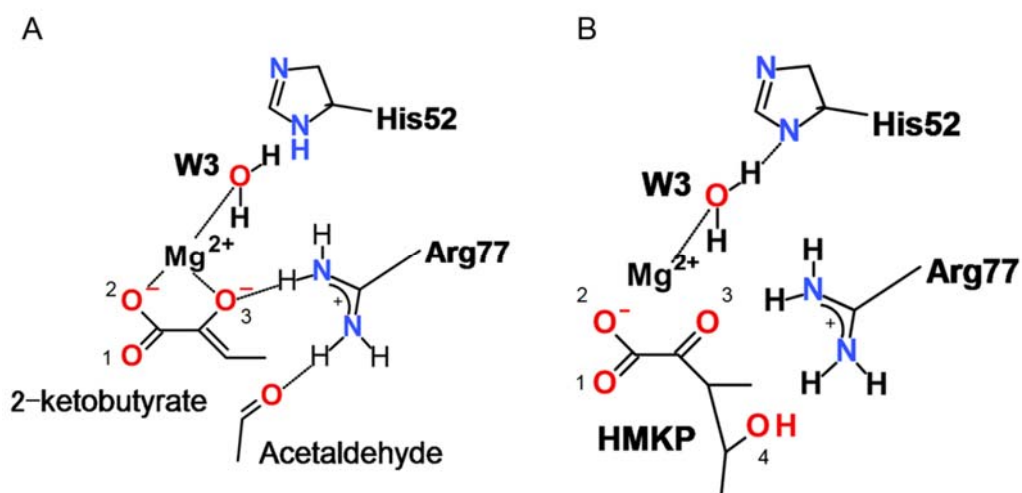


Fig. 3-16 Initial state (A) and end state (B) of the reaction catalyzed by asHPAL. The enolic hydroxyl group is suitable to coordinate Mg²⁺ due to its electronegativity. Therefore, 2-ketobutyrate with enolic hydroxyl group tends to bind to asHPAL at the beginning of the reaction. On the other hand, HMKP with hydroxyl group tends to be released from asHPAL at the end of the reaction.

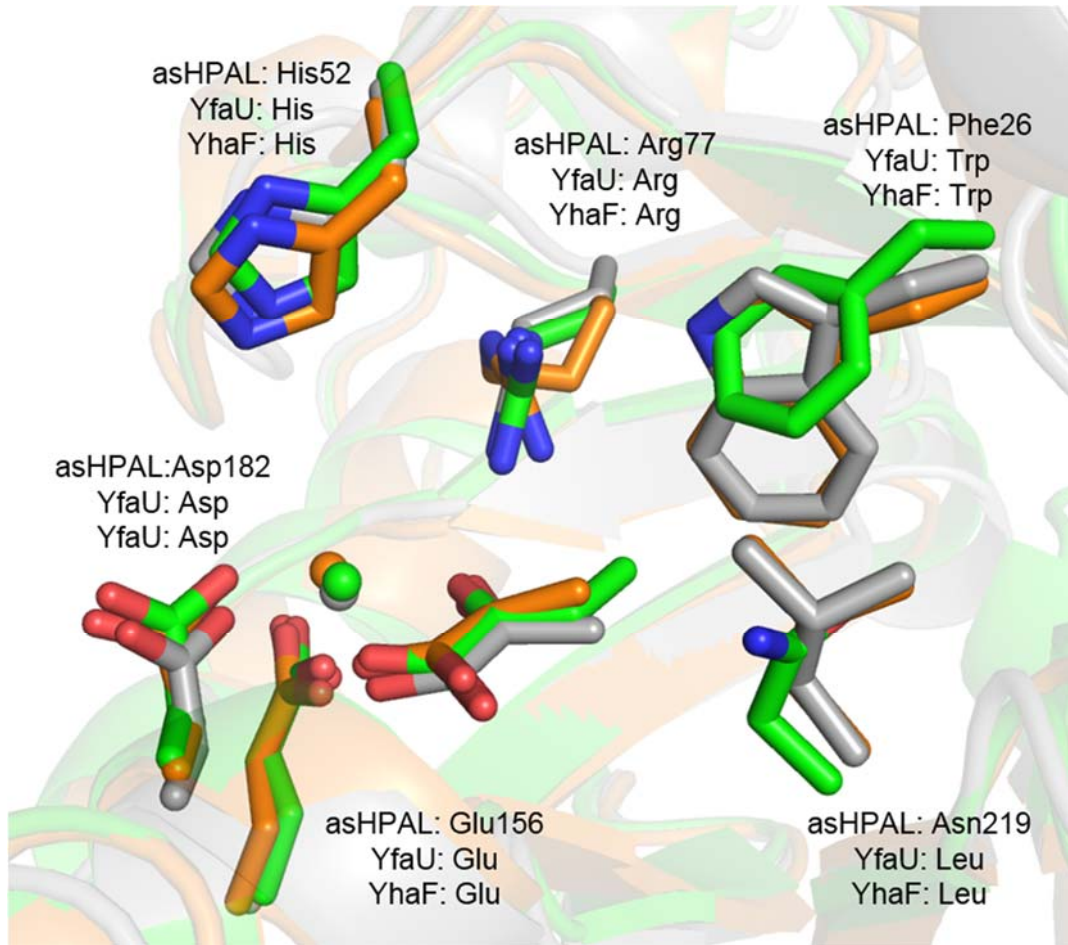


Fig. 3-17 The structural alignment of asHPAL-2-ketobutyrate (green), YfaU-pyruvate complex (yellow), and YhaF-pyruvate complex (gray).

These enzymes share four residues essential for the reaction. Two residues of asHPAL, Phe26 and Asn219, are different from the types of residues in the other enzymes.

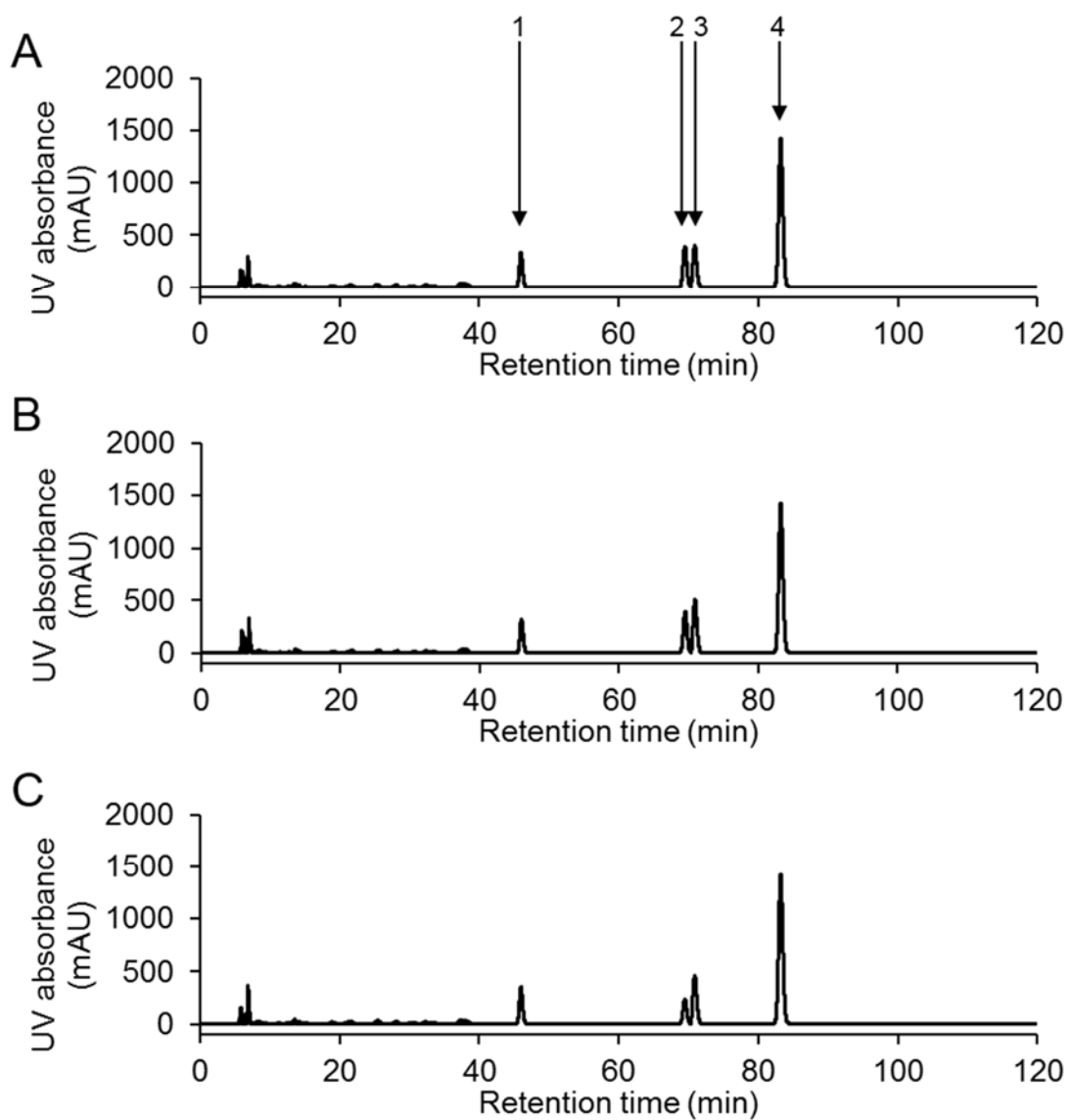


Fig. 3-18 HPLC analysis of reaction mixture catalyzed by asHPAL F26W mutant.
 Peak 1, L-Glu; peak 2, (2*S*,3*R*,4*R*)-4-HIL; peak 3, (2*S*,3*R*,4*S*)-4-HIL; and peak 4, α -aminobutyrate.

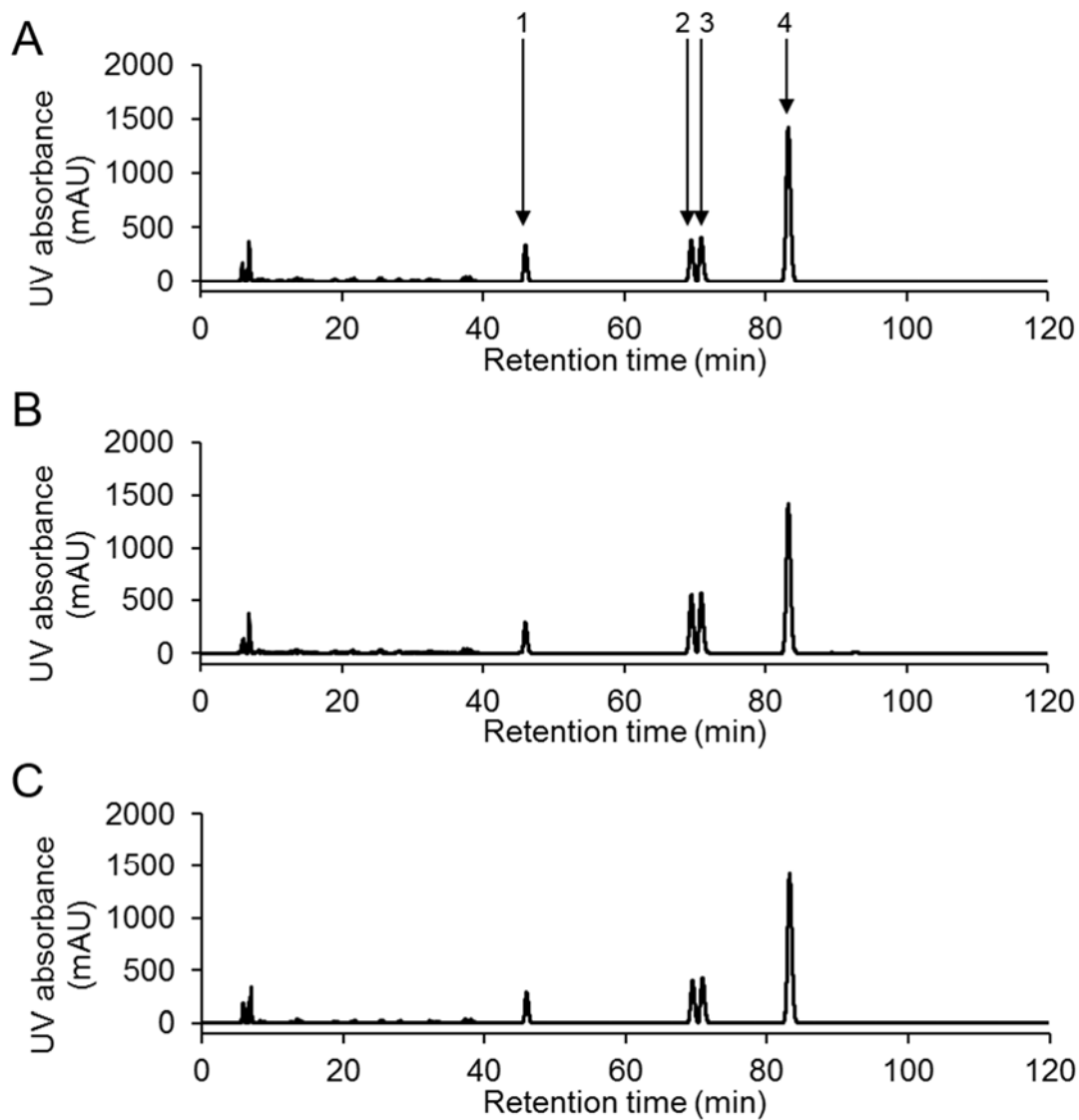


Fig. 3-19 HPLC analysis of reaction mixture catalyzed by F26L mutant.

Peak 1, L-Glu; peak 2, (2*S*,3*R*,4*R*)-4-HIL; peak 3, (2*S*,3*R*,4*S*)-4-HIL; and peak 4, α -aminobutyrate.

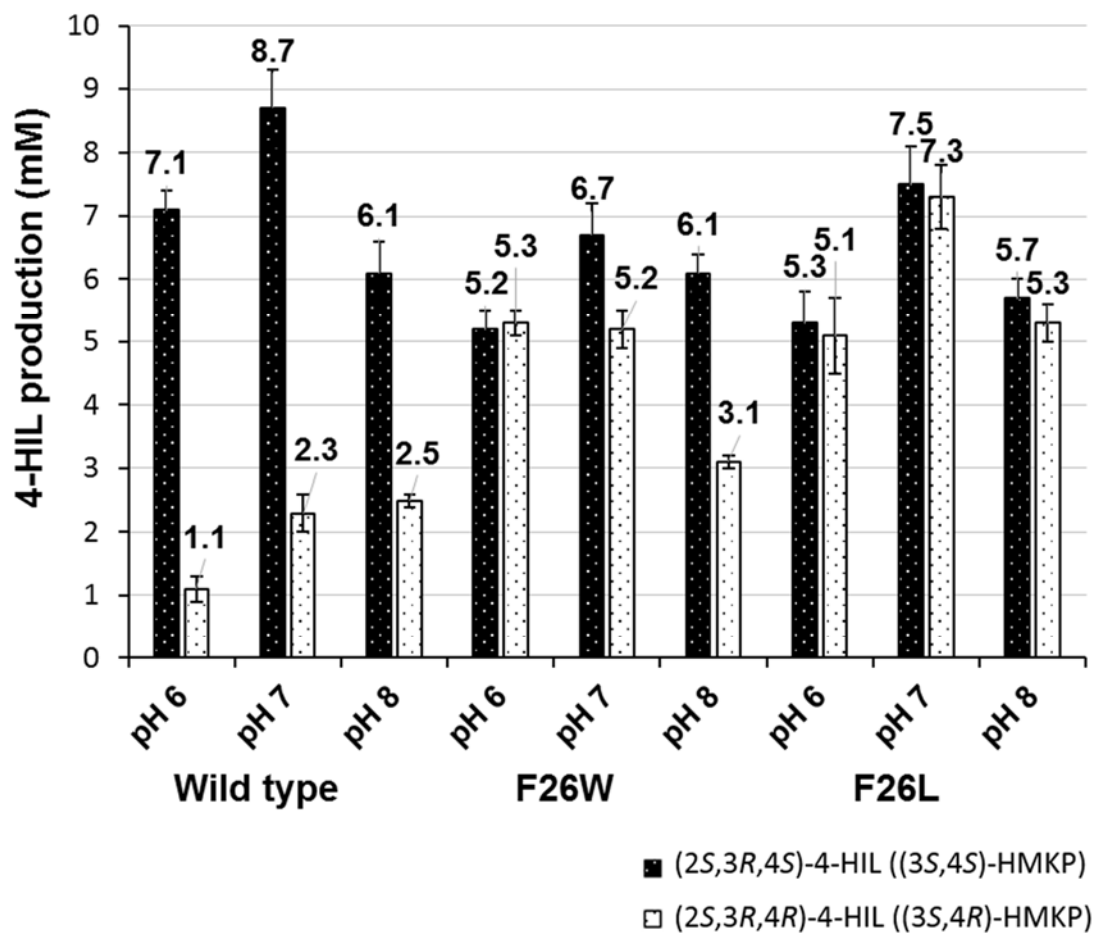


Fig. 3-20 pH dependency of 4-HIL enantiomers produced by the sequential reactions of asHPAL mutant (F26W or F26L) and BCAT.

All determinations were performed in triplicate. Error bars show standard deviations.

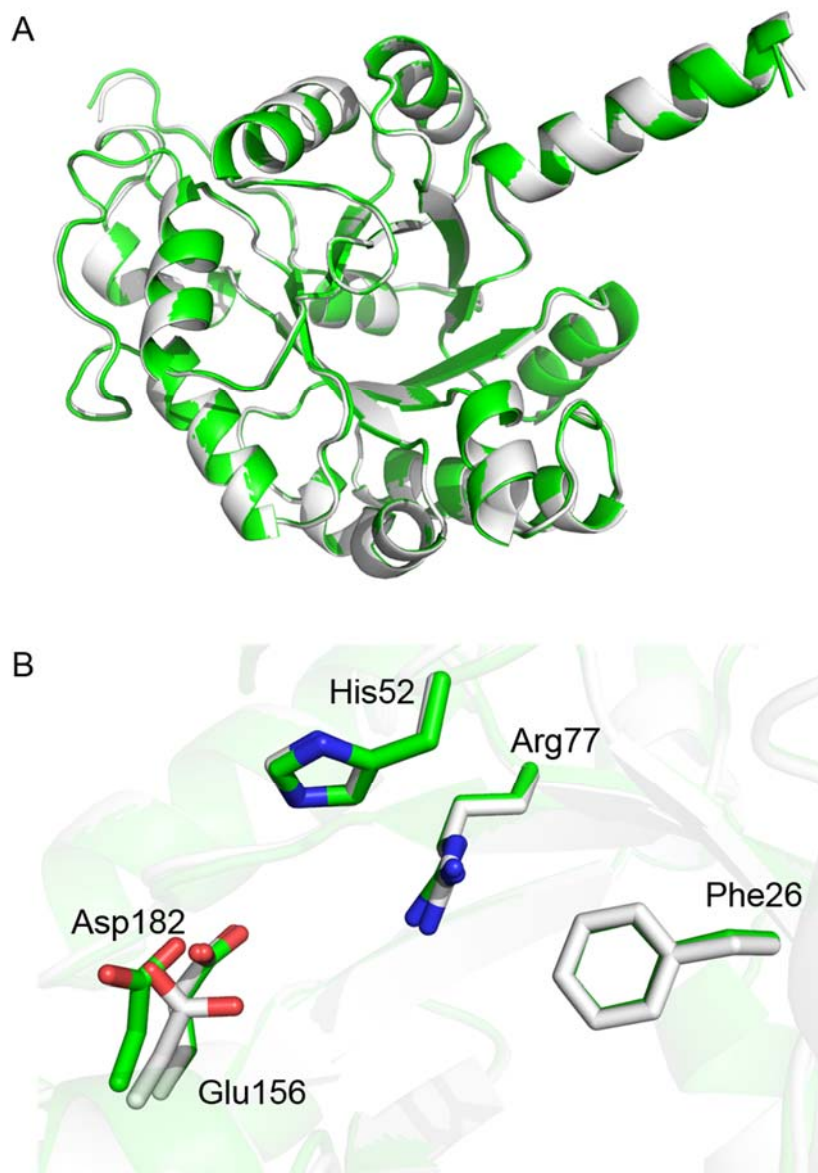


Fig. 3-21 Structural alignment of asHPAL at pH 6.0 (white) and pH 7.7 (green).
(A) The overall structures shows no significant difference (C_{α} RMSD of 0.273 Å).
(B) In the active site, the orientation of Asp182 changed in the structure at pH 6.0. The change is considered to be caused by the absence of Mg^{2+} .

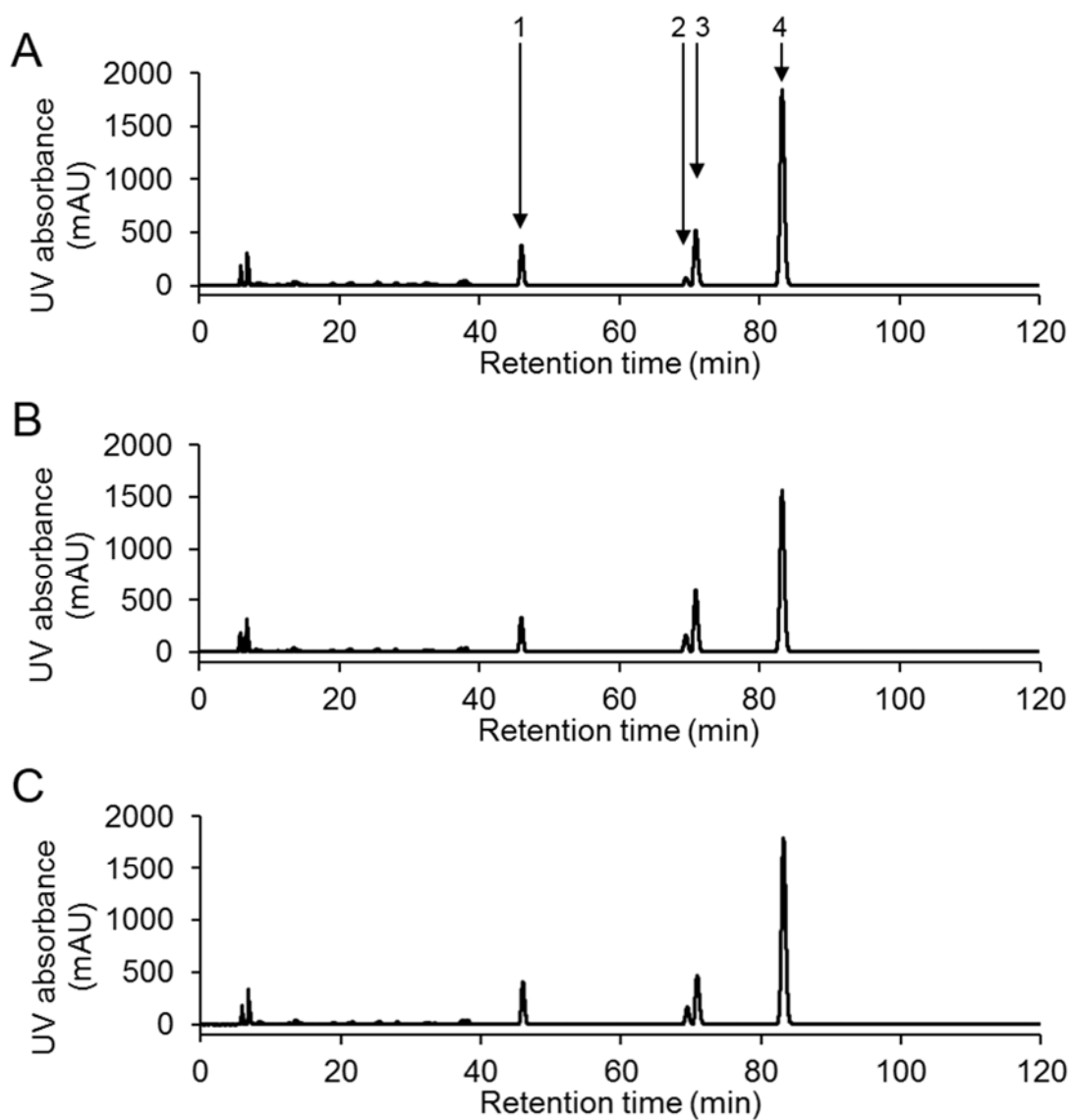


Fig. 3-22 HPLC analysis of reaction mixture catalyzed by F26Y mutant.

Peak 1, L-Glu; peak 2, (2*S*,3*R*,4*R*)-4-HIL; peak 3, (2*S*,3*R*,4*S*)-4-HIL; and peak 4, α -aminobutyrate.

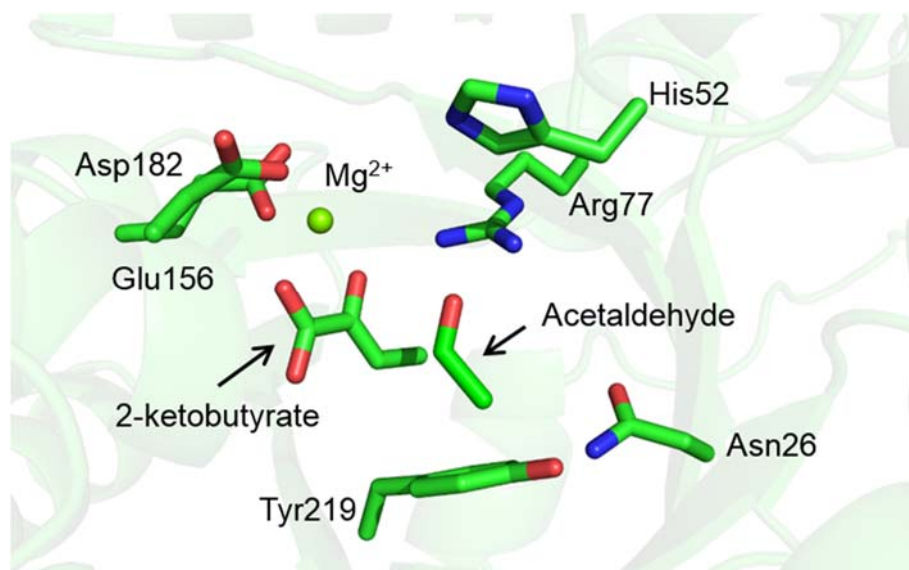


Fig. 3-23 The expected active site of N219Y/F26N mutant.

The side-chain amino group of Asn26 may interact with the hydroxyl group of Tyr219 through a hydrogen bond, which may allow the side-chain conformation of Tyr219 to form the π -CH interaction with the methyl group of acetaldehyde.

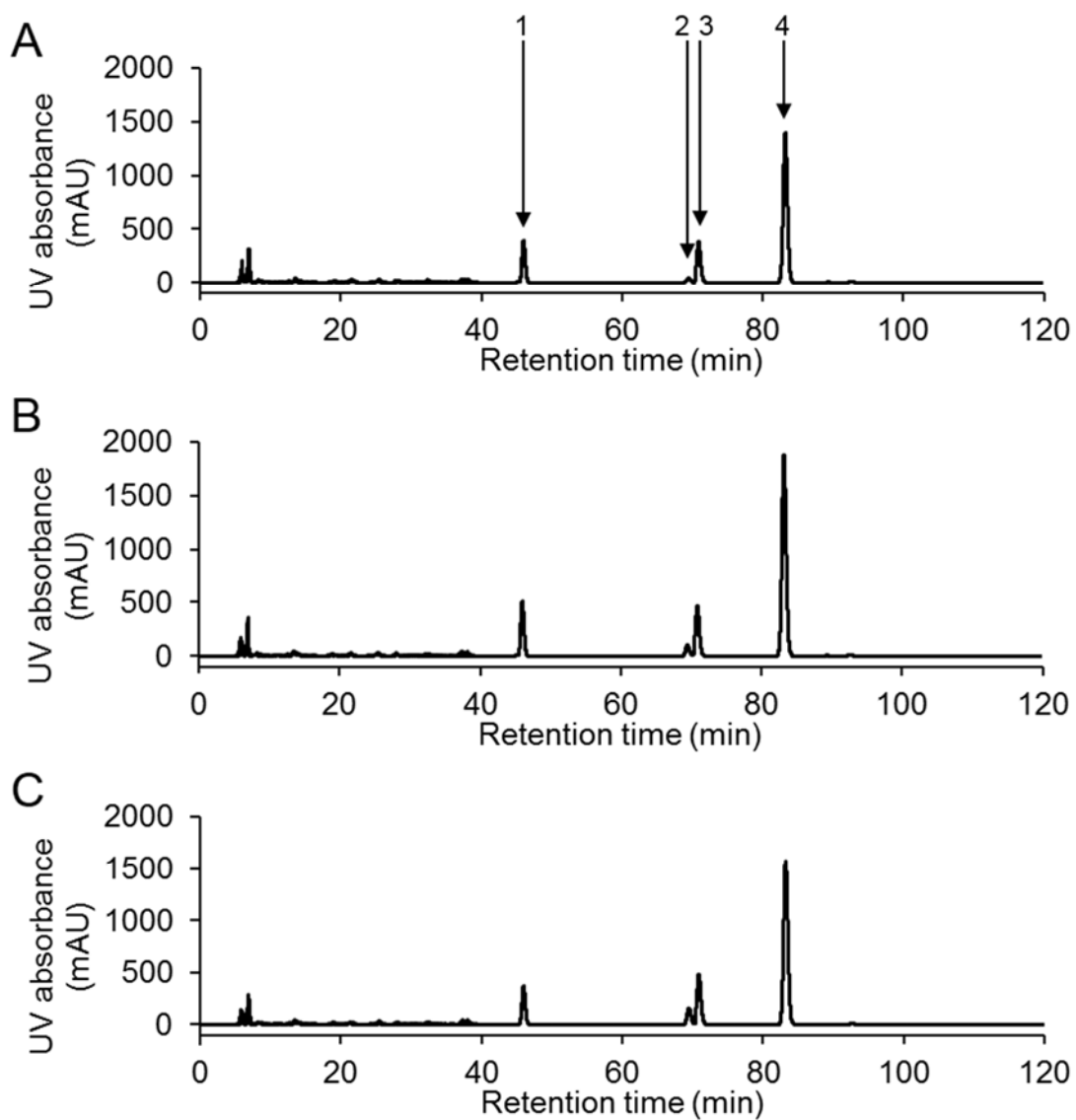


Fig. 3-24 HPLC analysis of reaction mixture catalyzed by N219Y/F26N mutant.

Peak 1, L-Glu; peak 2, (2*S*,3*R*,4*R*)-4-HIL; peak 3, (2*S*,3*R*,4*S*)-4-HIL; and peak 4, α -aminobutyrate.

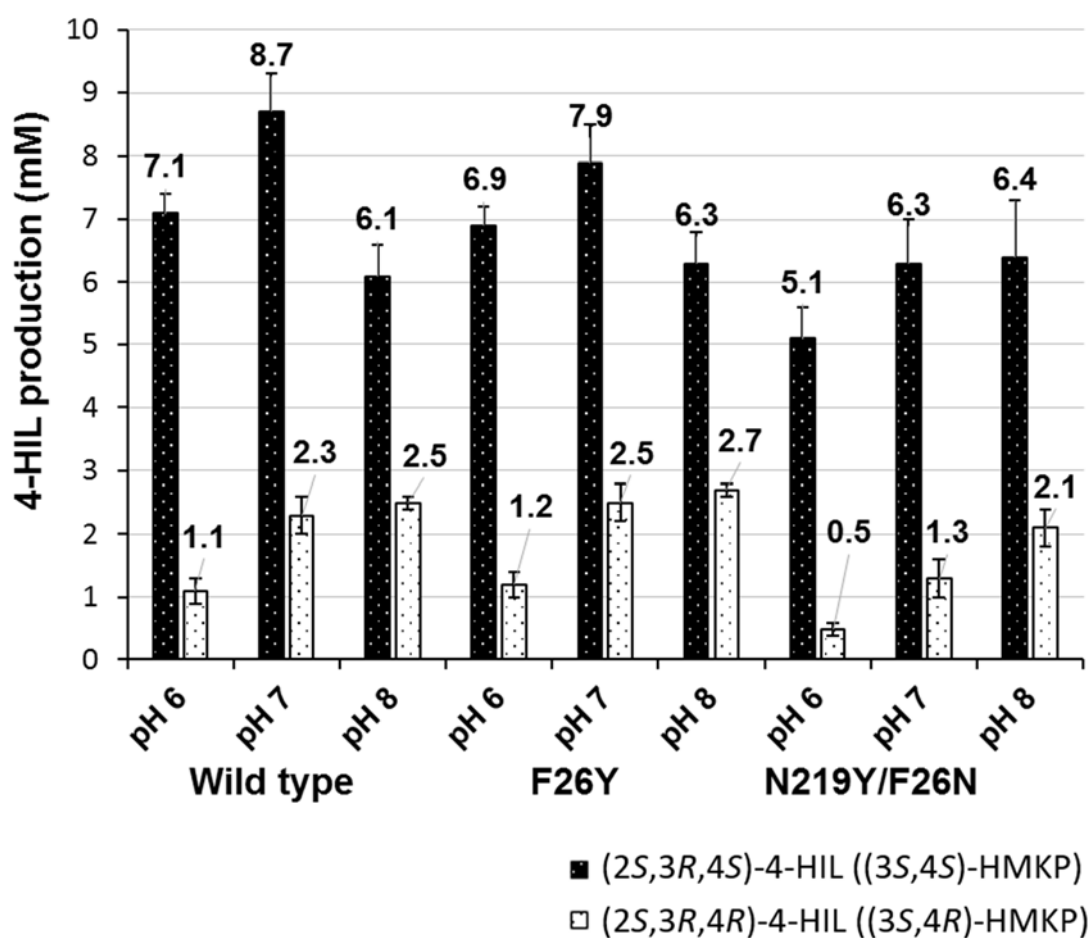


Fig. 3-25 pH dependency of 4-HIL enantiomers produced by the sequential reactions of asHPAL mutant (F26Y or N219Y/F26N) and BCAT. All determinations were performed in triplicate. Error bars show standard deviations.

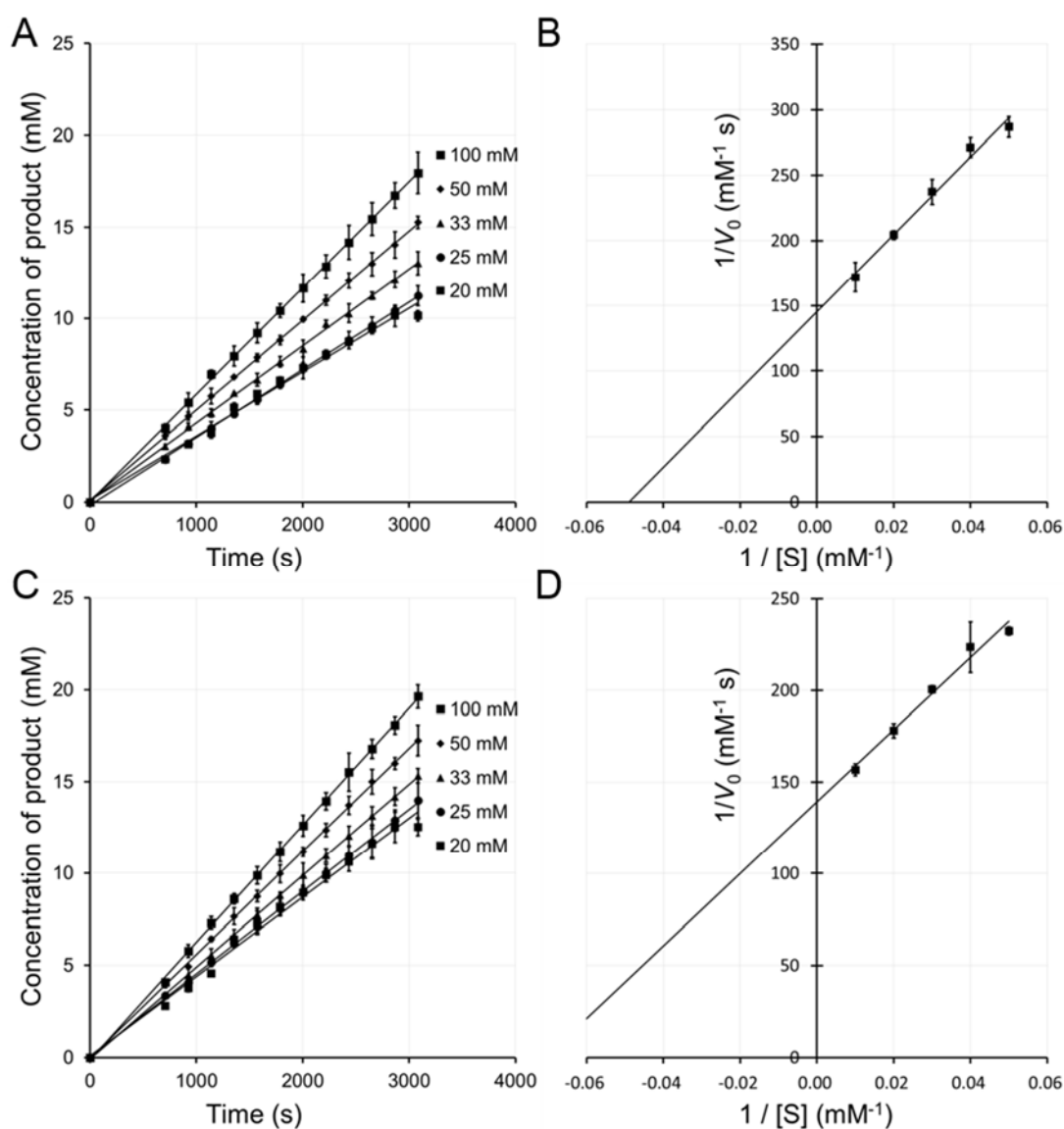


Fig. 3-26 Lineweaver–Burk plots for kinetic analysis of N219Y/F26N mutant.

(A) Time-dependent HMKP production by N219Y/F26N mutant towards 2-ketobutyrate.

(B) Lineweaver–Burk plots of N219Y/F26N mutant towards 2-ketobutyrate.

(C) Time-dependent HMKP production by N219Y/F26N mutant towards acetaldehyde.

(D) Lineweaver–Burk plots of N219Y/F26N mutant towards acetaldehyde.

The reduced 2-ketobutyrate or acetaldehyde concentrations are considered as the produced concentrations of HMKP, respectively. All determinations were performed in triplicate. Error bars show standard deviations.

Chapter 4

Mechanism of substrate specificity of asHPAL

4.1 Exordium

asHPAL has substrate specificity toward pyruvate and 2-ketobutyrate (Table 1-1). This narrow substrate specificity restricts the use of asHPAL as a biocatalyst for stereoselective aldol reactions. The molecular mechanism of this substrate selectivity will provide insight into how to expand the substrate specificity of asHPAL; however, the mechanism remains unclear. In this chapter, I describe the structural basis of the substrate specificity of asHPAL, especially the size of the branched-chain moiety at the C4 position of α -keto acids, and the structure-based design of asHPAL mutants with expanded substrate specificity toward 4-methyl-2-oxovalerate, an α -keto acid with an isopropyl group at the C4 position.

The structures of asHPAL in complex with pyruvate, oxamate, and 4-methyl-2-oxovalerate were determined at 1.97 Å, 1.81 Å, and 1.60 Å resolutions, respectively. These structures explained the binding mode and chemical properties of the substrates, required for the aldol reaction to proceed. Based on the structure of the asHPAL-4-methyl-2-oxovalerate complex, docking simulations were conducted to search for the active-site mutations that would allow 4-methyl-2-oxovalerate to bind in the same manner as the natural substrates. The expanded substrate specificities of engineered asHPALs were confirmed by the production of 2-amino-3-isopropyl-4-oxido-pentanoate, which was converted from 4-methyl-2-oxovalerate by sequential reaction with BCAT (Fig. 4-1).

4.2 Materials and methods

4.2.1 Crystallization of asHPAL complexed with pyruvate, oxamate, and 4-methyl-2-oxovalerate

asHPAL was prepared according to the procedures described in Sections 2.2.3 and 2.2.4, and the purified asHPAL (10 mg ml^{-1}) was used for crystallization experiments. Based on the co-crystallization conditions of the asHPAL-2-ketobutyrate complex, each compound (pyruvate, oxamate, and 4-methyl-2-oxovalerate) was added into the protein solution at the final concentration of 200 mM before crystallization. Each drop was prepared by mixing equal volumes ($2.0 \mu\text{l}$) of the protein solution and a reservoir solution containing 100 mM HEPES-Na (pH 7.7), 30% (v/v) PEG 400, and 200 mM MgCl_2 using 24-well Cryschem plates for the sitting-drop vapor diffusion method (Hampton Research). The drops were equilibrated against $400 \mu\text{l}$ of the reservoir solution at 293 K.

4.2.2 Data collection and processing

Each asHPAL crystal was picked up using a nylon loop (Hampton Research) and was transferred to a cryoprotectant solution prepared by mixing 76% (v/v) of the reservoir solution and 24% (v/v) of glycerol. The nylon loop was mounted on the X-ray diffractometer and was flash-cooled in a liquid nitrogen stream (95 K).

For the asHPAL crystals obtained in the presence of pyruvate or oxamate, the X-ray diffraction data sets (360 images per a data set) were collected with an FR-E SuperBright rotating anode generator (Rigaku) and an R-AXIS VII detector (Rigaku). The parameters of data collection were as follows: wavelength, 1.54 \AA (Cu $K\alpha$); total collection angle, 180° ; oscillation angle, 0.5° ; crystal-to-detector distance, 150 mm; and exposure time, 60 sec. The

diffraction data sets were indexed, integrated, and scaled with the XDS Program Package [66].

For the asHPAL crystal obtained in the presence of 4-methyl-2-oxovalerate, the X-ray diffraction experiments were performed at the AR-NW12A beamline of Photon Factory (Ibaraki, Japan). The diffraction data set (600 images) was collected at a wavelength of 1.0000 Å using an ADSC Quantum-210 CCD detector. Other parameters were as follows: total collection angle, 180°; oscillation angle, 0.3°; crystal-to-detector distance, 142 mm; and exposure time, 1.0 sec. The diffraction data were indexed, integrated, and scaled with HKL2000 [74].

4.2.3 Structure determination and refinement.

Subsequent data processing was performed using the CCP4 software package [55]. Molecular replacement was achieved using the coordinates of asHPAL as a search model with the MOLREP [56]. Alternate cycles of refinement were performed using WinCoot [58] and Refmac5 [59]. PROCHECK [60] was used to evaluate the refinement models. Figures were prepared using PyMOL [16]. The RMSD values for superimposed structures were calculated using Dali pairwise comparison service [62].

4.2.4 Docking simulation of 4-methyl-2-oxovalerate

The docking simulations of 4-methyl-2-oxovalerate to asHPAL F177A mutant were performed using the program suite MOE [67] according to the method described in Section 3.2.6. The crystal structure of the asHPAL-2-ketobutyrate complex was used as a starting model for the simulations. All water molecules and 2-ketobutyrate were removed from the model, and the residue Phe177 was then substituted to alanine. All hydrogen atoms were then generated with the Protonate3D module of the MOE program. MMFF94x forcefield was used for the

energy minimization, and a series of minimizations was performed using the Energy Minimize module with the Tether Atoms set as Heavy, which means that the forcefield is applied to non-hydrogen and non-lone pair atoms.

Site Finder [68] module was used to choose the potential binding site of asHPAL F177A mutant for 4-methyl-2-oxovalerate, and the site located near Mg²⁺, His52, and Arg77 was chosen for the docking simulation of 4-methyl-2-oxovalerate. The docking simulations of 4-methyl-2-oxovalerate at the selected site were performed using the ASEDock [69] module in which the forcefield was set to MMFF94x. In the simulation, the docking models were roughly searched with the following parameters: cutoff, 4.5 Å; RMS gradient, 10 kcal mol⁻¹ Å⁻¹; and energy threshold, 500 kcal mol⁻¹. The binding mode of each model was optimized by energy minimization with the following parameters: lowest energy, 5 kcal mol⁻¹; cutoff, 8 Å; and RMS gradient, 0.1 kcal mol⁻¹ Å⁻¹. The obtained docking models were evaluated by the U_dock value, which corresponds to the docking energy.

4.2.5 Site-directed mutagenesis

The site-directed mutagenesis for the F177A and F177A/S181W mutations was performed using PrimeSTAR Max DNA Polymerase (Takara). The plasmid for the expression of asHPAL (Section 2.2.1) was used as a template, and the mutagenic primers are shown in Table 4-1. PCR was performed with the following cycle parameters: 30 cycles of 98°C for 10 sec, 55°C for 15 sec, and 72°C for 30 sec, followed by cooling to 4°C. The resulting plasmid was amplified in *E. coli* XL1-Blue (Stratagene), and was then extracted from the cells using the Wizard *Plus SV* Minipreps DNA Purification System (Promega). The mutation sites were verified by a DNA sequencing service of FASMAC. The F177A and F177A/S181W mutants were expressed as soluble proteins and were purified using the same method as for the wild-type asHPAL

(Sections 2.2.2 and 2.2.3).

4.2.6 Assay for aldolase activity toward 4-methyl-2-oxovalerate

The aldol reaction of the F177A and F177A/S181W mutants towards 4-methyl-2-oxovalerate and acetaldehyde was analyzed using ESI-TOF-MS. Each mutant (369 nM) was incubated in reaction solution containing 20 mM bis-tris-HCl (pH 6.0), 100 mM 4-methyl-2-oxovalerate, 100 mM acetaldehyde, 2 mM MgCl₂, 50 μM PLP, 200 mM L-Glu, and 369 nM BCAT for 12 h. BCAT was used to aminate the C3 atom of the product, 3-(1-hydroxyethyl)-4-methyl-2-oxo-pentanoate, which is unstable in the reaction solution. The reaction process is illustrated in Fig. 4-1. To observe the production of 2-amino-3-isopropyl-4-oxido-pentanoate, the reaction solution was mixed with an equal volume of methanol and was then loaded into the JMS-T100LLP time of flight mass spectrometer (JEOL) equipped with an ESI source (JEOL). The mobile phase was 100% methanol and was constantly pumped at 0.50 ml min⁻¹. The conditions for ESI-TOF-MS detection were as follows: positive ion mode; needle voltage, 2,000 V; ring lens voltage, 10 V; orifice 1 voltage, 70 V; and orifice 2 voltages, 10 V. desolvation gas temperatures, 523 K; desolvation gas flow, 573 l h⁻¹; and the orifice 1 temperatures, 353 K. Data were obtained using Mass Center software, MS-56010MP (JEOL).

Kinetics studies on the aldol reaction between 4-methyl-2-oxovalerate and acetaldehyde were measured using NMR spectroscopy according to the method described in Section 3.2.7 with some modifications. The reaction solution contained different concentrations of 4-methyl-2-oxovalerate (20, 25, 33, 50, or 100 mM) instead of 2-ketobutyrate. The NMR signals of α -proton (δ , 2.95 ppm) were observed to measure the reduction of 4-methyl-2-oxovalerate during the reaction (Fig. 4-2).

4.2.7 Assay for the inhibitory activity of oxamate

The aldol reaction between oxamate and acetaldehyde was observed by the signal reduction of the compounds in the ^1H NMR spectra of the reaction solution according to the method described in Section 3.2.7 with some modifications. The reaction solution was composed of 20 mM MOPS (pD 6.0), 2 mM MgCl_2 , $\text{DDS-}d_6$, 36.9 nM asHPAL, 100 mM oxamate, and 100 mM acetaldehyde. The reaction was initiated by the addition of asHPAL to a final concentration of 36.9 nM into the reaction solution, the solution (600 μl) was immediately moved into a 5-mm NMR tube (Shigemi), and the tube was loaded into the NMR spectrometer.

To measure the inhibitory activity of oxamate toward asHPAL, oxamate at the final concentration of 50 and 100 mM was added into the reaction solution containing 20 mM MOPS (pD 6.0), 2 mM MgCl_2 , 0.1 mM $\text{DDS-}d_6$, 369 nM asHPAL, 100 mM acetaldehyde, and different concentrations of 2-ketobutyrate (20, 25, 33, 50, or 100 mM). After adding the enzyme to the reaction solution to initiate the reaction, the solution (600 μl) was immediately moved into a 5-mm NMR tube (Shigemi), and the tube was loaded into the NMR spectrometer. The acquisition parameters for ^1H NMR measurements were the same as those described in Section 3.2.8. The Dixon plot [71] was used to determine the K_i value of oxamate against the aldol reaction catalyzed by asHPAL.

4.3 Results and discussion

4.3.1 Structure determination of asHPAL complexed with pyruvate, oxamate, and 4-methyl-2-oxovalerate

asHPAL crystals were obtained in the presence of pyruvate, oxamate, and 4-methyl-2-oxovalerate (Fig. 4-2), and the crystals diffracted X-rays to 1.97 Å, 1.81 Å, and 1.60 Å resolutions, respectively (Fig. 4-3). All crystals belonged to the space group *C2* with nearly identical unit cell parameters (Tables 4-3, 4-4, and 4-5). The Matthews coefficients of the crystals were 2.19 Å³ Da⁻¹ for pyruvate, 2.21 Å³ Da⁻¹ for oxamate, and 2.19 Å³ Da⁻¹ for 4-methyl-2-oxovalerate, indicating that the crystals contained three asHPAL molecules per asymmetric unit.

The structure of the asHPAL-pyruvate complex was determined at 1.97 Å resolution and was refined to an R_{work} of 20.5% and an R_{free} of 25.3%. Clear electron density was observed for pyruvate, which enabled the model building of pyruvate (Fig. 4-4A). Finally, an asymmetric unit of the crystal contained three asHPAL molecules consisting of residues 1–259, three Mg²⁺ ions, three pyruvate molecules, and 612 water molecules. SFCHECK analysis showed that 93.1% of all of the residues were in the most favored region and that the remaining residues were in the additionally allowed region of a Ramachandran plot. The refinement statistics are summarized in Table 4-3.

The structure of the asHPAL-oxamate complex was determined at 1.81 Å resolution and was refined to an R_{work} of 19.5% and an R_{free} of 25.3%. Clear electron density was observed for oxamate (Fig. 4-4B). Finally, an asymmetric unit of the crystal contained three asHPAL molecules consisting of residues 1–259, three Mg²⁺ ions, three oxamate molecules, and 711 water molecules. SFCHECK analysis showed that 93.8% of all of the residues were in the most favored region and that the remaining residues were in the additionally allowed region of a

Ramachandran plot. The refinement statistics are summarized in Table 4-4.

The structure of the asHPAL-4-methyl-2-oxovalerate complex was determined at 1.60 Å resolution and was refined to an R_{work} of 19.8% and an R_{free} of 23.4%. Clear electron density was observed for 4-methyl-2-oxovalerate, which enabled the model building of 4-methyl-2-oxovalerate (Fig. 4-4C). Finally, an asymmetric unit of the crystal contained three asHPAL molecules consisting of residues 1–259, three Mg^{2+} ions, three 4-methyl-2-oxovalerate molecules, and 696 water molecules. SFCHECK analysis showed that 93.3% of all of the residues were in the most favored region and that the remaining residues were in the additionally allowed region of a Ramachandran plot. The refinement statistics are summarized in Table 4-5.

4.3.2 Binding mode of pyruvate and oxamate at the active site of asHPAL

The overall structures of asHPAL-pyruvate and asHPAL-oxamate complexes showed no significant differences with that of the asHPAL-2-ketobutyrate complex (C_{α} RMSD of 0.081 Å and 0.079 Å, respectively) (Fig. 4-5A). The orientations of the residues in the active site were also unchanged in the structures of the three different complexes, and the positions of pyruvate and oxamate were the same as that of 2-ketobutyrate in the structures (Fig. 4-5B). Although the correct orientations of pyruvate and oxamate could not be determined with only crystallographic data, the O2 and O3 atoms of pyruvate and oxamate were considered to be coordinated to Mg^{2+} similarly to the binding of 2-ketobutyrate. As described in the reaction mechanism of asHPAL toward 2-ketobutyrate (Section 3.3.6), the aldol reaction catalyzed by asHPAL requires contact between the C3 atom of α -keto acids and the C1 atom of acetaldehyde. asHPAL can also catalyze the aldol reaction between pyruvate and acetaldehyde. Therefore, the C3 atom of pyruvate was considered to be located near Arg77, which is the residue for binding

acetaldehyde, during the aldol reaction. However, the orientation of the C3 atom may not be strictly defined because there is no residue that recognizes the methyl group and the carbonyl oxygen at the C3 and O1 positions of pyruvate.

Generally, class II aldolases cannot utilize oxamate as a substrate. In accordance with this notion, the aldol reaction of asHPAL was not observed when oxamate was used as a substrate instead of 2-ketobutyrate (Fig. 4-6). However, the crystal structure of the asHPAL-oxamate complex showed the same binding mode as for the preferable substrates, pyruvate and 2-ketobutyrate (Fig. 4-5B). This structural evidence was confirmed by the inhibition assay with oxamate. As shown in Fig. 4-7, a Dixon plot showed that oxamate competitively inhibited the activity of asHPAL with the K_i value of 216 ± 24 mM in the aldol reaction between 2-ketobutyrate and acetaldehyde. These results indicate that the binding mode of oxamate does not explain why oxamate is not suitable as a substrate for asHPAL. Compared with the chemical structure of pyruvate, the methyl group at the C3 position of pyruvate is substituted to the amino group in oxamate. Due to this structural difference, oxamate does not adopt the enolate form, which supports that the enolate form of substrates is a crucial intermediate for the aldol reaction catalyzed by asHPAL.

4.3.3 Binding mode of 4-methyl-2-oxovalerate at the active site of asHPAL

The structural alignment of the asHPAL-4-methyl-2-oxovalerate complex with the asHPAL-2-ketobutyrate complex showed no significant structural differences in the overall structures (C_α RMSD of 0.143 Å) or the side-chain orientations of active-site residues (Fig. 4-8). However, the orientation of 4-methyl-2-oxovalerate in the active site was opposite that of 2-ketobutyrate (Fig. 4-8). In the structure of the asHPAL-2-ketobutyrate complex, Phe177 was close to the methyl group of 2-ketobutyrate at the C4 position (Fig. 4-9A). The structural

evidence suggested that Phe177 defined the space for accepting the methyl group of 2-ketobutyrate. When 4-methyl-2-oxovalerate is assumed to bind to the active site in the same orientation as 2-ketobutyrate, Phe177 could cause steric hindrance with the isopropyl group at the C4 position of 4-methyl-2-oxovalerate. Due to this steric hindrance, 4-methyl-2-oxovalerate could be restricted in the opposite direction from 2-ketobutyrate in the active site of asHPAL (Fig. 4-9B). In the binding orientation of 4-methyl-2-oxovalerate, the C3 atom was located far from the binding site of acetaldehyde, which explains why asHPAL cannot use 4-methyl-2-oxovalerate as a substrate of the aldol reaction.

4.3.4 Mutations for expanding the substrate specificity of asHPAL toward 4-methyl-2-oxovalerate

The structure of the asHPAL-4-methyl-2-oxovalerate complex suggested that Phe177 restricted the substrate specificity of asHPAL to pyruvate and 2-ketobutyrate. If the residue Phe177 is substituted by other residues with small side chains, 4-methyl-2-oxovalerate may bind at the active site in the same orientation as 2-ketobutyrate and be used as a substrate in the aldol reaction catalyzed by asHPAL. According to this hypothesis, the docking simulation was used to evaluate whether the binding orientation of 4-methyl-2-oxovalerate inverts at the active site of asHPAL F177A mutant, which is expected to expand the space for accepting the methyl group of 2-ketobutyrate. Simulated docking models were selected by the U_dock score. A lower score indicates that the binding model is more stable. Fig. 4-10 showed the top 6 most stable models of 4-methyl-2-oxovalerate binding to the F177A mutant. When the O2 and O3 atoms of 4-methyl-2-oxovalerate bound to Mg²⁺ in the docking model, the U_dock scores were less than -41 kcal/mol. In accordance with the crystal structure of the asHPAL-4-methyl-2-oxovalerate complex, the binding of 4-methyl-2-oxovalerate was stabilized by the coordination

of the O2 and O3 atoms with Mg^{2+} . Among the top 3 most stable binding models, model 1 showed nearly the same orientation as 2-ketobutyrate in the active site of asHPAL (Fig. 4-10A).

Because the docking simulation showed the possibility that the F177A mutant could catalyze the aldol reaction of 4-methyl-2-oxovalerate, I attempted to detect 2-amino-3-isopropyl-4-oxido-pentanoate, which is expected to be converted from 4-methyl-2-oxovalerate and acetaldehyde by the coupled reaction of the F177A mutant and BCAT. As shown in Fig. 4-11, the reaction product was successfully observed as a sodium salt ($[M + 2Na]^+$, m/z 219.07) on the ESI-TOF-MS spectrum when the reaction solution contained the F177A mutant. The MS peak with m/z 219.07 was not observed in the wild-type asHPAL, which strongly suggests that the F177A mutant exerts substrate specificity towards 4-methyl-2-oxovalerate.

The initial reaction rates of the F177A mutant were measured at different concentrations of 4-methyl-2-oxovalerate using NMR spectroscopy (Fig. 4-12A). The activity of the F177A mutant was observed when 4-methyl-2-oxovalerate was used as a substrate. The kinetic parameters were calculated by the Lineweaver-Burk plot with the initial reaction rates (Fig. 4-12B). The K_m value of the F177A mutant was 20.1 ± 1.8 mM toward 4-methyl-2-oxovalerate (Table 4-6). Compared with the K_m value of the wild-type enzyme toward 2-ketobutyrate (25.5 ± 2.5 mM, Table 3-5), the binding affinity of 4-methyl-2-oxovalerate to the F177A mutant was almost equal to that of 2-ketobutyrate to the wild-type enzyme. This result suggests that the major structural basis for substrate binding may be the coordination between Mg^{2+} and the O2 and O3 atoms of 4-methyl-2-oxovalerate, which is an interaction that 2-ketobutyrate shares in the wild-type enzyme. The k_{cat} value of the F177A mutant was 70.6 ± 2.4 s⁻¹ toward 4-methyl-2-oxovalerate (Table 4-6). The turnover rate was decreased to ~30% compared with that of the wild-type enzyme toward 2-ketobutyrate (213.2 ± 7.7 s⁻¹, Table 3-5). The decreased activity may be caused by the flexibility of substrate orientations at the active site.

Additional mutations were investigated to restrict the orientation of 4-methyl-2-

oxovalerate binding. I focused on the S181W mutation, which is expected to restrict the orientation of 4-methyl-2-oxovalerate in the same manner as that of 2-ketobutyrate by sealing the binding site for the isopropyl group of 4-methyl-2-oxovalerate (Fig. 4-13). The initial reaction rates of the F177A/S181W mutant were measured at different concentrations of 4-methyl-2-oxovalerate using NMR spectroscopy (Fig. 4-14A). The activity toward 4-methyl-2-oxovalerate was retained by the F177A/S181W mutation. The kinetic parameters were calculated by the Lineweaver-Burk plot with the initial reaction rates (Fig. 4-14B). The K_m values of the F177A/S181W mutant (26.7 ± 0.6 mM, Table 4-6) were not largely different from the wild-type asHPAL (25.5 ± 2.5 mM, Table 3-5) or the F177A mutant (20.1 ± 1.8 mM, Table 4-6). However, the k_{cat} value of the F177A mutant toward 4-methyl-2-oxovalerate was increased from 70.6 ± 2.4 s⁻¹ to 136.3 ± 0.6 s⁻¹ by the additional S181W mutation (Table 4-6).

4.4 Conclusion

Three structures of asHPAL were determined as complexes with pyruvate, oxamate, and 4-methyl-2-oxovalerate in addition to the complex with 2-ketobutyrate. The structures reveal a detailed structural basis for the binding of α -keto acids as substrates. α -Keto acids possess the O2 and O3 atoms as common moieties, and the Mg^{2+} coordination of these atoms is a major interaction between asHPAL and α -keto acids. In addition, the binding orientation of substrates at the active site is crucial for the substrate specificity because the aldol reactions can proceed when the C3 atom of an α -keto acid is close to the C2 atom of acetaldehyde.

The structure of asHPAL in complex with 4-methyl-2-oxovalerate and the mutational data revealed that Phe177 restricted the binding of 4-methyl-2-oxovalerate in the active site in an orientation opposite from 2-ketobutyrate. The F177A mutant, which was engineered by the crystal structure of asHPAL and simulation approaches, acquired the catalytic activity for the aldol reaction between 4-methyl-2-oxovalerate and acetaldehyde. Moreover, an additional S181W mutation increased the turnover rate of the F177A mutant toward 4-methyl-2-oxovalerate as a substrate, which reveals that restricting substrate orientations can enhance the catalytic activity of asHPAL.

The results in this chapter include the novel findings for the HpaI/HpcH-aldolase subfamily, and these findings deepen our understanding of the structural basis for substrate specificity. In addition, the structural basis successfully enabled the design of an asHPAL mutant as a potential biocatalyst for the stereoselective aldol reaction between 4-methyl-2-oxovalerate and acetaldehyde. The F177A/S181W mutant exhibited half of the activity toward 4-methyl-2-oxovalerate compared with the wild-type enzyme toward 2-ketobutyrate.

Table 4-1 Mutagenic primers.^a

Mutants	Forward primer	Reverse primer
F177A	5-gctatc <u>gcg</u> atcggcccttccgacttg-3	5-gccgatc <u>gcg</u> gatagcatcgacgccatc-3
S181W	5-ggccctt <u>ggg</u> acttggtgcttccatg-3	5-caagt <u>cca</u> agggccgatgaagatagc-3

^a Labeled bases were the variation locus.

Table 4-2 Concentrations of 4-methyl-2-oxovalerate and acetaldehyde used for kinetics studies on asHPAL mutants with 4-methyl-2-oxovalerate

Concentration (mM)	
4-methyl-2-oxovalerate	acetaldehyde
100	100
50	100
33	100
25	100
20	100

Table 4-3 Data collection and refinement statistics of asHPAL-pyruvate complex.

<i>Data collection</i>	
X-ray source	FR-E SuperBright
Wavelength (Å)	1.00000
Spacegroup	C2
Unit cell dimensions (Å)	$a = 120.4, b = 90.8, c = 86.8$
(°)	$\beta = 124.4$
Resolution (Å)	50.0–1.97 (2.00–1.97) ^a
Observed reflections	197334
Unique reflections	51800
Completeness (%)	99.7 (99.0) ^a
R_{meas} (%) ^b	5.2 (23.3) ^a
$I/\sigma(I)$	28.0 (7.1) ^a
 <i>Refinement</i>	
Resolution (Å)	20.0–1.97
$R_{\text{work}} / R_{\text{free}}$ (%) ^c	20.1 / 25.0
RMSD bond length (Å)	0.012
RMSD bond angle (°)	1.415
Ramachandran plot (%)	
Favored	93.1
Additionally allowed	6.9
Generously allowed	0
disallowed	0

^a Values in parentheses are for the highest-resolution shell.

^b $R_{\text{meas}} = \sum_{hkl} [(\sum_i |I_i - \langle I \rangle|) / \sum_i |I_i|]$.

^c $R_{\text{work}} = (\sum_{hkl} ||F_o| - |F_c||) / \sum_{hkl} |F_o|$. R_{work} was calculated with 95% of the data used for refinement, and R_{free} was calculated with 5% of the data excluded from refinement.

Table 4-4 Data collection and refinement statistics of asHPAL-oxamate complex.

<i>Data collection</i>	
X-ray source	FR-E SuperBright
Wavelength (Å)	1.00000
Spacegroup	C2
Unit cell dimensions (Å)	$a = 121.0, b = 89.7, c = 87.4$
(°)	$\beta = 124.5$
Resolution (Å)	50.0–1.81 (1.85–1.81) ^a
Observed reflections	205879
Unique reflections	56649
Completeness (%)	99.8 (98.4) ^a
R_{meas} (%) ^b	4.2 (19.3) ^a
$I/\sigma(I)$	20.7 (3.1) ^a
 <i>Refinement</i>	
Resolution (Å)	20.0–1.81
$R_{\text{work}} / R_{\text{free}}$ (%) ^c	19.2 / 25.1
RMSD bond length (Å)	0.009
RMSD bond angle (°)	1.166
Ramachandran plot (%)	
Favored	93.8
Additionally allowed	6.2
Generously allowed	0
disallowed	0

^a Values in parentheses are for the highest-resolution shell.

^b $R_{\text{meas}} = \sum_{hkl} [(\sum_i |I_i - \langle I \rangle|) / \sum_i |I_i|]$.

^c $R_{\text{work}} = (\sum_{hkl} ||F_o| - |F_c||) / \sum_{hkl} |F_o|$. R_{work} was calculated with 95% of the data used for refinement, and R_{free} was calculated with 5% of the data excluded from refinement.

Table 4-5 Data collection and refinement statistics of asHPAL-4-methyl-2-oxovalerate complex.

<i>Data collection</i>	
X-ray source	PF NW12A
Wavelength (Å)	1.00000
Spacegroup	C2
Unit cell dimensions (Å)	$a = 121.4, b = 89.4, c = 87.4$
(°)	$\beta = 124.4$
Resolution (Å)	20.00–1.60 (1.63–1.60) ^a
Total observations	367756
Unique observations	101493
Completeness (%)	99.1 (99.1) ^a
R_{merge} (%) ^b	3.4 (18.2) ^a
$I/\sigma(I)$	42.3 (7.4) ^a
<i>Refinement</i>	
Resolution range used for refinement	20.0–1.60
$R_{\text{work}}/ R_{\text{free}}$ (%) ^c	19.8 / 23.4
RMSD bond length (Å)	0.023
RMSD bond angle (°)	2.225
Ramachandran plot (%)	
Favored	93.3
Additionally allowed	6.7
Generously allowed	0
disallowed	0

^a Values in parentheses are for the highest-resolution shell.

^b $R_{\text{merge}} = \sum_{hkl} [(\sum_i |I_i - \langle I \rangle|) / \sum_i |I_i|]$.

^c $R_{\text{work}} = (\sum_{hkl} ||F_o| - |F_c||) / \sum_{hkl} |F_o|$. R_{work} was calculated with 95% of the data used for refinement, and R_{free} was calculated with 5% of the data excluded from refinement.

Table 4-6 Kinetics study of asHPAL mutants toward 4-methyl-2-oxovalerate

	K_m (mM)	k_{cat} (s ⁻¹)
F177A	20.1 ± 1.8	70.6 ± 2.4
F177A/S181W	26.7 ± 0.6	136.3 ± 0.6

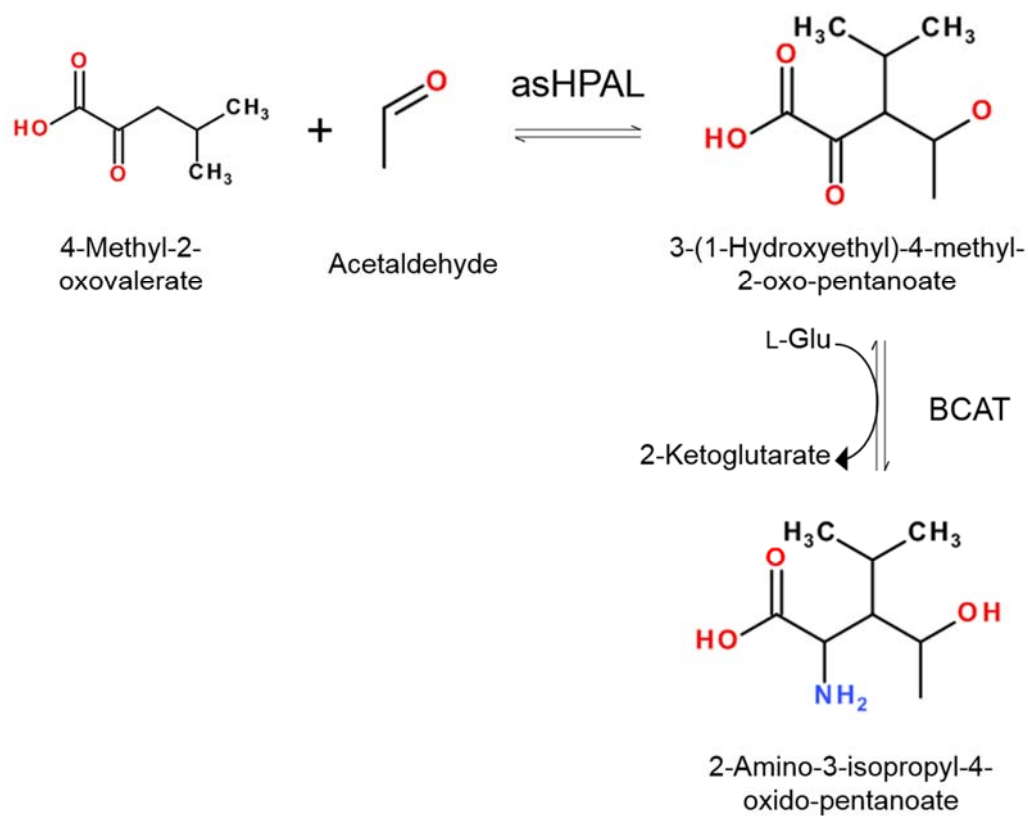


Fig. 4-1 Two-step enzymatic synthesis of 2-amino-3-isopropyl-4-oxido-pentanoate using an engineered asHPAL mutant and BCAT.

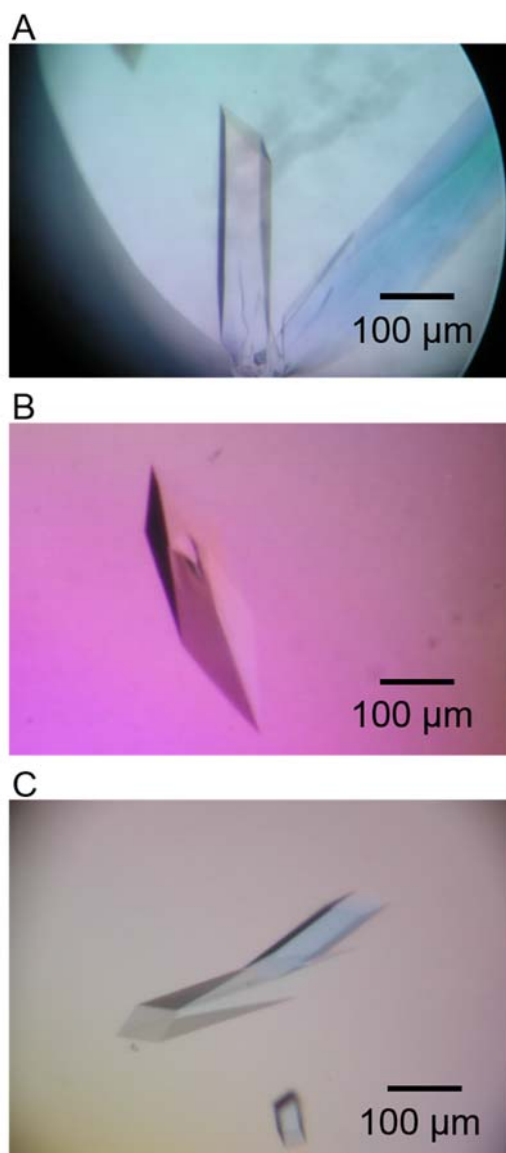


Fig. 4-2 asHPAL crystals obtained in the presence of some α -keto acids.
(A) Crystals of asHPAL obtained as co-crystals with pyruvate.
(B) Crystal of asHPAL obtained as co-crystal with oxamate.
(C) Crystals of asHPAL obtained as co-crystals with 4-methyl-2-oxovalerate.

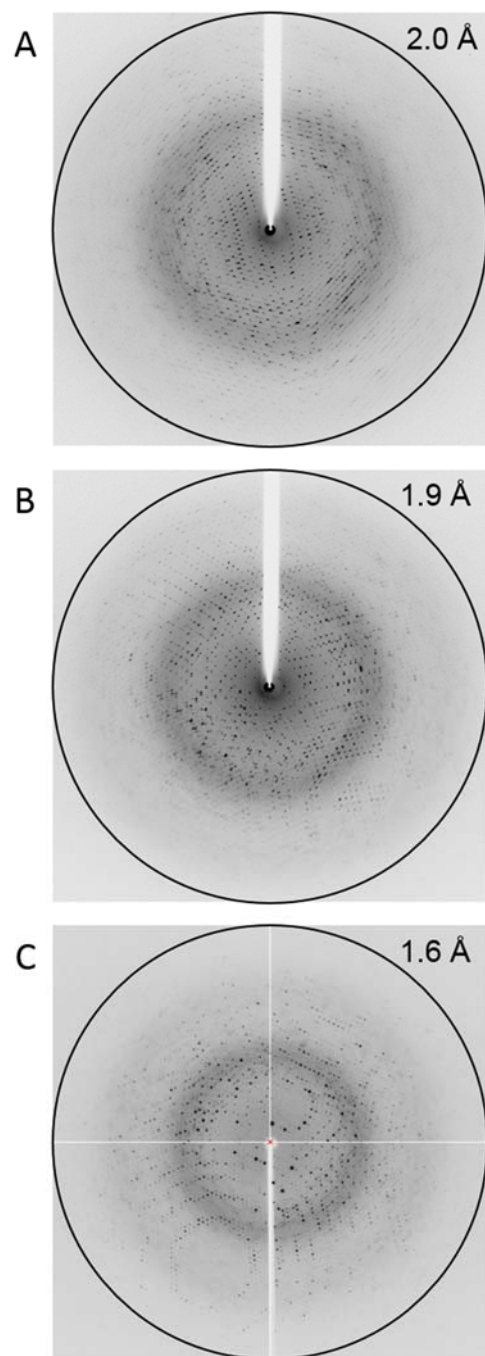


Fig. 4-3 X-ray diffraction images obtained from the asHPAL crystals.
(A) X-ray diffraction image of asHPAL-pyruvate co-crystal.
(B) X-ray diffraction image of asHPAL-oxamate co-crystal.
(C) X-ray diffraction image of asHPAL-4-methyl-2-oxovalerate co-crystal.

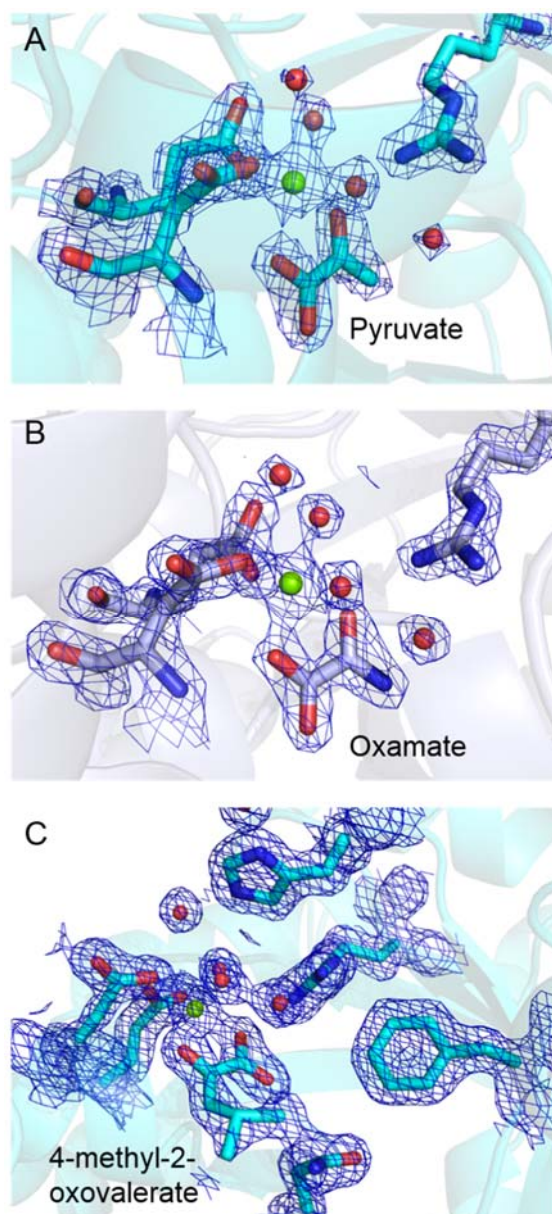


Fig. 4-4 Complex structures of the active site of asHPAL and α -keto acids. Clear electron density is visible for pyruvate (A), oxamate (B), and 4-methyl-2-oxovalerate molecule (C). Water molecules and Mg^{2+} ions are represented by red and green spheres, respectively. Blue mesh showed the $2|F_o|-|F_c|$ omit map (2.0σ)

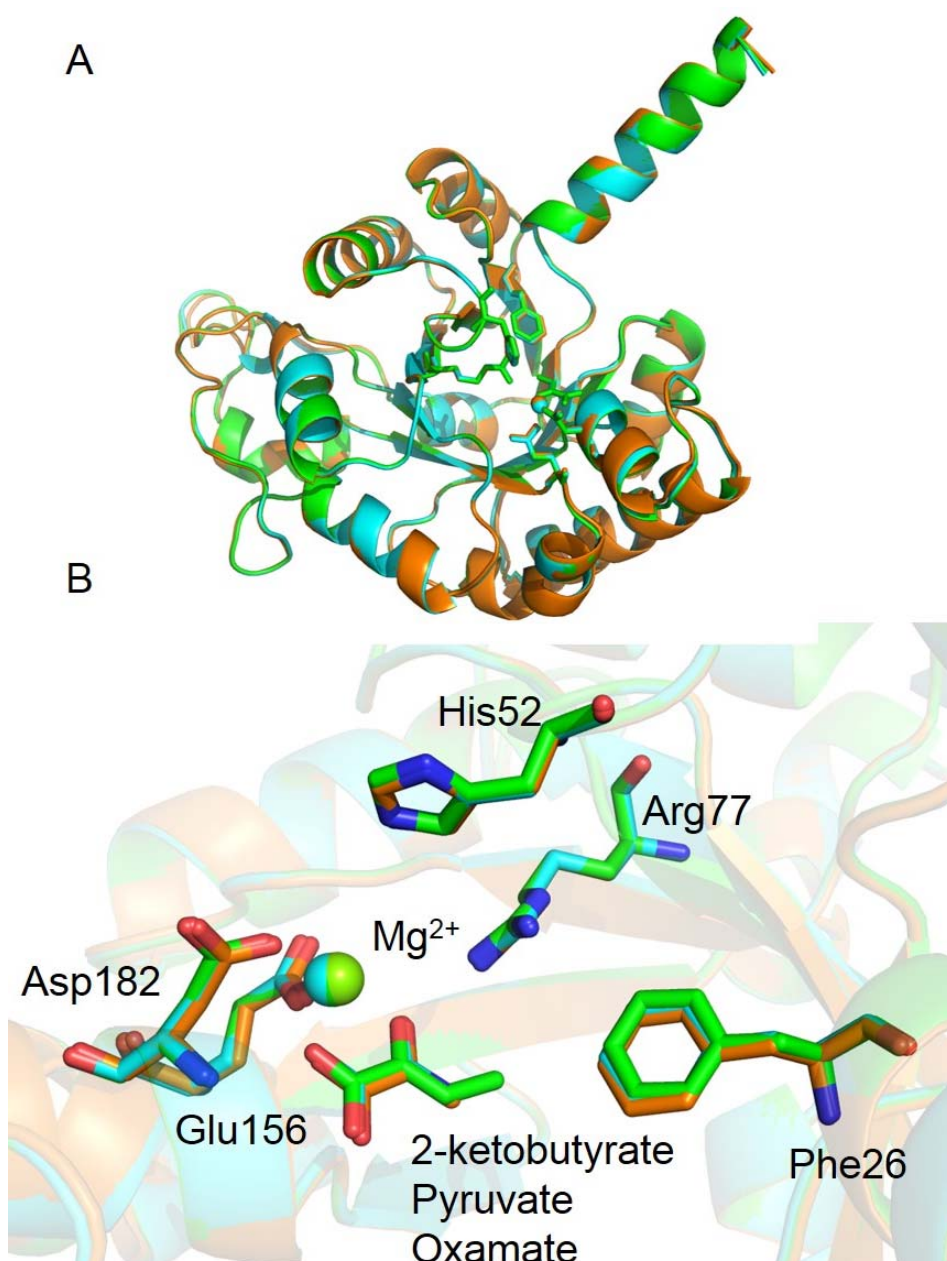


Fig. 4-5 Superposition of asHPAL structures in complex with 2-ketobutyrate (green), pyruvate (orange), and oxamate (cyan).

The asHPAL structures in complex with pyruvate and oxamate show no significant difference with the structure of asHPAL-2-ketobutyrate complex (C_{α} RMSD of 0.081 Å and 0.079 Å, respectively). Pyruvate and oxamate bond to asHPAL in the same fashion as 2-ketobutyrate: Mg²⁺ ion is coordinated with the O2 and O3 atoms of the α -keto acids.

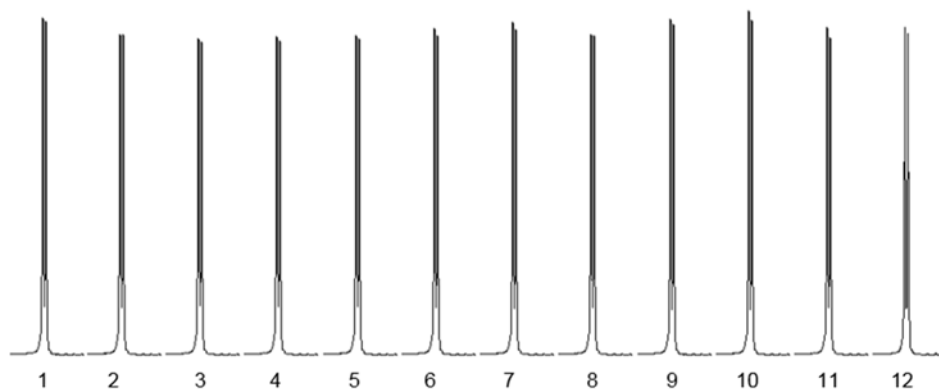


Fig. 4-6 Time-dependent changes of the ¹H NMR signals acetaldehyde in the reaction mixture containing oxamate instead of 2-ketobutyrate.

The signal strength of acetaldehyde was not decreased during the reaction of asHPAL when oxamate was added into the reaction solution instead of 2-ketobutyrate.

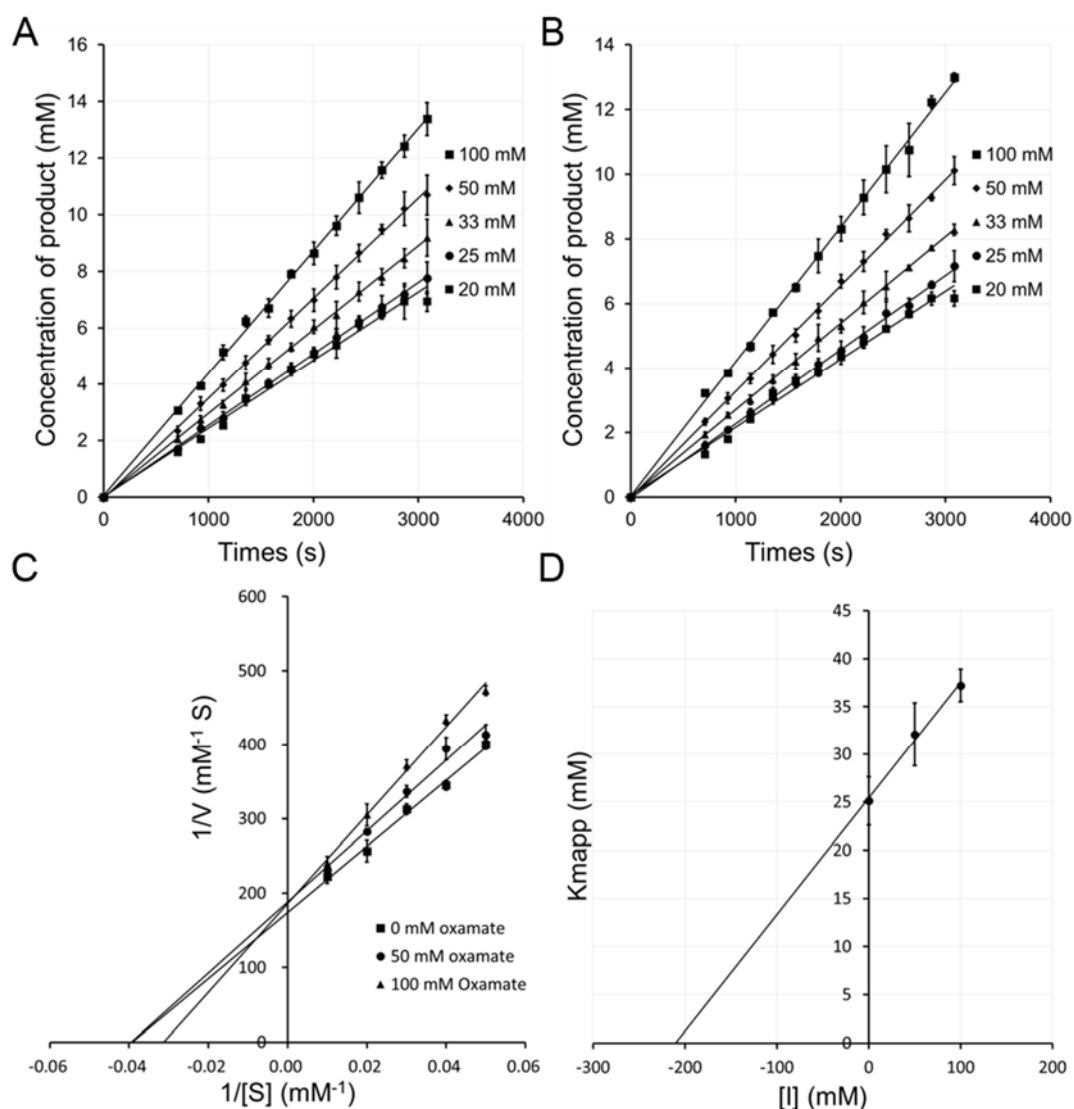


Fig. 4-7 Inhibitory activity of oxamate in the aldol reaction of asHPAL.

(A) Time-dependent HMKP production by asHPAL in the presence of 50 mM oxamate.

(B) Time-dependent HMKP production by asHPAL in the presence of 100 mM oxamate.

(C) Lineweaver–Burk plots for kinetic analysis of asHPAL in the presence of oxamate.

(D) Dixon plots for determining the inhibition mode of oxamate.

The reduced 2-ketobutyrate concentrations are considered as the produced concentrations of HMKP. All determinations were performed in triplicate. Error bars show standard deviations.

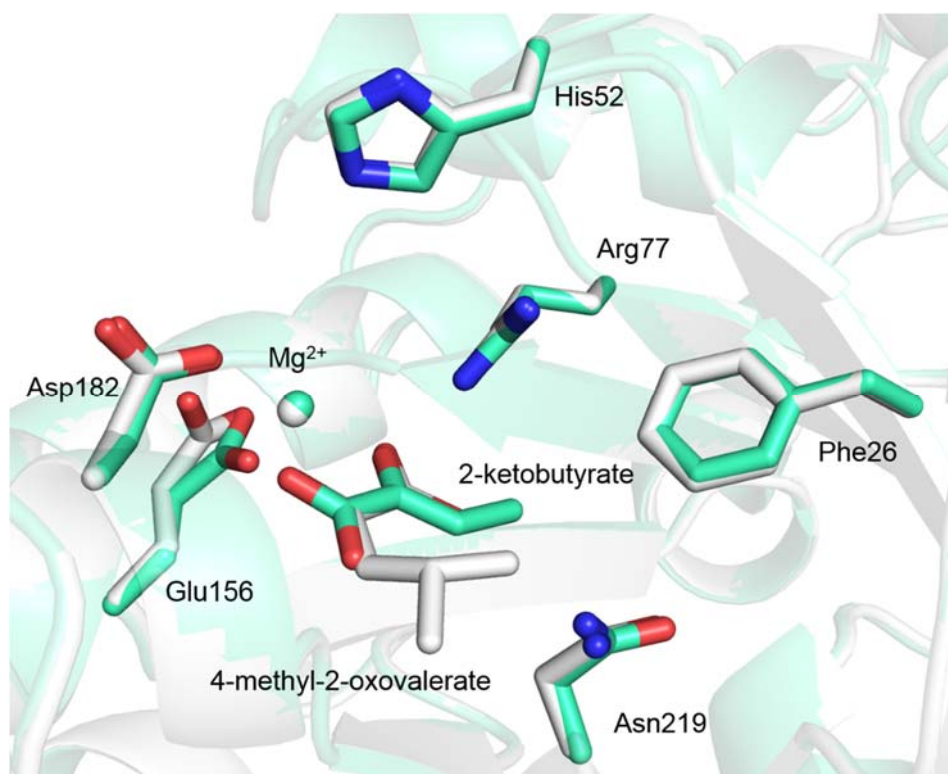


Fig. 4-8 Superposed structures of asHPAL in complex with 4-methyl-2-oxovalerate (white) and 2-ketobutyrate (cyan).

The direction of 4-methyl-2-oxovalerate at the active site was opposite with that of 2-ketobutyrate.

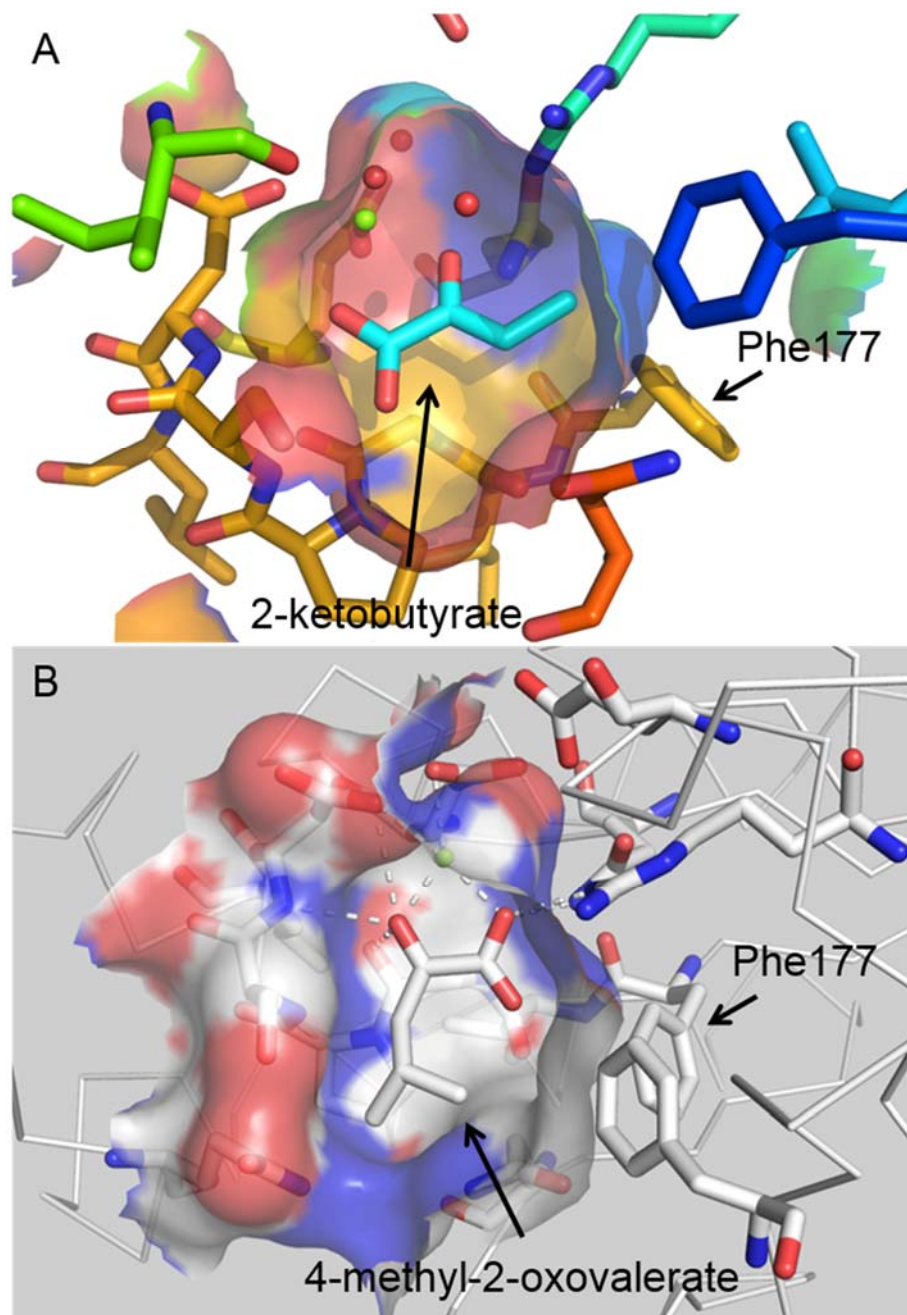


Fig. 4-9 Binding mode of 2-ketobutyrate (A) and 4-methyl-2-oxovalerate (B) at the active site.

Phe177 is located near the methyl group at the C4 position of 2-ketobutyrate in panel A.

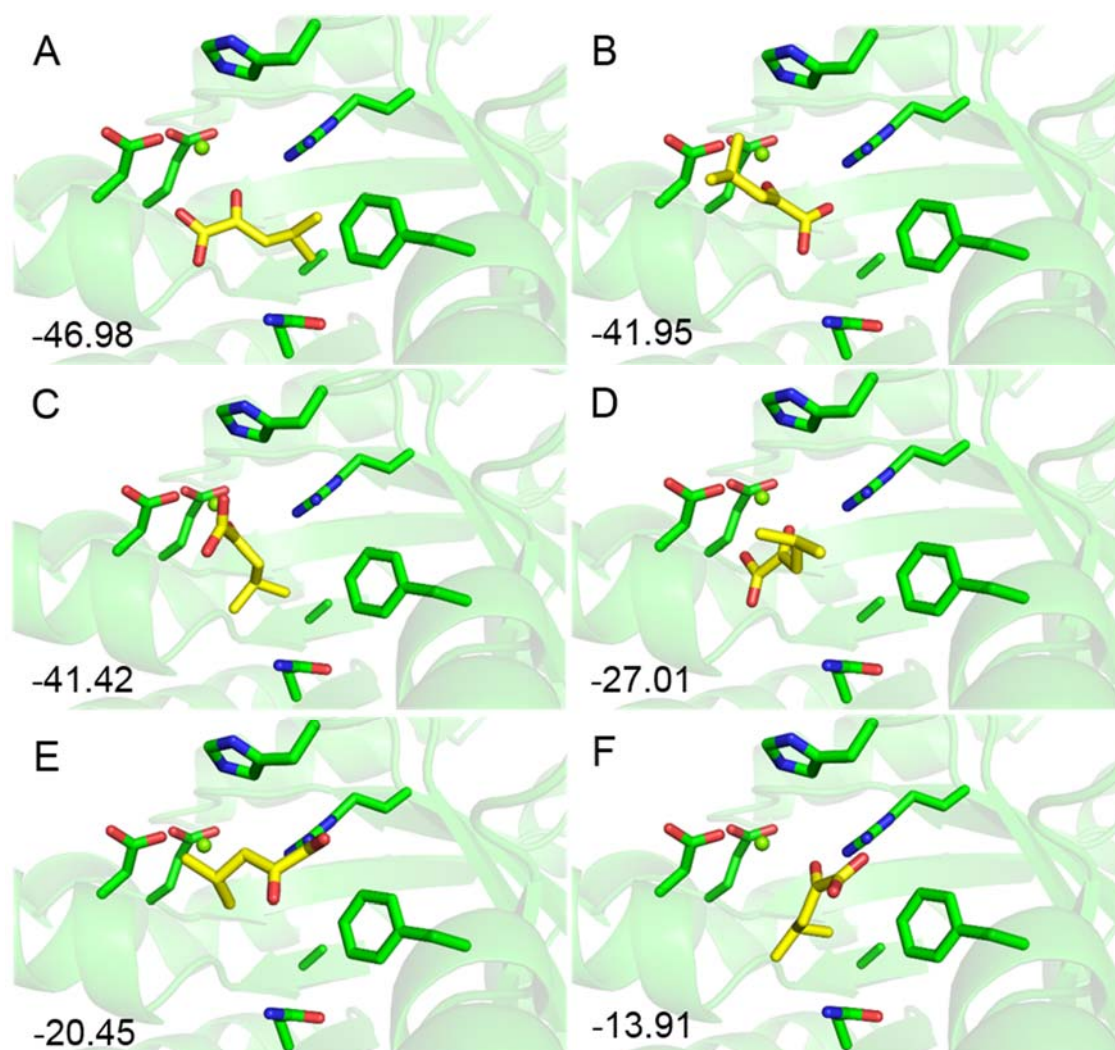


Fig. 4-10 Top 6 of the stable binding models of 4-methyl-2-oxovalerate to F177A mutant.

(A) Model 1; (B) Model 2; (C) Model 3, (D) Model 4; (E) Model 5; and (F) Model 6. The values show U_{dock} scores (kcal mol^{-1}), which are calculated by U_{ele} (electric energy)+ U_{vdw} (van der Waals energy)+ U_{solv} (Solvation energy)+ U_{strain} (Strain energy). Mg^{2+} ions and 4-methyl-2-oxovalerate are represented by spheres and yellow sticks, respectively.

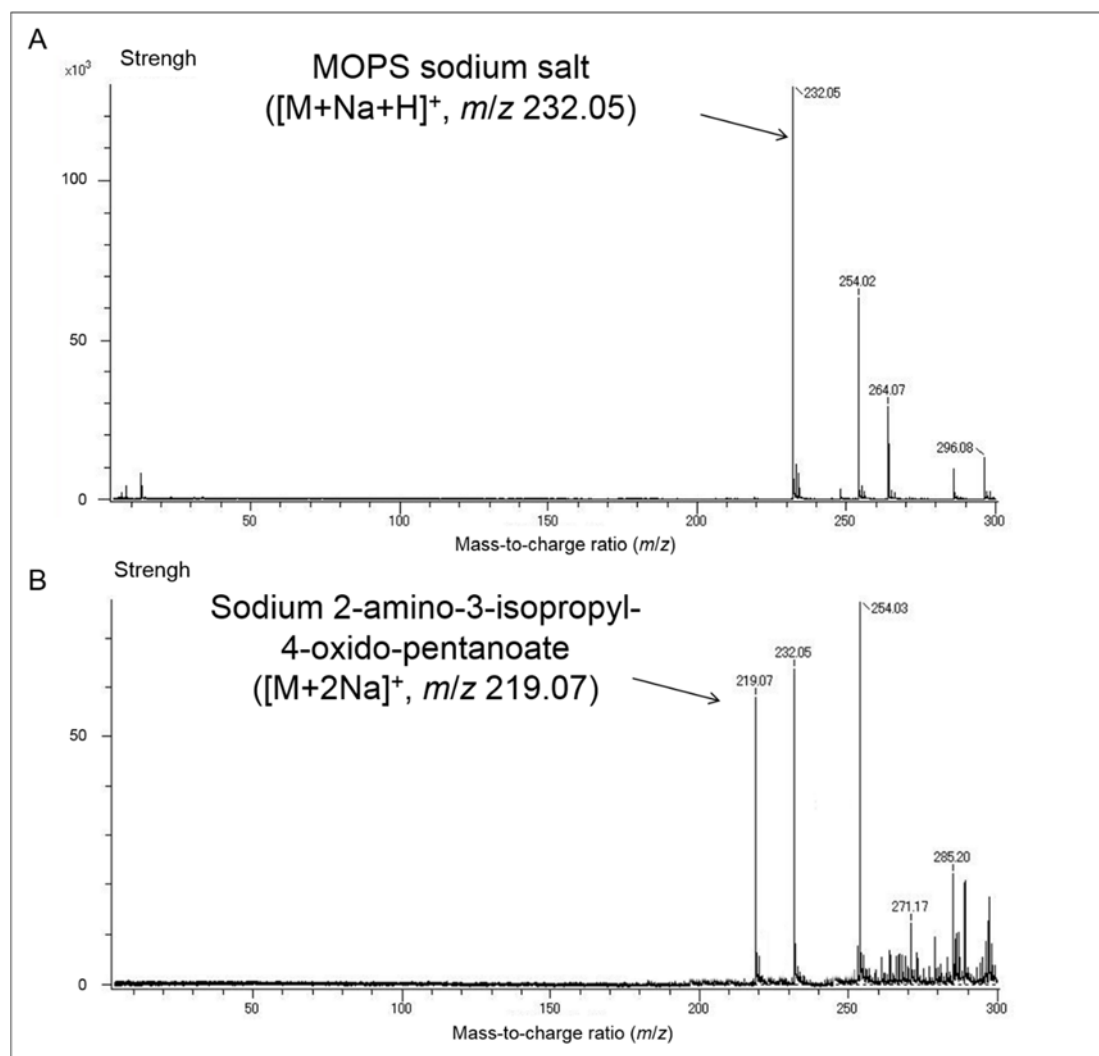


Fig. 4-11 MS spectra of the reaction mixture including the wild-type asHPAL (A) and the F177A mutant (B).

Reaction product was successfully observed as a sodium salt ($[M+2Na]^+, m/z 219.07$) in panel B.

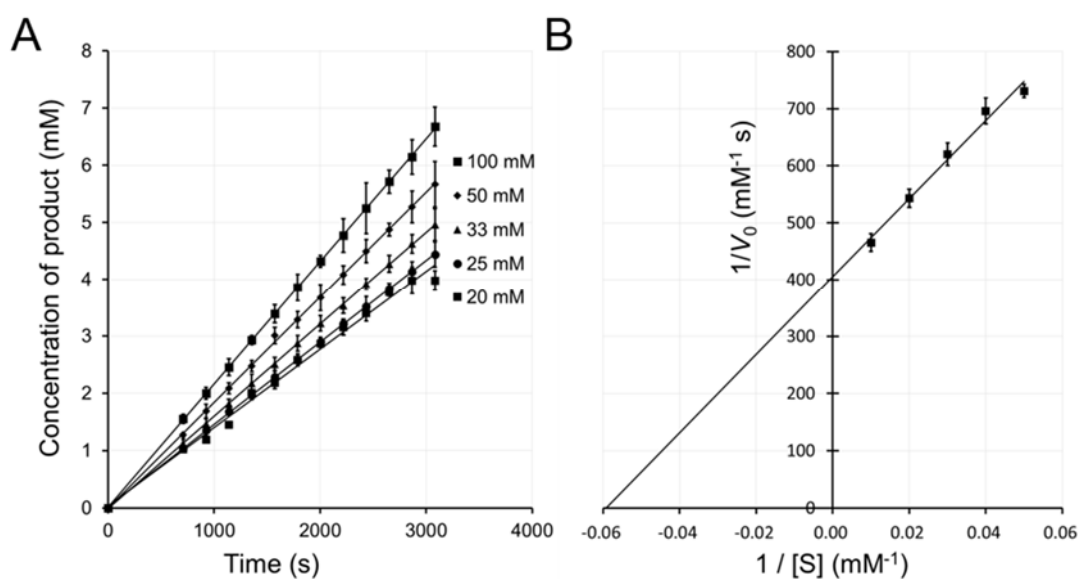


Fig. 4-12 Lineweaver–Burk plots for kinetic analysis of F177A mutant.

(A) Time-dependent production of 3-(1-hydroxyethyl)-4-methyl-2-oxo-pentanoate by the F177A mutant.

(B) Lineweaver–Burk plots for kinetic analysis of F177A mutant at varying concentrations of 3-(1-hydroxyethyl)-4-methyl-2-oxo-pentanoate.

The reduced 4-methyl-2-oxovalerate concentrations are considered as the produced concentrations of 3-(1-hydroxyethyl)-4-methyl-2-oxo-pentanoate. All determinations were performed in triplicate. Error bars show standard deviations.

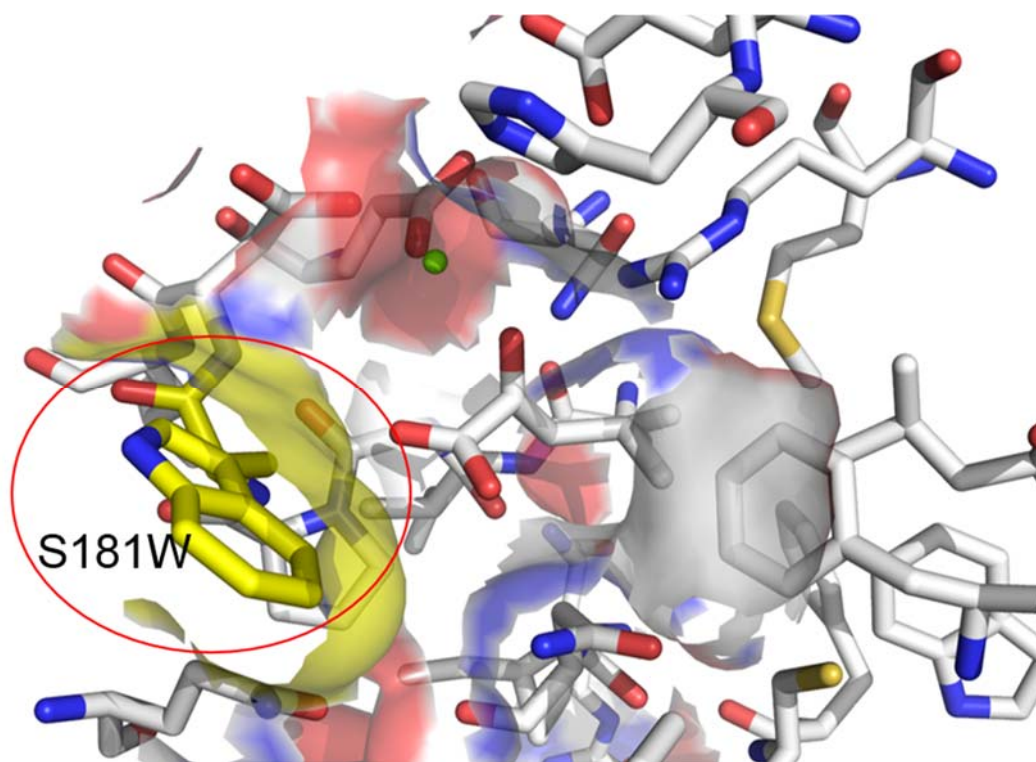


Fig. 4-13 Restriction of the orientation of 4-methyl-2-oxovalerate by S181W mutation. The S181W mutation is expected to restrict the orientation of 4-methyl-2-oxovalerate in the same manner as that of 2-ketobutyrate by sealing the binding site for the isopropyl group of 4-methyl-2-oxovalerate.

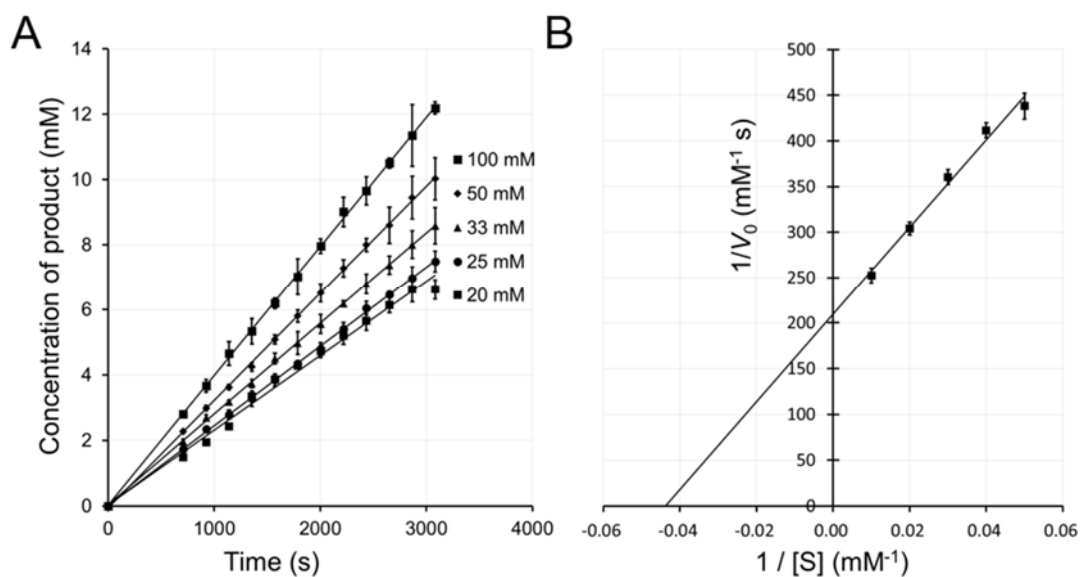


Fig. 4-14 Lineweaver–Burk plots for kinetic analysis of F177A/S181W mutant.

(A) Time-dependent production of 3-(1-hydroxyethyl)-4-methyl-2-oxo-pentanoate by the F177A/S181W mutant.

(B) Lineweaver–Burk plots for kinetic analysis of F177A/S181W mutant at varying concentrations of 3-(1-hydroxyethyl)-4-methyl-2-oxo-pentanoate.

The reduced 4-methyl-2-oxovalerate concentrations were considered as the produced concentrations of 3-(1-hydroxyethyl)-4-methyl-2-oxo-pentanoate. All determinations were performed in triplicate. Error bars show standard deviations.

Chapter 5

General discussion

In this study, the crystal structures of asHPAL were determined in six different states: four complexes with 2-ketobutyrate, pyruvate, oxamate, or 4-methyl-2-oxovalerate and two different pH conditions (pH 6.0 and 7.7). The structural findings, in combination with docking simulation and kinetics briefly summarized in Section 3.4 and Fig. 3-15, have refined the catalytic mechanism of the HpaI/HpcH-aldolase subfamily. More interestingly, the present results demonstrate the structural bases for the stereoselective reaction and substrate specificity of asHPAL and enabled the design of new enzymes with high stereoselectivity and a broad range of substrates.

Docking simulations showed that the methyl group of acetaldehyde formed a π -CH interaction with the phenyl ring of Phe26. This interaction appeared to ensure the particular direction of the methyl group of acetaldehyde. In fact, the phenyl ring regulates the preferable stereoselective production of (3*S*,4*S*)-HMKP; this finding was supported by the decreased stereoselectivity in the F26W and F26L mutants. Based on this structure, the stereoselectivity of asHPAL was improved by the N219Y/F26N double mutation, which produced (2*S*,3*R*,4*S*)-4-HIL selectively in 91% enantiomeric excess (*ee*) at pH 6.0. However, the stereoselectivity of asHPAL is still not high enough for industrial use (>99% *ee*) [75]. The results with the N219Y/F26N double mutation confirmed that Phe26 and Asn219 could be useful targets to improve the stereoselectivity of asHPAL. In the future, the saturated mutations of the target residues should be evaluated to find mutants with more favorable stereoselectivity than the N219Y/F26N mutant. In addition, the asHPAL structures at pH 6.0 and 7.7 cannot explain the mechanism for the pH dependency of stereoselectivity. The F26L mutation caused the loss of stereoselectivity in the tested pH conditions, indicating that the acetaldehyde direction at the active site for (3*S*,4*S*)-HMKP production could be energetically favored by the expected π -CH interaction between the methyl group of acetaldehyde and the phenyl ring of Phe26. The energetic contribution of the π -CH interaction may be affected by different pH conditions to

change the predominant acetaldehyde direction at the active site. To evaluate this hypothesis, quantum mechanics together with kinetics studies on several mutants of the residues surrounding the phenyl ring of Phe26 are powerful tools that can be used.

The structure of the asHPAL-4-methyl-2-oxovalerate complex showed that Phe177 is a critical residue that determines the substrate specificity by allowing space for the isopropyl group at the C4 position of 4-methyl-2-oxovalerate. Based on the structural basis, the substrate specificity of asHPAL was changed toward 4-methyl-2-oxovalerate by the F177A mutation. Furthermore, the additional S181W mutation could restrict 4-methyl-2-oxovalerate in the same orientation as a preferable substrate, 2-ketobutyrate, and the resulting activity toward 4-methyl-2-oxovalerate was increased by the mutation. In this study, the stereoselectivity of the F177A/S181W double mutant remains unclear because it is difficult to chemically synthesize a single enantiomer of 2-amino-3-isopropyl-4-oxido-pentanoate for the HPLC assay with a chiral separation column. There are several methods to determine the absolute configuration of compounds, such as the advanced Mosher method [76-78], X-ray crystallographic analysis [79], NMR measurements using chiral shift reagents [80-82], and circular dichroism [83]. In the future, I will try to separate the target product from the reaction mixture and then analyze the stereoselectivity of the F177A/S181W mutants using the aforementioned methods. According to the structural findings of my research, the stereoselectivity of asHPAL is governed by the π -CH interaction between the methyl group of acetaldehyde and the phenyl ring of Phe26, whereas the orientation of α -keto acids does not participate in the stereoselectivity. Because the F177A/S181W mutant retains the Phe26 residue, the double mutant is expected to catalyze the aldol reaction of 4-methyl-2-oxovalerate with the preferable stereoselectivity for single enantiomer production.

Fig. 5-1 showed the key amino acid residues involved in catalysis, substrate binding, stereoselectivity and substrate specificity of asHPAL. Further multiple sequence

alignment of asHPAL, BphF, YfaU, YhaF, and HpcH (Fig. 5-2) showed that these aldolases had the same residues involved in the catalysis, ligand binding and substrate specificity, indicating that BphF, YfaU, YhaF, and HpcH may have similar substrate specificity. However, the similarity of the residues involved in the stereoselectivity among BphF, YfaU, YhaF, and HpcH indicated that BphF and HpcH might have similar stereoselectivity as YfaU and YhaF. Because the activity of YfaU and YhaF are higher than asHPAL, it is expected that additional study of the difference between asHPAL and the 4 kinds of aldolases may help us improve in catalytic activity of asHPAL.

A further homology search using the Basic Local Alignment Search Tool (BLAST) showed that more than 100 aldolases share a high amino acid sequence identity (>50%). Among these, there are 8 aldolases with Phe and Asn residues at positions corresponding to Phe26 and Asn219 of asHPAL (Fig. 5-2). These aldolases have the residues involved in the catalytic reaction and therefore may exert similar stereoselectivity as asHPAL. In addition, the residues contributing to substrate specificity of asHPAL, Phe177 and Ser181, were investigated among the aldolases with a high sequence identity. Some aldolases had a Leu residue at the position corresponding to Phe177 of asHPAL. Because the side chain is bulkier than the Ala residue in the F177A mutant, which can catalyze the aldol reaction between 4-methyl-2-oxovalerate and acetaldehyde, these aldolases should exhibit narrow substrate specificity similarly as asHPAL. Although the structural bases revealed in this study are useful to identify the asHPAL-like aldolases with improved stereoselectivity and expanded substrate specificity from the sequence database and the natural metagenomes, the sequential search showed that the designed asHPAL mutants might possess the specific residues for the improvements of stereoselectivity and substrate specificity as non-natural enzymes.

My research focused on the mechanistic bases for the stereoselectivity and substrate specificity of asHPAL and led to the design of the N219Y/F26N and F177A/S181W mutants as

HpaI/HpcH-aldolase subfamily enzymes with improved stereoselectivity and substrate specificity toward 4-methyl-2-oxovalerate, respectively. Further studies will be performed to improve the enzymatic properties, especially the stereoselectivity to produce (2*S*,3*R*,4*S*)-4-HIL in the coupled reaction with BCAT. The unveiled structural bases could help design more useful enzymes with improved stereoselectivity and a broad range of substrate specificity.

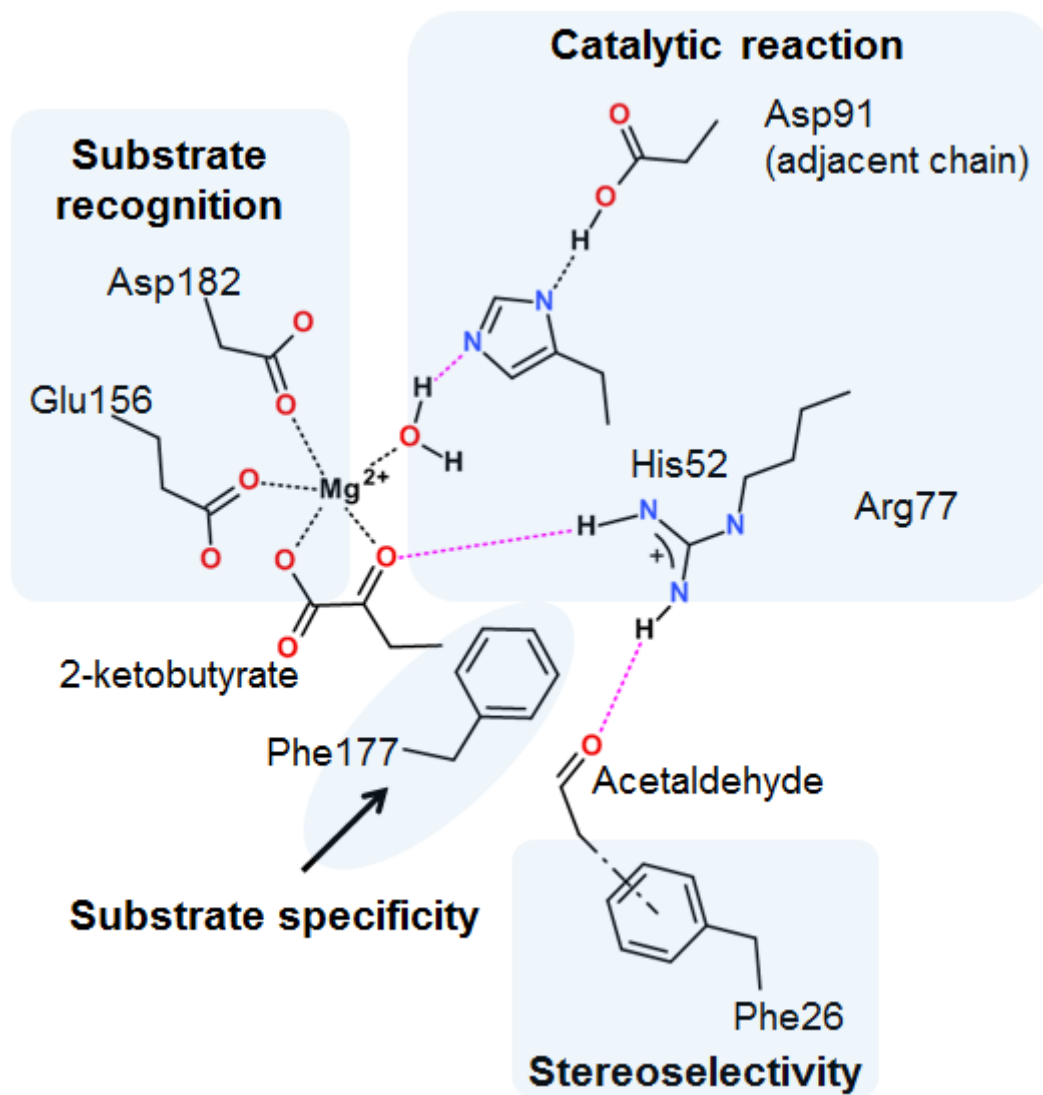


Fig. 5-1 The key amino acid residues involved in catalysis, substrate binding, stereoselectivity and substrate specificity of asHPAL

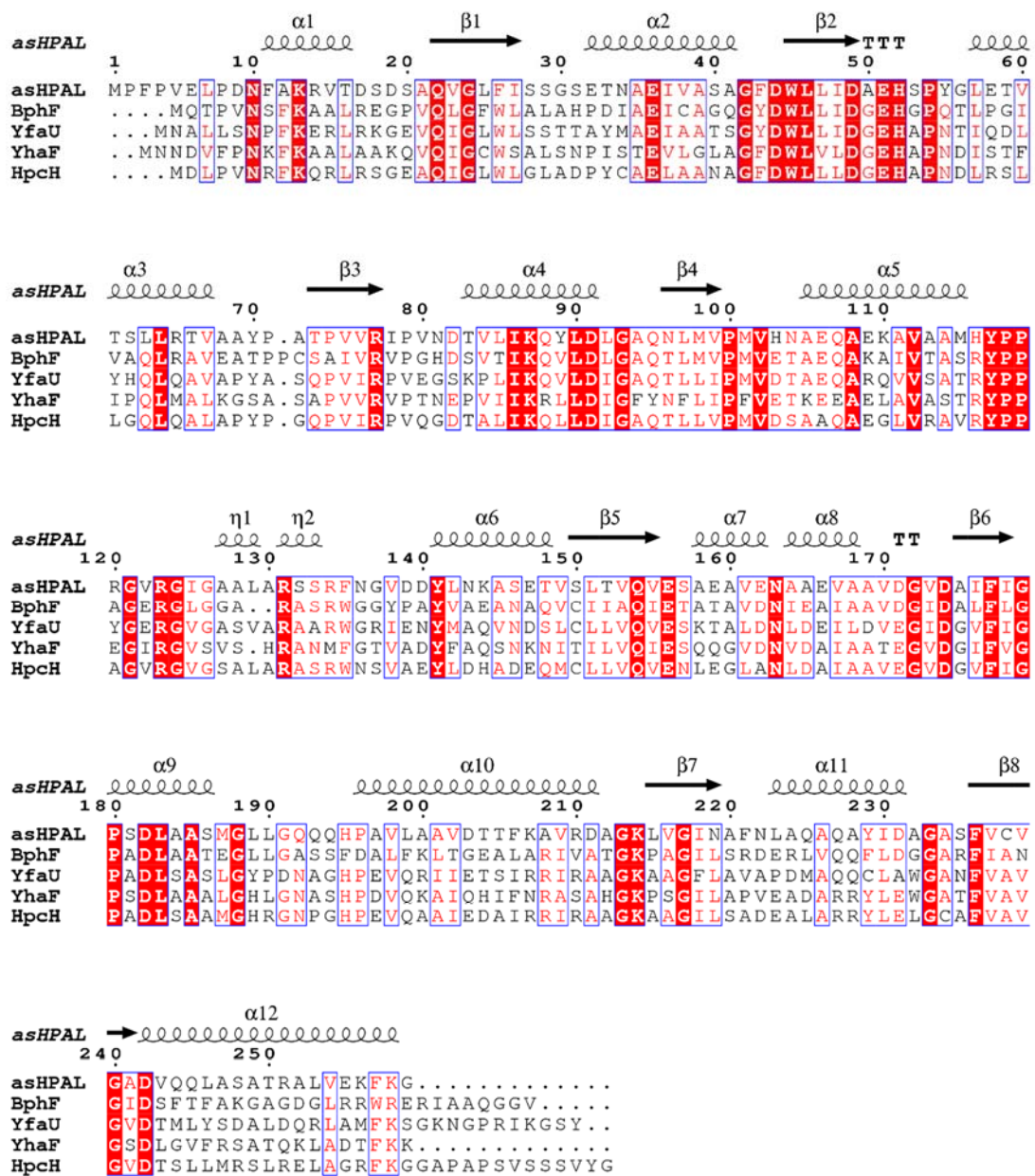


Fig. 5-2 Multiple sequence alignment of asHPAL, BphF, YfaU, YhaF, and HpcH. Sequences were aligned by using ClustalW [84]. The 70% consensus sequence was generated by ESPript [85]: capital letters indicate identity, and lowercase letters indicate a consensus level of >0.5.

	Stereoselectivity	Catalytic reaction	Substrate specificity
asHPAL	...GLFIS...GINAF...	...AEHSP...VVRIP...YLDLG...QVESA...PSDLA...	...AIFIGPSDL...
1	...GLFIT...GINAF...	...AEHSP...VVRIP...YLDLG...QVESA...PSDLA...	...AIFIGPSDL...
2	...GLFLS...GVNAF...	...AEHSP...VVRIP...YLDLG...QIESG...PSDLA...	...AVFIGPSDL...
3	...GIFIN...GVNAF...	...AEHSP...VVRIP...YLDLG...QAESA...PSDLA...	...CVFVGPSDL...
4	...GIFLS...GVNAF...	...GEHSP...VVRVP...YLDLG...QAESA...PSDLA...	...GVFVGPSDL...
5	...GIFLS...GVNAF...	...GEHSP...VVRVP...YLDLG...QAESA...PSDLA...	...GVFVGPSDL...
6	...GIFLS...GVNAF...	...GEHSP...VVRVP...YLDLG...QAESA...PSDLA...	...GVFVGPSDL...
7	...GMFVC...GVNAF...	...GEHGP...VVRVP...YLDLG...QIEAA...PSDLA...	...GVFIGPSDL...
8	...GMFLS...GVNAF...	...AEHAP...LVRVP...VLDLG...QVESA...PSDLS...	...GVFIGPSDL...
9	...GMWVC...GVNAF...	...MEHSP...VVRVP...VLDVG...QVETA...PADLS...	...GVLVGPADL...
10	...GAWVC...GVNAF...	...AEHSP...LVRPP...YLDIG...QIESA...PADLA...	...GILIGPADL...
11	...GQWVC...GVNAF...	...GEHSP...VVRAP...LLDLG...QIETA...PADLA...	...ALLVGPADL...

Fig. 5-3 Sequence alignment of asHPAL with other aldolases.

The amino acid residues colored blue, red, and green represent the residues involved in the stereoselectivity, catalytic reaction, and substrate specificity of asHPAL.

1, 2-dehydro-3-deoxy-D-glucarate aldolase from *Corynebacterium casei* (gi|493875823; Sequence identity to asHPLA, 93%); **2**, 2-dehydro-3-deoxy-D-glucarate aldolase from *Corynebacterium atypicum* (gi|740819474; Seq. identity, 76%); **3**, 2-dehydro-3-deoxy-D-glucarate aldolase from *Corynebacterium glucuronolyticum* (gi|491533728; Seq. identity, 72%); **4**, 2-dehydro-3-deoxy-D-glucarate aldolase from *Kocuria rhizophila* (gi|491533728; Seq. identity, 58%); **5**, 2-dehydro-3-deoxy-D-glucarate aldolase from *Kocuria rhizophila* (gi|697972844; Seq. identity, 57%); **6**, 2-dehydro-3-deoxy-D-glucarate aldolase from *Kocuria rhizophila* (gi|746027423; Seq. identity, 57%); **7**, putative 2,4-dihydroxyhept-2-ene-1,7-dioic acid aldolase (HpaI) from *Arthrobacter crystallopoietes* (gi|491414136; Seq. identity, 61%); **8**, 2-dehydro-3-deoxy-D-glucarate aldolase from *Citricoccus sp.* CH26A (gi|750081262; Seq. identity, 60%); **9**, 2-dehydro-3-deoxy-D-glucarate aldolase from *Cellulomonas carbonis* T26 (gi|697972844; Seq. identity, 61%); **10**, 2-dehydro-3-deoxy-D-glucarate aldolase from *Agromyces subbeticus* (gi|651370090; Seq. identity, 56%); and **11**, 2-dehydro-3-deoxy-D-glucarate aldolase from *Leifsonia aquatica* 54 (gi|640734204; Seq. identity, 54%).

References

- [1] Wade, L.G., *Organic chemistry*. 1999, Upper Saddle River, N.J.: Prentice Hall.
- [2] Anonymous, Annual Report in Medicinal Chemistry, 1992-2009, 2009. **27-44**.
- [3] Bartholow, M., *Top 200 Drugs of 2010*. Pharmacy Times, 2010.
- [4] Nelson, D.L., D.L. Nelson, A.L. Lehninger, and M.M. Cox, *Lehninger principles of biochemistry*. 2008, New York: W.H. Freeman.
- [5] Leffingwell, J.C., *Chirality & Bioactivity I.: Pharmacology*. Leffingwell Reports, 2003. **3**: p. 1-27.
- [6] Blaschke, G., *Chromatographische Racemattrennung von Thalidomid und teratogene Wirkung der Enantiomere*. Arzneimittelforschung, 1979. **29**: p. 1640-1642.
- [7] Nguyen, L.A., H. He, and C. Pham-Huy, *Chiral Drugs: An Overview*. International Journal of Biomedical Science : IJBS, 2006. **2**(2): p. 85-100.
- [8] McNaught, A.D., A. Wilkinson, A.D. Jenkins, P. International Union of, and C. Applied, *IUPAC compendium of chemical terminology the gold book*. 2006, [Research Triangle Park, N.C.]: International Union of Pure and Applied Chemistry.
- [9] Bauer, E.B., *Chiral-at-metal complexes and their catalytic applications in organic synthesis*. Chemical Society Reviews, 2012. **41**(8): p. 3153-3167.
- [10] Heitbaum, M., F. Glorius, and I. Escher, *Asymmetric Heterogeneous Catalysis*. Angewandte Chemie International Edition, 2006. **45**(29): p. 4732-4762.
- [11] Roos, G., *Compendium of chiral auxiliary applications*. 2002, San Diego: Academic Press.
- [12] Faber, K., *Biotransformations in organic chemistry : a textbook*. 2004, Berlin [etc.]: Springer.
- [13] Mukaiyama, T., *The Directed Aldol Reaction*, in *Organic Reactions*. 2004, John Wiley & Sons, Inc.
- [14] Smith, M., J. March, and J. March, *March's advanced organic chemistry : reactions*,

- mechanisms, and structure*. 2001, New York: Wiley.
- [15] *Modern aldol reactions 1, 1*. 2004, Weinheim: Wiley-VCH.
- [16] *Modern aldol reactions 2, 2*. 2004, Weinheim: Wiley-VCH.
- [17] Wurtz, A., *Ueber einen Aldehyd-Alkohol*. Journal für Praktische Chemie, 1872. **5**(1): p. 457-464.
- [18] Mestres, R., *A green look at the aldol reaction*. Green Chemistry, 2004. **6**(12): p. 583-603.
- [19] Braun, M. and R. Devant, *(R)- and (S)-2-acetoxy-1,1,2-triphenylethanol - effective synthetic equivalents of a chiral acetate enolate*. Tetrahedron Letters, 1984. **25**(44): p. 5031-5034.
- [20] Brown, H.C., R.K. Dhar, R.K. Bakshi, P.K. Pandiarajan, and B. Singaram, *Major effect of the leaving group in dialkylboron chlorides and triflates in controlling the stereospecific conversion of ketones into either [E]- or [Z]-enol borinates*. Journal of the American Chemical Society, 1989. **111**(9): p. 3441-3442.
- [21] Ireland, R.E. and A.K. Willard, *The stereoselective generation of ester enolates*. Tetrahedron Letters, 1975. **16**(46): p. 3975-3978.
- [22] Narula, A.S., *An analysis of the diastereomeric transition state interactions for the kinetic deprotonation of acyclic carbonyl derivatives with lithium diisopropylamide*. Tetrahedron Letters, 1981. **22**(41): p. 4119-4122.
- [23] Ireland, R.E., P. Wipf, and J.D. Armstrong, *Stereochemical control in the ester enolate Claisen rearrangement. 1. Stereoselectivity in silyl ketene acetal formation*. The Journal of Organic Chemistry, 1991. **56**(2): p. 650-657.
- [24] Xie, L., K.M. Isenberger, G. Held, and L.M. Dahl, *Highly Stereoselective Kinetic Enolate Formation: Steric vs Electronic Effects*. J Org Chem, 1997. **62**(21): p. 7516-7519.
- [25] Evans, D.A., J.V. Nelson, E. Vogel, and T.R. Taber, *Stereoselective aldol condensations*

- via boron enolates*. Journal of the American Chemical Society, 1981. **103**(11): p. 3099-3111.
- [26] Roush, W.R., *Concerning the diastereofacial selectivity of the aldol reactions of .alpha.-methyl chiral aldehydes and lithium and boron propionate enolates*. The Journal of Organic Chemistry, 1991. **56**(13): p. 4151-4157.
- [27] Boyer, P.D., E.G. Krebs, and D.S. Sigman, *The Enzymes*. 1970: Academic Press.
- [28] Fessner, W.-D., A. Schneider, H. Held, G. Sinerius, C. Walter, M. Hixon, and J.V. Schloss, *The Mechanism of Class II, Metal-Dependent Aldolases*. Angewandte Chemie International Edition in English, 1996. **35**(19): p. 2219-2221.
- [29] Dreyer, M.K. and G.E. Schulz, *Catalytic Mechanism of the Metal-dependent Fuculose Aldolase from Escherichia colias Derived from the Structure*. Journal of Molecular Biology, 1996. **259**(3): p. 458-466.
- [30] Lorentzen, E., B. Siebers, R. Hensel, and E. Pohl, *Mechanism of the Schiff Base Forming Fructose-1,6-bisphosphate Aldolase: Structural Analysis of Reaction Intermediates*†. Biochemistry, 2005. **44**(11): p. 4222-4229.
- [31] Horecker, B.L., P.T. Rowley, E. Grazi, T. Cheng, and O. Tchola, *THE MECHANISM OF ACTION OF ALDOLASES. IV. LYSINE AS THE SUBSTRATE-BINDING SITE*. Biochem Z, 1963. **338**: p. 36-51.
- [32] St-Jean, M. and J. Sygusch, *Stereospecific proton transfer by a mobile catalyst in mammalian fructose-1,6-bisphosphate aldolase*. J Biol Chem, 2007. **282**(42): p. 31028-37.
- [33] Rutter, W.J., *EVOLUTION OF ALDOLASE*. Fed Proc, 1964. **23**: p. 1248-57.
- [34] Liapounova, N.A., V. Hampl, P.M.K. Gordon, C.W. Sensen, L. Gedamu, and J.B. Dacks, *Reconstructing the Mosaic Glycolytic Pathway of the Anaerobic Eukaryote Monocercomonoides*. Eukaryotic Cell, 2006. **5**(12): p. 2138-2146.

- [35] Ogawa, J., H. Yamanaka, J. Mano, Y. Doi, N. Horinouchi, T. Kodera, N. Nio, S.V. Smirnov, N.N. Samsonova, Y.I. Kozlov, and S. Shimizu, *Synthesis of 4-hydroxyisoleucine by the aldolase-transaminase coupling reaction and basic characterization of the aldolase from Arthrobacter simplex AKU 626*. Biosci Biotechnol Biochem, 2007. **71**(7): p. 1607-15.
- [36] Fowden, L., H.M. Pratt, and A. Smith, *4-Hydroxyisoleucine from Seed of Trigonella Foenum-Graecum*. Phytochemistry, 1973. **12**(7): p. 1707-1711.
- [37] Gieren, A., Narayana.P, W. Hoppe, M. Hasan, K. Michl, T. Wieland, H.O. Smith, G. Jung, and Breitmai.E, *Components of Green Deathcap Toadstool, Amanita-Phalloides .44. Configuration of Hydroxylated Isoleucines from Amatoxins*. Annalen Der Chemie-Justus Liebig, 1974(10): p. 1561-1569.
- [38] Alcock, N.W., D.H.G. Crout, M.V.M. Gregorio, E. Lee, G. Pike, and C.J. Samuel, *Stereochemistry of the 4-hydroxyisoleucine from Trigonella foenum-graecum*. Phytochemistry, 1989. **28**(7): p. 1835-1841.
- [39] Jacob, M., M.L. Roumestant, P. Viallefont, and J. Martinez, *Enantioselective synthesis of gamma-hydroxynorvaline*. Synlett, 1997(6): p. 691-692.
- [40] Broca, C., M. Manteghetti, R. Gross, Y. Baissac, M. Jacob, P. Petit, Y. Sauvaire, and G. Ribes, *4-Hydroxyisoleucine: effects of synthetic and natural analogues on insulin secretion*. Eur J Pharmacol, 2000. **390**(3): p. 339-45.
- [41] Mamer, O.A. and M.L. Reimer, *On the mechanisms of the formation of L-alloisoleucine and the 2-hydroxy-3-methylvaleric acid stereoisomers from L-isoleucine in maple syrup urine disease patients and in normal humans*. J Biol Chem, 1992. **267**(31): p. 22141-7.
- [42] Hall, T.R., R. Wallin, G.D. Reinhart, and S.M. Hutson, *Branched chain aminotransferase isoenzymes. Purification and characterization of the rat brain isoenzyme*. Journal of Biological Chemistry, 1993. **268**(5): p. 3092-3098.

- [43] Wright, A., A. Blewett, V. Fulop, R. Cooper, S. Burrows, C. Jones, and D. Roper, *Expression, purification, crystallization and preliminary characterization of an HHED aldolase homologue from Escherichia coli K12*. Acta Crystallogr D Biol Crystallogr, 2002. **58**(Pt 12): p. 2191-3.
- [44] Izard, T. and N.C. Blackwell, *Crystal structures of the metal-dependent 2-dehydro-3-deoxy-galactarate aldolase suggest a novel reaction mechanism*. EMBO J, 2000. **19**(15): p. 3849-56.
- [45] Romine, M.F., L.C. Stillwell, K.K. Wong, S.J. Thurston, E.C. Sisk, C. Sensen, T. Gaasterland, J.K. Fredrickson, and J.D. Saffer, *Complete sequence of a 184-kilobase catabolic plasmid from Sphingomonas aromaticivorans F199*. J Bacteriol, 1999. **181**(5): p. 1585-602.
- [46] Rea, D., V. Fulop, T.D. Bugg, and D.I. Roper, *Structure and mechanism of HpcH: a metal ion dependent class II aldolase from the homoprotocatechuate degradation pathway of Escherichia coli*. J Mol Biol, 2007. **373**(4): p. 866-76.
- [47] Rea, D., R. Hovington, J.F. Rakus, J.A. Gerlt, V. Fulop, T.D. Bugg, and D.I. Roper, *Crystal structure and functional assignment of YfaU, a metal ion dependent class II aldolase from Escherichia coli K12*. Biochemistry, 2008. **47**(38): p. 9955-65.
- [48] Donnay, J.D.H., *X-Ray Crystallographic Technology. André Guinier; trans. by T. L. Tippell; Kathleen Lonsdale, Ed. London: Hilger and Watts, 1952. (U.S. distrib.: Jarrell-Ash, Boston.) 330 pp. Illus. + plates. \$9.50*. Science, 1953. **118**(3077): p. 757-758.
- [49] Ealick, S., *Principles of protein X-ray crystallography by J. Drenth*. Acta Crystallographica Section D, 1995. **51**(2): p. 248.
- [50] Tamura, K., G. Stecher, D. Peterson, A. Filipinski, and S. Kumar, *MEGA6: Molecular Evolutionary Genetics Analysis version 6.0*. Molecular Biology and Evolution, 2013.
- [51] Smirnov, S.V., N.N. Samsonova, A.E. Novikova, N.G. Matrosov, N.Y. Rushkevich, T.

- Kodera, J. Ogawa, H. Yamanaka, and S. Shimizu, *A novel strategy for enzymatic synthesis of 4-hydroxyisoleucine: identification of an enzyme possessing HMKP (4-hydroxy-3-methyl-2-keto-pentanoate) aldolase activity*. FEMS Microbiol Lett, 2007. **273**(1): p. 70-7.
- [52] Larkin, M.A., G. Blackshields, N.P. Brown, R. Chenna, P.A. McGettigan, H. McWilliam, F. Valentin, I.M. Wallace, A. Wilm, R. Lopez, J.D. Thompson, T.J. Gibson, and D.G. Higgins, *Clustal W and Clustal X version 2.0*. Bioinformatics, 2007. **23**(21): p. 2947-2948.
- [53] Pace, C.N., F. Vajdos, L. Fee, G. Grimsley, and T. Gray, *How to measure and predict the molar absorption coefficient of a protein*. Protein Sci, 1995. **4**(11): p. 2411-23.
- [54] Kinoshita, T., Y. Kasahara, and N. Nimura, *Reversed-phase high-performance liquid chromatographic resolution of non-esterified enantiomeric amino acids by derivatization with 2,3,4,6-tetra-*o*-acetyl- β -*D*-glucopyranosyl isothiocyanate and 2,3,4-tri-*o*-acetyl- α -*D*-arabinopyranosyl isothiocyanate*. Journal of Chromatography A, 1981. **210**(1): p. 77-81.
- [55] Collaborative Computational Project, N., *The CCP4 suite: programs for protein crystallography*. Acta Crystallogr D Biol Crystallogr, 1994. **50**(Pt 5): p. 760-3.
- [56] Vagin, A. and A. Teplyakov, *MOLREP: an Automated Program for Molecular Replacement*. Journal of Applied Crystallography, 1997. **30**(6): p. 1022-1025.
- [57] Cohen, S.X., M. Ben Jelloul, F. Long, A. Vagin, P. Knipscheer, J. Lebbink, T.K. Sixma, V.S. Lamzin, G.N. Murshudov, and A. Perrakis, *ARP/wARP and molecular replacement: the next generation*. Acta Crystallogr D Biol Crystallogr, 2008. **64**(Pt 1): p. 49-60.
- [58] Emsley, P. and K. Cowtan, *Coot: model-building tools for molecular graphics*. Acta Crystallogr D Biol Crystallogr, 2004. **60**(Pt 12 Pt 1): p. 2126-32.
- [59] Vagin, A.A., R.A. Steiner, A.A. Lebedev, L. Potterton, S. McNicholas, F. Long, and G.N. Murshudov, *REFMAC5 dictionary: organization of prior chemical knowledge and*

- guidelines for its use.* Acta Crystallogr D Biol Crystallogr, 2004. **60**(Pt 12 Pt 1): p. 2184-95.
- [60] Laskowski, R.A., M.W. MacArthur, D.S. Moss, and J.M. Thornton, *PROCHECK: a program to check the stereochemical quality of protein structures.* Journal of Applied Crystallography, 1993. **26**(2): p. 283-291.
- [61] Holm, L. and P. Rosenstrom, *Dali server: conservation mapping in 3D.* Nucleic Acids Res, 2010. **38**(Web Server issue): p. W545-9.
- [62] Hasegawa, H. and L. Holm, *Advances and pitfalls of protein structural alignment.* Curr Opin Struct Biol, 2009. **19**(3): p. 341-8.
- [63] Andrews, P., *Estimation of the molecular weights of proteins by Sephadex gel-filtration.* Biochemical Journal, 1964. **91**(2): p. 222-233.
- [64] Matthews, B.W., *Solvent content of protein crystals.* J Mol Biol, 1968. **33**(2): p. 491-7.
- [65] Vella, F., *Introduction to protein structure. By C Branden and J Tooze. pp 302. garland publishing, New York. 1991 ISBN 0-8513-0270-3 (pbk).* Biochemical Education, 1992. **20**(2): p. 121-122.
- [66] Kabsch, W., *Xds.* Acta Crystallogr D Biol Crystallogr, 2010. **66**(Pt 2): p. 125-32.
- [67] Chemical Computing Group Inc., S.S.W., Suite #910, Montreal, QC, Canada, H3A 2R7, 2013. , *Molecular Operating Environment (MOE), 2013.08.*
- [68] Edelsbrunner, H., M. Facello, F. Ping, and L. Jie. *Measuring proteins and voids in proteins.* in *System Sciences, 1995. Proceedings of the Twenty-Eighth Hawaii International Conference on.* 1995.
- [69] Goto, J., R. Kataoka, H. Muta, and N. Hirayama, *ASEDock-docking based on alpha spheres and excluded volumes.* J Chem Inf Model, 2008. **48**(3): p. 583-90.
- [70] 中村, 博., *パソコンによるFT-NMRのデータ処理* 第2版 ed. 2009: 三共出版. ix, 134p.
- [71] Lineweaver, H. and D. Burk, *The Determination of Enzyme Dissociation Constants.*

- Journal of the American Chemical Society, 1934. **56**(3): p. 658-666.
- [72] Michaelis, L. and M.L. Menten, *{Die kinetik der invertinwirkung}*. Biochem. Z, 1913. **49**(333-369): p. 352.
- [73] Cederstav, A.K. and B.M. Novak, *Investigations into the Chemistry of Thermodynamically Unstable Species. The Direct Polymerization of Vinyl Alcohol, the Enolic Tautomer of Acetaldehyde*. Journal of the American Chemical Society, 1994. **116**(9): p. 4073-4074.
- [74] Otwinowski, Z. and W. Minor, *Processing of X-ray diffraction data collected in oscillation mode*. 1997, Elsevier. p. 307-326.
- [75] Sutton, P.W., J.P. Adams, I. Archer, D. Auriol, M. Avi, C. Branneby, A.J. Collis, B. Dumas, T. Eckrich, I. Fotheringham, R. ter Halle, S. Hanlon, M. Hansen, K.E. Holt-Tiffin, R.M. Howard, G.W. Huisman, H. Iding, K. Kiewel, M. Kittelmann, E. Kupfer, K. Laumen, F. Lefèvre, S. Luetz, D.P. Mangan, V.A. Martin, H.-P. Meyer, T.S. Moody, A. Osorio-Lozada, K. Robins, R. Snajdrova, M.D. Truppo, A. Wells, B. Wirz, and J.W. Wong, *Biocatalysis in the Fine Chemical and Pharmaceutical Industries*, in *Practical Methods for Biocatalysis and Biotransformations 2*. 2012, John Wiley & Sons, Ltd. p. 1-59.
- [76] Dale, J.A., D.L. Dull, and H.S. Mosher, *.alpha.-Methoxy-.alpha.-trifluoromethylphenylacetic acid, a versatile reagent for the determination of enantiomeric composition of alcohols and amines*. The Journal of Organic Chemistry, 1969. **34**(9): p. 2543-2549.
- [77] Ohtani, I., T. Kusumi, Y. Kashman, and H. Kakisawa, *High-field FT NMR application of Mosher's method. The absolute configurations of marine terpenoids*. Journal of the American Chemical Society, 1991. **113**(11): p. 4092-4096.
- [78] Hoye, T.R., C.S. Jeffrey, and F. Shao, *Mosher ester analysis for the determination of*

- absolute configuration of stereogenic (chiral) carbinol carbons*. Nat. Protocols, 2007. **2**(10): p. 2451-2458.
- [79] Flack, H.D. and G. Bernardinelli, *The use of X-ray crystallography to determine absolute configuration*. Chirality, 2008. **20**(5): p. 681-90.
- [80] Kobayashi, Y., N. Hayashi, and Y. Kishi, *Toward the creation of NMR databases in chiral solvents: bidentate chiral NMR solvents for assignment of the absolute configuration of acyclic secondary alcohols*. Org Lett, 2002. **4**(3): p. 411-4.
- [81] Ghosh, I., H. Zeng, and Y. Kishi, *Application of chiral lanthanide shift reagents for assignment of absolute configuration of alcohols*. Org Lett, 2004. **6**(25): p. 4715-8.
- [82] Kobayashi, Y., N. Hayashi, and Y. Kishi, *Application of chiral bidentate NMR solvents for assignment of the absolute configuration of alcohols: scope and limitation*. Tetrahedron Letters, 2003. **44**(40): p. 7489-7491.
- [83] Freedman, T.B., X. Cao, R.K. Dukor, and L.A. Nafie, *Absolute configuration determination of chiral molecules in the solution state using vibrational circular dichroism*. Chirality, 2003. **15**(9): p. 743-58.
- [84] Thompson, J.D., D.G. Higgins, and T.J. Gibson, *CLUSTAL W: improving the sensitivity of progressive multiple sequence alignment through sequence weighting, position-specific gap penalties and weight matrix choice*. Nucleic Acids Research, 1994. **22**(22): p. 4673-4680.
- [85] Robert, X. and P. Gouet, *Deciphering key features in protein structures with the new ENDscript server*. Nucleic Acids Research, 2014. **42**(W1): p. W320-W324.

Acknowledgments

I would like to express the most sincere thanks to my supervisor, Prof. TANOKURA Masaru. He kept guiding me to the right path, offering valuable advice, keeping me inspired, and trying to build a research atmosphere as pleasant as possible. Without him, I could not have developed my knowledge and research skills so smoothly.

I deeply appreciate Prof. OGAWA Jun and Dr. HIBI Makoto at Kyoto University. The recombinant asHPAL expression plasmid and catalytic activities analysis method was provided by them. Most of the results described in this thesis would not have been obtained without collaboration with them.

I am also grateful to Dr. NAGATA Koji, Associate Professor in Tanokura's laboratory at the University of Tokyo. He always supports me to advance my research, and understands what the problem is.

I also want to thank Dr. OKAI Masahiko and Dr. MIYAKAWA Takuya, for teaching me how important it is to think about vents from a broad standpoint of view, as well as the skills of X-ray structural analysis. It is a pleasure to have worked with all the members of TANOKURA laboratory. They now constitute an important and indispensable dimension in my life.

I am extremely thankful to the staff of the Photon Factory of the National Laboratory for High Energy Physics and SPring-8 for their assistance.

Finally, I am deeply grateful to my family and friends for their constant help and the financial support from University of Tokyo that made my doctoral study possible.